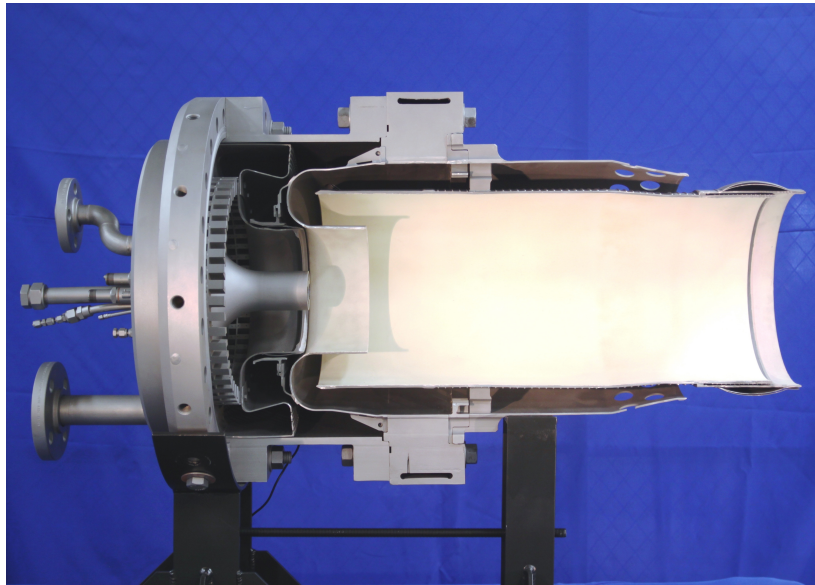


# Master of Science Thesis

Boundary layer flashback prediction of a low emissions  
full hydrogen burner for gas turbine applications.

Joeri Tober

January 15, 2019



Faculty of Mechanical Engineering  
Department of Process and Energy  
Delft, University of Technology  
Delft, The Netherlands

Supervisors:  
Prof.dr.ir. Sikke Klein  
Johan Steimes PhD

## Acknowledgements

This is the final thesis of the track Energy and Process Technology, which is a specialization of the master Mechanical Engineering. The thesis has been worked on individually and is worth 45 ECTS, which is equivalent to approximately eight months of full time work.

Hereby I would like to thank Nitish Gadgil for obtaining relevant literature for my thesis. Also thanks to Dirk Roekaerts, Rene Pecnik, Mathieu Pourquoi and Gustavo Otero for taking time to help me out with questions. Furthermore I would like to thank Johan Steimes for supervising me on a weekly basis. It was fun and very helpful. Many thanks to Sikke Klein, who supervised my project. I enjoyed the in-depth discussions on Lewis numbers, burning velocities and all that was related.

Finally many thanks to my family and Rowie. Without the (financial and general) support of my parents it was never possible to study for such a long time and go for an exchange. Thanks to Rowie I realized the importance of setting realistic goals, of which this thesis is a result I am very proud of.

Joeri Tober, TU Delft, Delft, January 2019

# Abstract

A highly accurate model is presented that predicts boundary layer flashback (BLF) for lean premixed hydrogen combustion. In contrast to existing models, that fail for lean hydrogen mixtures, the present model includes the effect of flame instabilities. The model is applied to study the effect of burner geometry on flashback tendency. A diverging geometry results in a higher flashback tendency due to an adverse pressure gradient. These observations are in line with experimental results. It shows that the BLF model is a tool that could significantly contribute to the development of lean premixed hydrogen burners. This is a great step towards carbon-free industrial gas turbines.

# Contents

<b>1</b>	<b>Introduction</b>	<b>1</b>
1.1	Flashback Mechanisms . . . . .	4
1.2	Recent Studies on Boundary Layer Flashback . . . . .	5
1.3	Thesis Outline . . . . .	5
<b>2</b>	<b>Theory</b>	<b>8</b>
2.1	Historical Overview . . . . .	8
2.2	Relevant Physical Concepts . . . . .	11
2.2.1	Stratford Separation Criterion . . . . .	11
2.2.2	Turbulent Burning Velocity . . . . .	13
2.2.3	Stretched Laminar Burning Velocity . . . . .	18
2.2.4	Markstein Length . . . . .	20
2.2.5	Turbulence . . . . .	21
2.3	Hoferichter’s Model . . . . .	23
2.3.1	Model Description . . . . .	23
2.3.2	Results and Validation . . . . .	26
2.3.3	Discussion . . . . .	28
2.4	Conclusion . . . . .	31
<b>3</b>	<b>Improvements to the Analytical Model</b>	<b>33</b>
3.1	Model Duplication . . . . .	33
3.2	Improvement Study 1: Turbulence-Flame Interaction . . . . .	35
3.2.1	Effect of the Flame on Upstream Turbulence . . . . .	36
3.2.2	Code Modification . . . . .	39
3.3	Improvement Study 2: Flame Instabilities . . . . .	40
3.3.1	Onset to a Cellular Flame Structure . . . . .	41
3.3.2	Effect of Flame Instabilities on Burning Velocity . . . . .	43
3.3.3	Code Modification . . . . .	45
3.4	Improvement Study 3: Flame Stretch . . . . .	45
3.4.1	Code Modification . . . . .	46
3.5	Results and Discussion . . . . .	49
3.6	Conclusion . . . . .	57
<b>4</b>	<b>Effect of a Diverging Flow on Flashback Tendency</b>	<b>58</b>
4.1	Effect of the Geometry on the Flow Parameters . . . . .	59
4.2	Effect of the Flow Parameters on Flashback Tendency . . . . .	65
4.3	Conclusion . . . . .	69
<b>5</b>	<b>Conclusion and Recommendations</b>	<b>70</b>
<b>6</b>	<b>Appendix</b>	<b>76</b>
6.1	BLF Model - Python Code . . . . .	76
6.2	Fluent Example: Basics . . . . .	81
6.3	CFD Results . . . . .	94

# 1 Introduction

Today there are mainly two concerns within the world of energy: climate changes and depleting resources. Both problems should be considered a serious threat for us and for future generations. Although progress is being made, according to the latest update of the International Energy Agency [1] still only 13.6 % of the world's Total Primary Energy Supply (TPES) comes from a sustainable source. Without doubts it is therefore of importance to develop and improve energy systems that are based on renewable resources. This thesis does that by contributing to the development of a hydrogen fueled industrial gas turbine.

Using pure hydrogen in gas turbines is closely related to the characteristics of both the renewable power and the gas turbine. Renewable power generation is characterized by a highly fluctuating output, caused by variations in solar and wind. This is shown in Figure 1. When more power is being produced than used, one option is to store energy by producing hydrogen. Energy is used to split water into hydrogen and oxygen, which can be used as a fuel at a later moment. On the other hand, to ensure a steady, reliable power supply, technologies are required to balance the fluctuations. Compared to coal fired and nuclear power plants, a gas turbine is superior to perform this task. This is due to the combination of a short start up time, a high turn-down ratio (flexible power output) and a high efficiency.

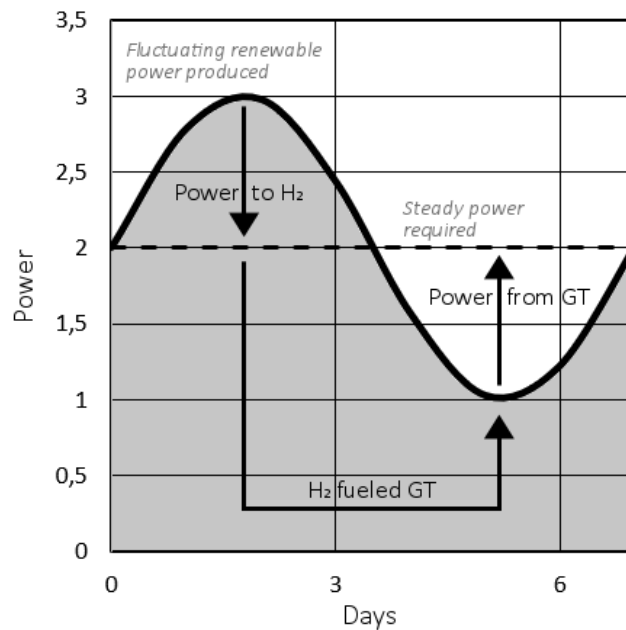


Figure 1: Surplus renewable energy (used to produce hydrogen) and shortcomings (compensated for by gas turbines) are combined by using hydrogen as a gas turbine fuel.

Figure 1 illustrates the imbalance between renewable power supply and required power. The surplus of power is used to produce hydrogen and a gas turbine is used in moments

of shortcomings. It shows the opportunity for a hydrogen fueled gas turbine to play an important role to deal with fluctuations.

Whereas almost all industrial gas turbines use natural gas as a fuel, the production of Carbon Dioxide (CO<sub>2</sub>) cannot be avoided. Since CO<sub>2</sub> contributes to global warming, CO<sub>2</sub> emissions from gas turbine combustion should be kept minimal. One possibility that completely eliminates these emissions, is the combustion of alternative, carbon-free fuels such as pure hydrogen. However, there are two points of attention: the origin of hydrogen and two major technical consequences of hydrogen combustion: Nitrous Oxides (NO<sub>x</sub>) production and flame flashback:

- **Hydrogen production:** Three types of hydrogen are distinguished based on CO<sub>2</sub> production. green hydrogen (no CO<sub>2</sub> produced during the process), blue hydrogen (CO<sub>2</sub> is produced, but captured) and grey hydrogen (CO<sub>2</sub> is produced and not captured). According to Gandia [2], who differentiates between renewable (green) and non-renewable (blue and grey) hydrogen, only 4% of the world's hydrogen production (determined in 2013) is renewable.

According to Ad van Wijk [3], one of the hydrogen experts in the Netherlands, the role of hydrogen will increase significantly the coming decades by facilitating the energy transition. The Northern Netherlands has access to offshore wind parks, which can produce green hydrogen on a large scale. Simultaneously, due to gas extraction-induced earthquakes, within society there is a growing desire for replacing natural gas.

To conclude with, it should be kept in mind that a hydrogen fueled energy system is not sustainable by definition, because it still depends on the hydrogen production method. However, increasing the demand for (green) hydrogen, possibly results in more green hydrogen production. Also, with a high potential in the Northern Netherlands, it is expected that green hydrogen production will significantly increase in the next decades [3].

- **NO<sub>x</sub> production:** Although the CO<sub>2</sub> emissions can be eliminated, by using a hydrogen-air mixture, Nitrous Oxides (NO<sub>x</sub>) can still be produced in the combustion process. NO<sub>x</sub> is one of the main components that causes ground level ozone [4]. This can trigger serious respiratory problems, and therefore NO<sub>x</sub> emissions are strictly regulated. In Europe NO<sub>x</sub> emissions (for thermal plants up to 50 MW) are limited to 40 ppmv, in the United States this is only 15 ppmv. NO<sub>x</sub> emissions can be reduced by keeping the flame temperature below 1800 K, which is done by adding more air to the fuel mixture than required for pure stoichiometric combustion. For premixed hydrogen-air mixtures this is shown in Figure 2. For a relative air/fuel ratio higher than 2.2 the NO<sub>x</sub> emissions can be neglected [5]. This is similar to an equivalence ratio below 0.45.
- **Flame flashback:** Comparing combustion of hydrogen to natural gas, the main differences are the reactivity, the diffusivity and the burning velocity. Hydrogen has a laminar flame speed and diffusivity, about four times that of typical natural gases. For premixed combustion, this results in both stability and safety issues due to the risk of upstream flame propagation into the mixing section. This is called flashback and once it occurs engine shutdown is required (the flame cannot be pushed back) and equipment

may be damaged (when temperatures become higher than designed for). This leads to unsafe operation, higher maintenance costs and eventually to a system that is not economically viable.

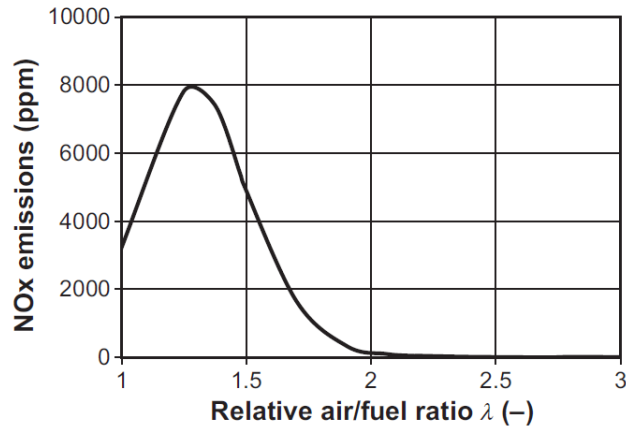


Figure 2: NOx emissions for homogeneous hydrogen air mixtures against relative air/fuel ratio in a typical internal combustion engine (from Verhelst [5]).

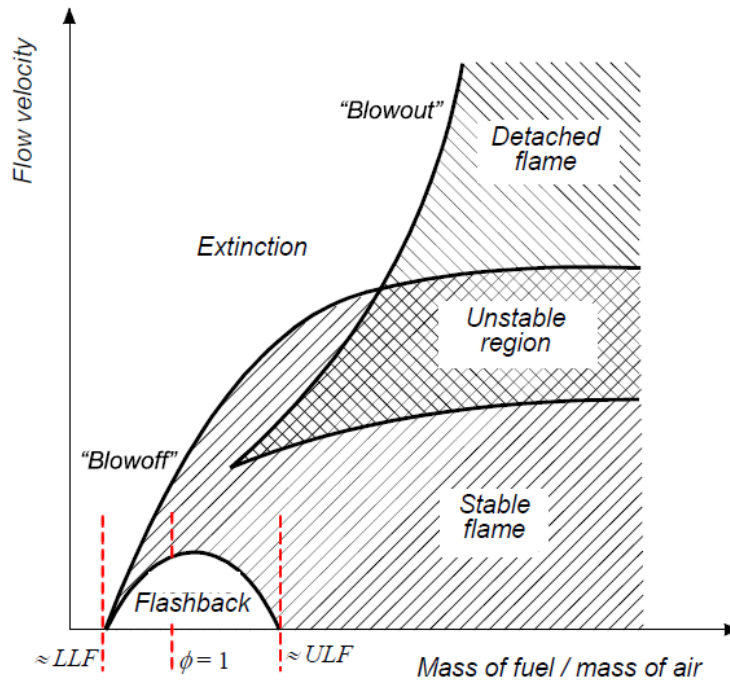


Figure 3: Flame stability diagram for different equivalence ratios, with the Lower and Upper Limit Flashback (LLF and ULF) indicated (from Técnico Lisboa [6]).

The fact that lean premixed combustion solves the problem of NOx emissions, together

with the assumption that large scale green hydrogen becomes available within the coming decades, results in the focus of this thesis: flame flashback. Also, according to Figure 3, flame instabilities (and thus flashback) are of great relevance for lean combustion, due to the narrow stability region.

## 1.1 Flashback Mechanisms

There are mainly four flashback mechanisms:

1. **Flashback in the turbulent core:** When the (turbulent) burning velocity exceeds the flow velocity, the flame front moves upstream. According to Eichler [7], for normal gas turbine operations this type of flashback can be neglected, because the free stream velocity is generally higher than the burning velocity.
2. **Boundary Layer Flashback (BLF):** A boundary layer has a no-slip condition: the velocity in the burner decreases to zero close to the wall. A boundary layer is formed in which local flow velocities drop below the (turbulent) burning velocity. Because of this, upstream flame propagation (flashback) is initiated.
3. **Flashback due to combustion instabilities:** This flashback mechanism is the result of acoustic interaction between the energy release of the flame and the flow structure. Combustion instabilities periodically produce velocity oscillations at the burner exit and, especially for reactive fuels, this has a significant effect on flashback limits. This mechanism can lead to flashback both in the boundary layer and in the turbulent core [8].
4. **Flashback due to Combustion Induced Vortex Breakdown (CIVB):** In case of a swirl-stabilized burner (most GT burners), flashback along the centerline might occur due to the upstream propagation of the recirculation zone. Figure 4 illustrates the concept. According to Al-Fahham [9] the transition to CIVB depends mainly on the swirl number, which is the ratio of the axial flux of tangential momentum over the axial flux of axial momentum times the equivalent nozzle radius. Typically a swirl number above 1.0 results in CIVB. Below 0.5 CIVB hardly occurs. CIVB flashback can be prevented with a proper aerodynamic burner design [10].

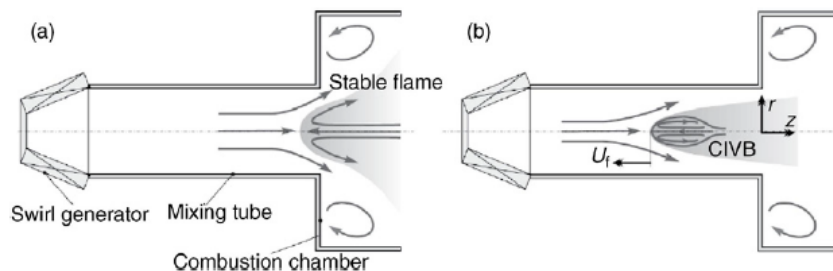


Figure 4: Swirl burner flow patterns for a stable flame (left) and a flame with CIVB flashback (right) (from Benim and Syed [11]).

While the first and fourth flashback mechanisms can be dealt with relatively well, the second and third require more understanding, especially for highly reactive fuels. This thesis focuses on the second mechanism only: boundary layer flashback.

## 1.2 Recent Studies on Boundary Layer Flashback

With a growing interest for pure hydrogen combustion in gas turbines, the studies of BLF have increased. From 2016 on experiments have been performed by Kalantari and McDonell [12, 13] from the University of California. They proposed an empirical relation to predict boundary layer flashback. In 2017 they validated this relation with two commercially available gas turbines: a micro gas turbine, operating at atmospheric pressure and a 60 kw gas turbine. Fuel hydrogen percentages ranged from 30% to 100%. Kalantari and McDonell [14] also presented a paper including an overview of all experiments relevant to BLF.

Meanwhile, Al-Fahham [9] and Hatem [8] from the Cardiff University have studied methods to prevent BLF. Al-Fahham focused on the use of a micromesh, which decreases friction drag in the boundary layer, resulting in more resistance to BLF. His work includes both experiments and modelling and also covers the manufacturing of microstructures. Hatem's work includes experiments with different burner setups and injector configurations. Supported by observations, Hatem defines a dimensionless number which describes the transition from CIVB to BLF. One of the mechanism involved in this transition is swirl: the higher the swirl, the more chance of CIVB, but the lower the chance of BLF.

From 2011 on researchers from TU Munich have been working on the fundamental understanding of BLF. Experiments performed by Eichler [7, 15, 16] and DNS studies from Gruber [17, 18] led to new insights in the BLF mechanism. Baumgartner [19, 20] differentiated between unconfined and confined burner configurations, which have a different flashback mechanism. Finally, Hoferichter [10, 21] proposed a semi-analytical model to predict BLF, based on onset to flow separation. This model uses only one parameter to fit experimental data. However, it has only been validated for atmospheric conditions (temperature of 293 K and pressure of 1 bar). For gas turbines the operating conditions are typically ranging from 500 to 800 K and 10 to 20 bars. Also, the model can be used for simple geometries only: channels and tubes, because it makes use of standard velocity and turbulence profiles.

## 1.3 Thesis Outline

There are two BLF prediction methods: the empirical approach (data-driven) from Kalantari and McDonell and the semi-analytical approach (knowledge-based) from TU Munich. Since data-driven models are only applicable to the range of parameters that were used to feed the model, extending the model to new burner concepts brings high uncertainties. A more fundamental, knowledge-based approach captures the mechanisms behind flashback and is more likely to predict it for new burner concepts. However, the TU Munich model has only been validated for atmospheric conditions and simple geometries. This leads to the thesis objective:

- *To improve the semi-analytical boundary layer flashback model and, by feeding the model with Computational Fluid Dynamics (CFD) results, to study the effect of a geometry change on flashback tendency.*

Improving the model means that it is not only validated for atmospheric conditions, but also for elevated temperatures. For the geometry change to diverging channels are studied. Experimental results are available for both inlet temperatures of 473 K and 673 K and for two diverging channels. An overview of the thesis structure is shown in Figure 5.

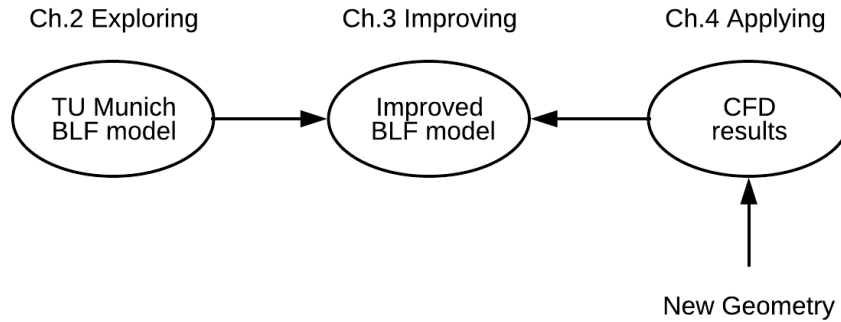


Figure 5: Thesis overview.

In Chapter 2 a literature review is presented. It starts with theory on flame classifications, followed by the first analytical model on BLF proposed by Lewis and von Elbe. Experimental work from TU Munich is then discussed, which has led to the BLF prediction model. This model is the starting point of this thesis and will be explained in detail. Shortcomings and assumptions will be listed. This chapter answers the questions:

- *What are the main assumptions in the BLF model?*
- *Which parameters are critical?*

Based on the findings of Chapter 2, Chapter 3 presents a more in-depth study on turbulence-flame interaction, flame instabilities and (anisotropic) flame stretch. These phenomena are either not well understood or neglected in the existing model. The related parameters, such as the turbulent fluctuations and the Markstein length, cause high uncertainties while the assumption of isotropic turbulence is not valid at all, even for a straight channel or tube. Based on the studies discussed in this chapter, several modifications are proposed and the results are compared to both experiments and to the original model. The following questions are answered:

- *Where in the BLF model can improvements be made?*
- *How well does the improved model matches experiments?*

In chapter 4 model is applied to two diverging channels. First the effect of the geometry on the flow parameters is obtained with CFD. Then these results are used to feed the BLF model. This led to three studies: the effect of smaller turbulent fluctuations, an adverse pressure gradient and high velocity gradients in the boundary layer. The following question has been answered:

- *Why does a diverging channel lead to higher flashback limits and what physical mechanism is responsible for this?*

At last Chapter 5 covers the concluding remarks and future recommendations.

## 2 Theory

The goal of this chapter is to describe the TU Munich model and to find its critical assumptions. To do so, first a brief historical overview is shown. This includes the first physical model for BLF and explains how TU Munich came up with a new theory. Then a number of physical concepts are explained, which are required to fully understand Hoferichter’s BLF model. These concepts include: the Stratford separation criterion, the turbulent burning velocity, the stretched laminar burning velocity, the Markstein length and turbulence. Finally Hoferichter’s model is explained and the results are compared to experiments. The leading questions for this chapter are:

- *What are the main assumptions in the BLF model?*
- *Which parameters are critical?*

### 2.1 Historical Overview

BLF was described first by Lewis and von Elbe [22] in 1943. They conducted experiments with fully developed laminar methane-air flames at ambient pressure and temperature. A model was developed to correlate the flashback limits of laminar flames, in terms of a velocity gradient. A stable flame condition is maintained between two values of the velocity gradient: below the lower gradient the flame flashes back, while above the upper gradient blow-off occurs. In this model the following relations were proposed:

$$g = \left. \frac{\partial u}{\partial y} \right|_{y=0} \tag{2.1}$$

$$g_c = \frac{S_f(\delta_b)}{\delta_b} \tag{2.2}$$

In case of BLF the velocity gradient  $g$  at the wall becomes the critical velocity gradient  $g_c$ , which is estimated by dividing the laminar burning velocity  $S_f$  at the flame tip by the distance to the wall  $\delta_b$ . A diagram related to this is shown in Figure 6, where the velocity profile is shown on the left and the flame front on the right. This approach does not take into account the interaction between the flame and the flow. Also, the critical velocity gradient  $g_c$  cannot be calculated, because the burning velocity  $S_f$  depends on many unknowns, such as flame dynamics, wall temperature etc, and therefore it has to be determined experimentally.

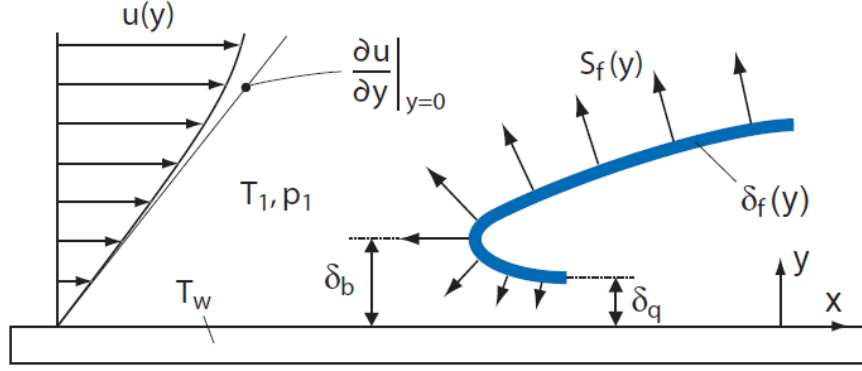


Figure 6: Illustration of the critical velocity gradient model, which predicts BLF for laminar flames (from Eichler [7]).

In 2011 Eichler [7, 15, 16] performed experiments with both laminar and turbulent flames in a channel burner setup with a rectangular cross-section. The experiments were done with premixed hydrogen-air mixtures, over a range of different equivalence ratios, for ambient and elevated temperatures. Based on advanced optical measurement techniques, Eichler concluded that there exists an interaction between the flame and the upstream flow by means of an upstream pressure rise. This was not included in the model of Lewis and von Elbe by. The mechanism is illustrated in Figure 7. This pressure rise leads to flow separation upstream of the flame, and eventually it results in backflow regions which initiate BLF.

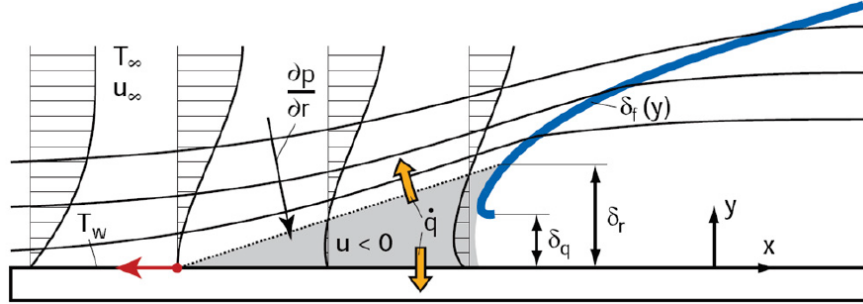


Figure 7: Physical model for laminar and turbulent BLF with adverse flame pressure, proposed by Eichler (from Eichler [7]).

Closely related to the experiments of Eichler were the Direct Numerical Simulation (DNS) studies of Gruber [17, 18] on BLF of a turbulent hydrogen flame in a confined channel. The conditions were a temperature of 750 K, pressures of 1 and 2 atmosphere and an equivalence ratio of 1.5. Flow stagnation and backflow regions were observed. The results of the DNS show the existence of interaction mechanisms between the flame and the upstream flow. Figure 8 shows the instantaneous normalized pressure fields during BLF. The white line indicates the flame front at  $C = 0.7$  (the reaction has progressed up to 70 %) and the flow is from left to right. The presence of a high pressure region shows up upstream of the flame tip, which is in line with the theory proposed by Eichler. Gruber argues that flashback is initiated by the hydrodynamic Darrieus-Landau (DL) instability.

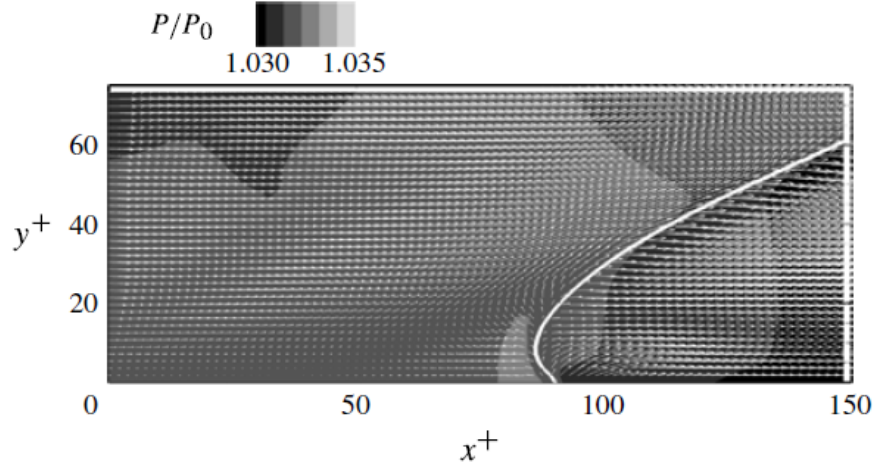


Figure 8: DNS studies showing the normalized instantaneous pressure field  $P$  in the  $xy$ -plane (from Gruber [18]).

Whereas Eichler provided a theory for confined flames, Baumgartner [19] extended this to unconfined flames in 2014. He used Particle Image Velocimetry (PIV) to investigate premixed hydrogen-air mixtures, with a focus on the effect of the rim temperature and the burner exit design. He proposed a theory that includes the BLF transient from unconfined towards confined. In other words: the flame starts in an unconfined configuration, but once the it's front starts to move upstream, the flame tip attaches to the wall and becomes confined. The critical flashback velocity for a confined flame is much higher than the one for the unconfined flame. This means that, an immediate BLF occurs once the unconfined flame attaches to the wall.

In 2017, Hoferichter [10, 21] used both the confined and unconfined theory provided by Eichler and Baumgartner, respectively, to predict a limiting bulk flow velocity  $\bar{U}_{FB}$  at which BLF occurs. With the confined case being critical, this thesis focuses on the confined flame flashback model only. From now on this model is referred to as the TU Munich model, the BLF model or Hoferichter's model.

The model is based on the mechanism shown in Figure 7, a backpressure caused by the flame leading to flow separation and thus BLF. A flow separation criterion is used which was introduced by Stratford [23] in 1959. The criterion relates an upstream pressure increase (an adverse pressure gradient) to separation in turbulent flow. Hoferichter relates the pressure increase to the flame by means of the expansion ratio  $\sigma$  and the turbulent burning velocity  $S_t$ . This idea is fundamentally different from the critical gradient model proposed by Lewis and von Elbe, since it includes the effect of the flame on the upstream flow. Before Hoferichter's model is explained a number of relevant physical concepts will be discussed. Knowledge of those is required to understand the assumptions in the model.

## 2.2 Relevant Physical Concepts

Prior to a description of Hoferichter's BLF model a number of physical concepts will be explained. Knowledge of those is required for full understanding of the model and its assumptions.

### 2.2.1 Stratford Separation Criterion

Considering the turbulent boundary layer with an inner and outer region, the Stratford criterion assumes that the kinetic energy profile in the outer region stays similar in shape, because the shear forces are small compared to the pressure gradient and inertial forces. In the inner region a balance between pressure gradient and shear stress is formed, which results in deformation of the profile. This is illustrated in Figure 9. Flow separation occurs when the profile is vertical (i.e.  $\partial u/\partial y = 0$ ) at the wall. Together with two joining conditions between the inner and outer region: continuity ( $u = u$ ) and first-order smoothness ( $\partial u/\partial y = \partial u/\partial y$ ), Stratford [23] derived the separation criterion given by Equation 2.3.

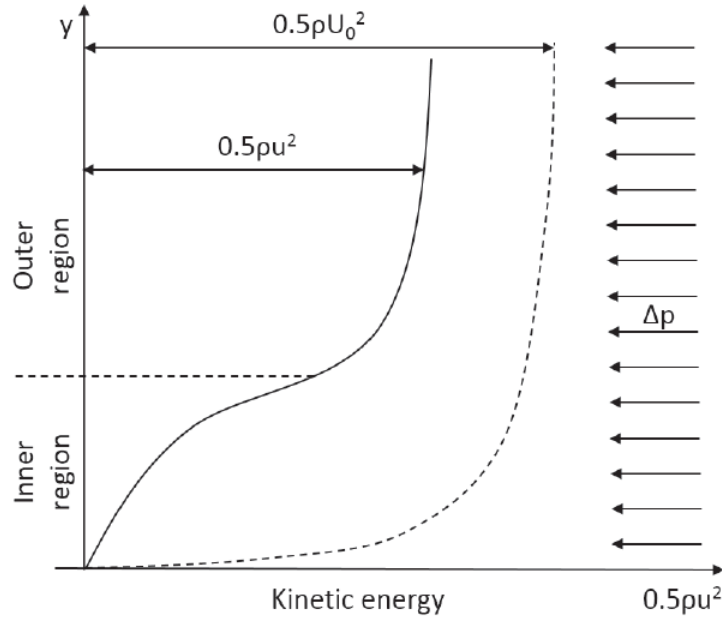


Figure 9: Development of a boundary layer subject to a pressure gradient (from Baumgartner [19]).

$$(2 \cdot \bar{C}_p)^{0.25 \cdot (n-2)} \cdot \left( \bar{x} \frac{d\bar{C}_p}{d\bar{x}} \right)^{0.5} = 1.06 \cdot \beta (10^{-6} \cdot \overline{\text{Re}}_x)^{0.1} \quad (2.3)$$

$$\bar{C}_p = \frac{p - p_m}{0.5 \cdot \rho u_m^2} \quad (2.4)$$

$$\overline{\text{Re}}_x = \frac{u_m \bar{x}_m \rho}{\mu} \quad (2.5)$$

$$\bar{x} = x - (x_m - \bar{x}_m) \quad (2.6)$$

$$\bar{x}_m = \int_0^{x_m} \left( \frac{u_e}{u_m} \right)^3 dx \quad (2.7)$$

$$\text{with: } \beta = 0.66 \text{ for } \frac{d^2 p}{dx^2} < 0 \quad \beta = 0.73 \text{ for } \frac{d^2 p}{dx^2} \geq 0 \quad (2.8)$$

$$\text{and: } n = 6 \text{ for } \overline{\text{Re}}_x \leq 10^6 \quad n = 8 \text{ for } \overline{\text{Re}}_x > 10^8 \quad (2.9)$$

In these equations  $\bar{C}_p$  is the pressure coefficient,  $x_m$  is the x-location of minimum pressure  $p_m$ . The maximum velocity at  $x_m$  is  $u_m$  and  $u_e$  is the free stream velocity. An effective downstream distance is defined as  $\bar{x}_m$  and  $\bar{x}$  is the effective origin. An bar means that the parameter is calculated w.r.t. the effective origin. For most applications  $\beta = 0.73$  and  $n = 6$  and this results in Equation 2.10.

$$\frac{\bar{C}_p \left( \bar{x} \frac{d\bar{C}_p}{d\bar{x}} \right)^{0.5}}{(\overline{\text{Re}}_x \cdot 10^{-6})^{0.1}} = 0.39 \quad (2.10)$$

Tavoularis [24] considers three cases and they are illustrated in Figure 10.

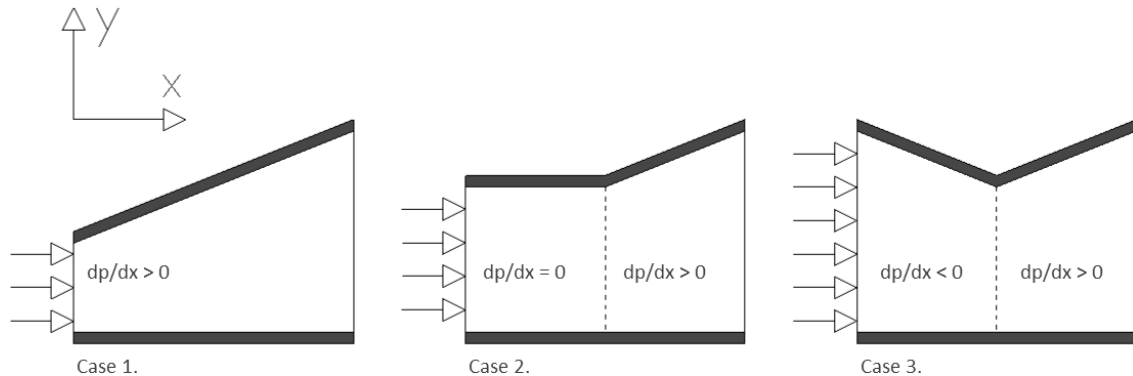


Figure 10: Three cases with each a different pressure gradient.

1. **Only a positive pressure gradient:** This is illustrated with a diverging channel, since a decrease in velocity (due to divergence) results in an increase of pressure. The

minimum pressure is found at the inlet and therefore  $x_m = 0$ ,  $p_m$  is the minimum pressure at  $x_m$  and  $u_m$  is the maximum velocity at  $x_m$ . Also, with  $x_m = 0$ ,  $\bar{x} = x$  and the Reynolds number effect disappears (since there is no downstream dependency in front of the inlet). For this specific case Equation 2.10 simplifies to:

$$\bar{C}_p \left( x \frac{d\bar{C}_p}{dx} \right)^{0.5} = 0.39 \quad (2.11)$$

2. **A zero pressure gradient followed by a positive pressure gradient:** Now  $x_m$  is found at the location of minimum pressure  $p_m$  and the maximum velocity at  $x_m$  is  $u_m$ . Similar to case 1, the effective origin  $\bar{x} = x$  meaning that  $\bar{x}_m = x_m$ . However, the Reynolds number will now be included (based on  $x_m$  instead of  $\bar{x}_m$ ) to account for downstream dependency. This results in:

$$\frac{\bar{C}_p \left( x \frac{d\bar{C}_p}{dx} \right)^{0.5}}{(\text{Re}_x \cdot 10^{-6})^{0.1}} = 0.39 \quad (2.12)$$

$$\text{Re}_x = \frac{u_m x_m \rho}{\mu} \quad (2.13)$$

3. **A negative pressure gradient followed by a positive pressure gradient:** Similar to case 2, but now  $x_m$  is not equal to  $\bar{x}_m$ . Evaluating the integral of Equation 2.7, with  $u_e$  and  $u_m$  constant along  $x$ , results in the following equations:

$$\bar{x}_m = \left( \frac{u_e}{u_m} \right)^3 x_m \quad (2.14)$$

$$\bar{x} = x - \left( \left( \frac{u_e}{u_m} \right)^3 - 1 \right) x_m \quad (2.15)$$

$$\overline{\text{Re}}_x = \frac{u_m \bar{x}_m \rho}{\mu} \quad (2.16)$$

$$\frac{\bar{C}_p \left( \bar{x} \frac{d\bar{C}_p}{d\bar{x}} \right)^{0.5}}{(\overline{\text{Re}}_x \cdot 10^{-6})^{0.1}} = 0.39 \quad (2.17)$$

## 2.2.2 Turbulent Burning Velocity

To describe the turbulence-flame interaction on a macroscopic scale, five different flame regimes are defined, illustrated by Figure 11. The parameters involved are the turbulent macroscale  $\Lambda$ , the turbulent fluctuations  $u'$ , the laminar flame thickness  $\delta_f$  and the unstretched laminar burning velocity  $S_{l,0}$ , or in other words: the length and velocity scales for the turbulent flow and the flame, respectively.

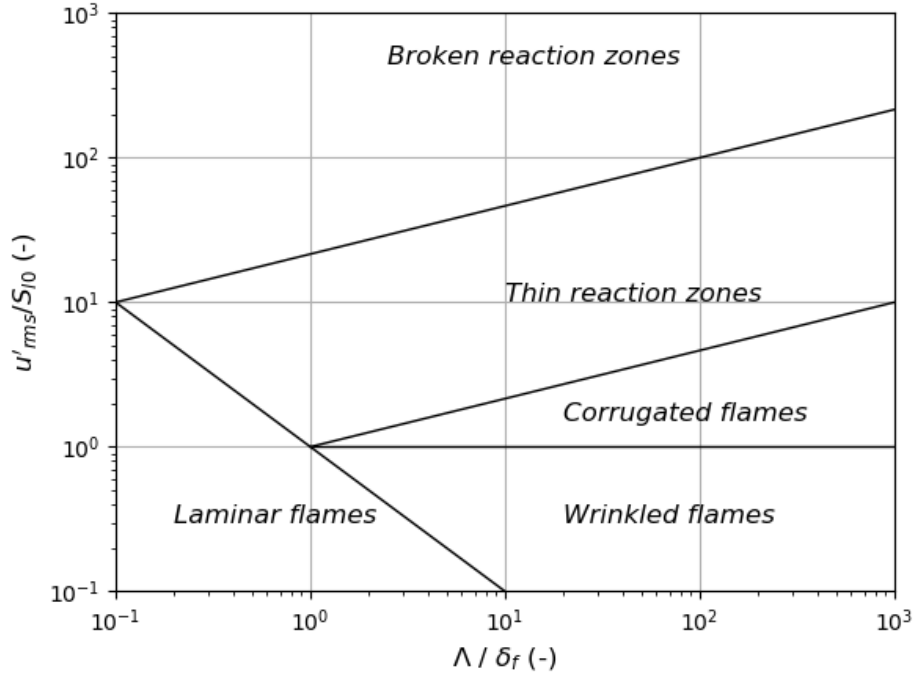


Figure 11: Flame regimes based on the turbulent macroscale and fluctuations, laminar flame thickness and laminar burning velocity (based on Peters [25]).

1. **Laminar flames:** Although turbulent fluctuations might exist, they are too small to influence the combustion process.
2. **Wrinkled flames:** The flame front is only weakly wrinkled, because the velocity fluctuations are smaller than the laminar flame speed. The dominant parameter is the laminar burning velocity.
3. **Corrugated flames:** Compared to the wrinkled flame domain, the wrinkles are now significantly stronger, due to the higher turbulent fluctuations. This results in a larger flame surface and thus in higher consumption speeds. Since the Kolmogorov scale  $\eta$  is still larger than the flame thickness  $\delta_f$ , the eddies do not influence the processes inside the flame. The upper limit of this domain is given by the Karlovitz number being equal to one. The Karlovitz number  $Ka$  and the reciprocal, the Damköhler number  $Da$ , are defined as:

$$Ka = \frac{1}{Da} = \left( \frac{u'}{S_{l,0}} \right)^{3/2} \left( \frac{\delta_f}{\Lambda} \right)^{1/2} \quad (2.18)$$

4. **Thin reaction zones:** Compared to the corrugated flame regime, the Kolmogorov eddies are now able to penetrate into the preheat zone (Figure 12) of the flame. Mixing,

and thus mass and heat transfer, between the preheat zone and the inner reaction layer is now possible. However, turbulence does not affect the chemical reactions.

5. **Broken reaction zones:** Unlike the regime of thin reaction zones, the Kolmogorov eddies are now small enough to also penetrate into the inner reaction zone. This results into local flame extinction, caused by heat losses to the preheat zone.

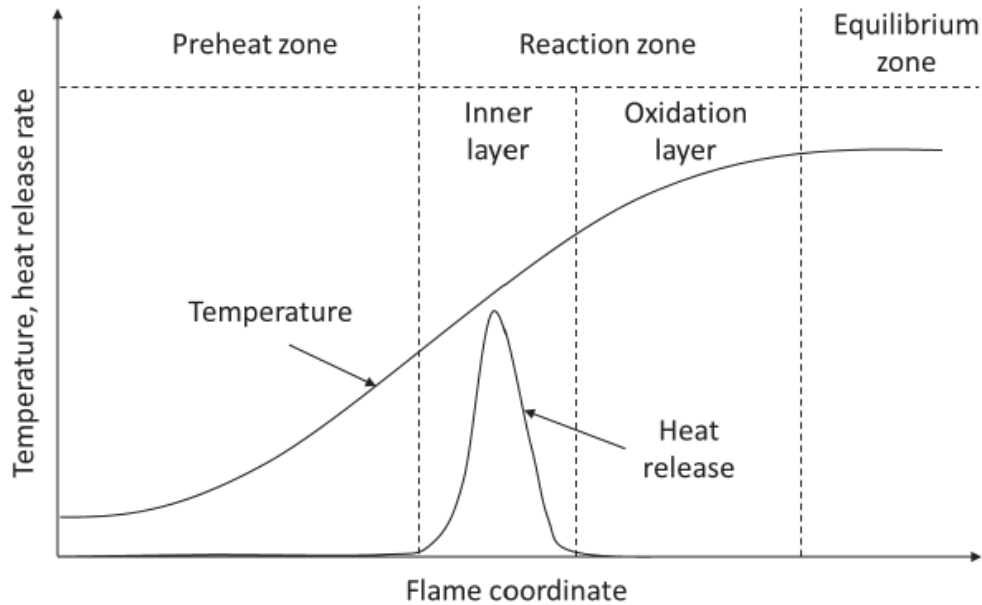


Figure 12: Zone specification in and near the flame front (from Baumgartner [19]).

The wrinkled flames, corrugated flames and the thin reaction zones can be grouped into one regime: the flamelet regime. Within this regime the local burning velocity can be considered laminar and one-dimensional. This is a powerful idea that helps defining the turbulent burning velocity  $S_t$  in terms of the laminar burning velocity  $S_l$ , the turbulent flame surface area  $A_t$  and the cross sectional area  $A$ , as given by Equation 2.19 and illustrated in Figure 13. This has been done first by Damköhler in 1940. The derivation of  $S_t$  will now be given, following notes from Peters [26].

$$\frac{S_t}{S_l} = \frac{A_t}{A} \tag{2.19}$$

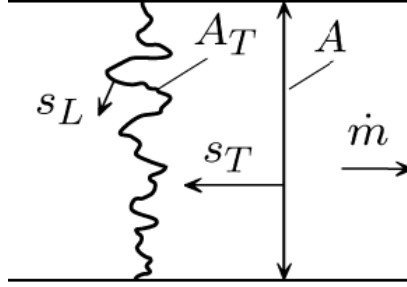


Figure 13: The turbulent burning velocity (from Peters [26]).

Damh hler identified two different regimes of premixed turbulent combustion: large scale turbulence and small scale turbulence. These regimes correspond to the *Corrugated flames* regime and the *Thin reaction zone* regime, respectively, which were illustrated in Figure 11. In case of large scale turbulence, Damk hler assumed that the only interaction between a wrinkled flame front and turbulence is the kinematic interaction. The turbulent flame area  $A_t$  is then proportional to the (root mean squared) turbulent fluctuations  $u'$ . Combining this with Equation 2.19, shows that  $S_t$  is proportional to the turbulent fluctuation:

$$\frac{A_t}{A} \sim \frac{u'}{S_l} \quad (2.20)$$

$$S_t \sim u' \quad (2.21)$$

Starting with a scaling for the laminar burning velocity in terms of the molecular diffusivity  $D$  and chemical time scale  $t_c$ , Damh hler argued that for small scale turbulence only the diffusivity (transport between the reaction zone and the unburned gas) is affected by the turbulence. Based on this assumption he defines a turbulent diffusivity  $D_t$ :

$$S_l \sim \left(\frac{D}{t_c}\right)^{1/2} \quad (2.22)$$

$$S_t \sim \left(\frac{D_t}{t_c}\right)^{1/2} \quad (2.23)$$

With the laminar diffusivity being proportional to the product of  $S_l$  and the flame thickness  $\delta_f$ , and the turbulent diffusivity proportional to the product of  $u'$  and the turbulent macroscale  $\Lambda$ , the following proportionality holds:

$$\frac{S_t}{S_l} \sim \left(\frac{u'\Lambda}{S_l\delta_f}\right)^{1/2} \quad (2.24)$$

In case of no turbulence,  $u' \rightarrow 0$ , it is expected that the turbulent and laminar burning velocity are equal. Also, the ratio of  $\Lambda$  and  $\delta_f$  can be written as a constant  $C$ . Together this results in:

$$\frac{S_t}{S_l} = 1 + C \left( \frac{u'}{S_l} \right)^{1/2} \quad (2.25)$$

Based on the work of Damh hler many more and different correlations have been developed to describe  $S_t$ . An overview of the many expressions for  $S_t$  is given by Burke [27]. They depend on many different parameters: Damk hler number  $Da$ , laminar burning velocity  $S_l$ , turbulent fluctuations  $u'$ , turbulent Reynolds number  $Re_t$ , turbulent flame area  $A_t$ , Lewis number  $Le$  and a number of constants. In almost all relations  $S_t$  is expressed in terms of  $S_l$  and this is in line with the definition given by Equation 2.19. According to Figure 14 the laminar burning velocity for lean premixed hydrogen-air mixtures is well known (compared to rich mixtures). The uncertainty is in the relation between  $S_t$  and  $S_l$  and therefore the hydrogen related correlations between  $S_t$  and  $S_l$  will now be presented.

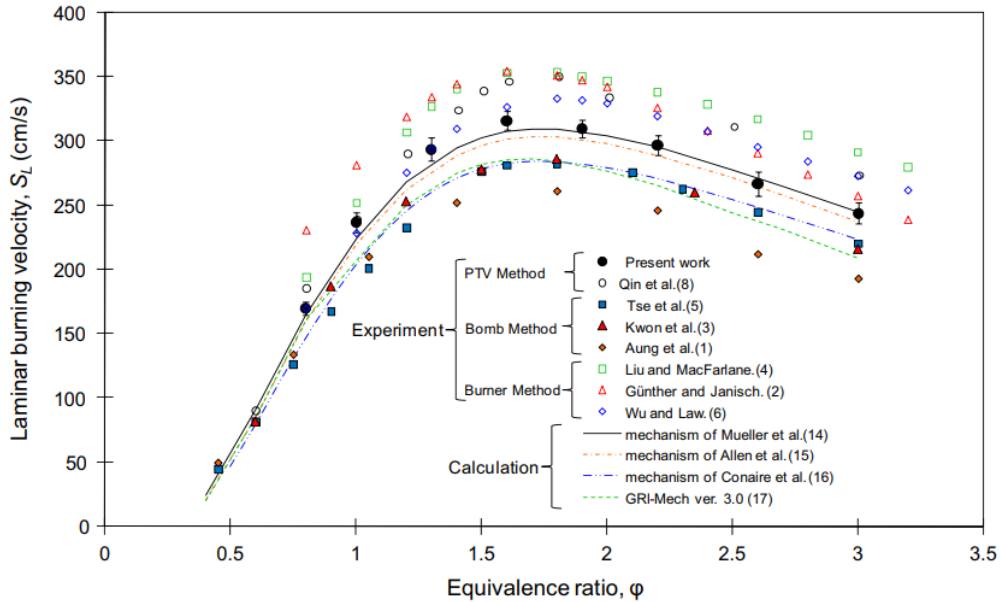


Figure 14: Laminar burning velocity of premixed hydrogen-air against equivalence ratio (from Pareja [28]).

In 1993 Koroll [29] obtained laminar and turbulent burning velocities of hydrogen-air mixtures, by performing measurements in a 17-L vessel using the double-kernel technique. He proposed a correlation which is based on the measured flammability limits and this is in good agreement with the measured burning velocities. His correlation depends on the turbulent fluctuations  $u'$  and the expansion ratio  $\sigma$ :

$$\frac{S_t}{S_l} = \sqrt{1 + 16 \cdot \left(\frac{u'}{S_l}\right)^2} + \left(1 - e^{-u'/S_l}\right) \frac{\sigma - 1}{\sqrt{3}} \quad (2.26)$$

In 2011 Daniele [30] performed research on the turbulent flame speed for syngas at gas turbine relevant conditions. Experiments up to a pressure of 2 MPa and a temperature of 773 K are presented with a maximum hydrogen percentage of 67 %. The proposed correlation depends on the turbulent macroscale  $\Lambda$ , the flame thickness  $\delta_f$ , the pressure  $P$  and the temperature  $T$ . The reference temperature  $T_0$  is 1 K and the reference pressure  $P_0$  is 0.1 MPa:

$$\frac{S_t}{S_l} = 337.5 \cdot \left(\frac{u'}{S_l}\right)^{0.63} \left(\frac{\Lambda}{\delta_f}\right)^{-0.37} \left(\frac{P}{P_0}\right)^{0.63} \left(\frac{T}{T_0}\right)^{-0.63} \quad (2.27)$$

Finally, in 2014 Lin [31] presented a study on turbulent flame speed for hydrogen-rich fuel gases at gas turbine relevant conditions. The correlation he proposes includes an effective Lewis number  $Le_{eff}$  and is valid for both syngas and hydrogen-air mixtures. The reference pressure  $P_0$  and temperature  $T_0$  are 0.1 MPa and 293 K, respectively. According to Lin, the correlation matches available data with a maximum error of 20%. This data includes 100% hydrogen at an inlet temperature of 623 K. The correlation reads:

$$\frac{S_t}{S_{l:0}} = 10.5 \cdot Le_{eff}^{-0.82} \left(\frac{u'}{S_{l:0}}\right)^{0.45} \left(\frac{\Lambda}{\delta_f}\right)^{-0.41} \left(\frac{P_0}{P}\right)^{0.75} \left(\frac{T_0}{T}\right)^{-1.33} \quad (2.28)$$

### 2.2.3 Stretched Laminar Burning Velocity

One of the few flames where all speeds can be defined and measured is the unstretched planar flame. However, due to flame stretch the flame speed differs and becomes harder to calculate numerically and to measure experimentally. Poinot [32] suggest that, in the limit of low flame stretch, this is the only parameter affecting the flame structure. This results in a linear relationship between the displacement and consumption speeds and defines the stretched laminar burning velocity  $S_{l,s}$ :

$$S_{l,s} = S_{l,0} - \kappa L_M \quad (2.29)$$

It depends on the unstretched laminar burning velocity  $S_{l,0}$ , the flame stretch rate  $\kappa$  and the Markstein length  $L_M$ . The Markstein length is defined as the reduction of the laminar burning velocity caused by stretch and is fuel dependent. The flame stretch rate  $\kappa$  is defined as the normalized temporal change of laminar flame surface area and can be caused by a curvature in the flame front,  $\kappa_c$ , or by hydrodynamic strain,  $\kappa_s$ . Chong [33] differentiates

between a mean and a turbulent strain component, resulting in the corresponding flame stretch rates  $\kappa_{mean}$  and  $\kappa_t$ , respectively.

$$\kappa = \frac{1}{A} \frac{dA}{dt} \quad (2.30)$$

$$= \kappa_c + \kappa_{mean} + \kappa_t \quad (2.31)$$

Starting with Equation 2.32 Chong uses Reynolds-averaging to separate  $\kappa_{mean}$  and  $\kappa_t$  to get Equation 2.33. This equation includes the Kronecker delta  $\delta_{ij}$ , the Favre-averaged orientation factors  $\langle n_i n_j \rangle$  and partial derivatives of the averaged velocity components. Chong relates the orientation factors to the (time) averaged Reynolds stresses  $\overline{u'_i u'_j}$  and the turbulent kinetic energy  $k$ , proposed by Veynante [34], shown in Equation 2.34.

$$\kappa_{mean} + \kappa_t = (\delta_{ij} - n_i n_j) \frac{\partial u_i}{\partial x_j} \quad (2.32)$$

$$\kappa_{mean} = (\delta_{ij} - \langle n_i n_j \rangle) \frac{\partial \bar{u}_i}{\partial x_j} \quad (2.33)$$

$$\langle n_i n_j \rangle = \frac{\overline{u'_i u'_j}}{2 \cdot k} \quad (2.34)$$

Evaluating Equation 2.33 results in Equation 2.35 and this can be written out to get Equation 2.36.

$$\kappa_{mean} = \frac{\partial \bar{u}_i}{\partial x_i} - \frac{\overline{u'_i u'_j}}{2 \cdot k} \frac{\partial \bar{u}_i}{\partial x_j} \quad (2.35)$$

$$= \left( \frac{\partial \bar{u}}{\partial x} + \frac{\partial \bar{v}}{\partial y} + \frac{\partial \bar{w}}{\partial z} \right) - \frac{1}{2 \cdot k} \left[ \overline{u' u'} \frac{\partial \bar{u}}{\partial x} + \overline{u' v'} \frac{\partial \bar{u}}{\partial y} + \overline{u' w'} \frac{\partial \bar{u}}{\partial z} \right. \\ \left. + \overline{v' u'} \frac{\partial \bar{v}}{\partial x} + \overline{v' v'} \frac{\partial \bar{v}}{\partial y} + \overline{v' w'} \frac{\partial \bar{v}}{\partial z} + \overline{w' u'} \frac{\partial \bar{w}}{\partial x} + \overline{w' v'} \frac{\partial \bar{w}}{\partial y} + \overline{w' w'} \frac{\partial \bar{w}}{\partial z} \right] \quad (2.36)$$

Chong relates the turbulent component of the flame stretch rate,  $\kappa_t$ , to an efficiency function  $\Gamma_K$ , the turbulence dissipation rate  $\varepsilon$  and the turbulent kinetic energy  $k$ . The  $\Gamma_k$  function is proposed by Meneveau and Poinot [35]. It depends, among other parameters, on  $s$ , which is a function of the turbulent macroscale  $\Lambda$  and the flame thickness  $\delta_f$ .

$$\kappa_t = \Gamma_K \frac{\varepsilon}{k} \quad (2.37)$$

$$\log_{10}(\Gamma_K) = (1 - e^{-(s+0.4)}) \left( \frac{2}{3} \cdot \left( 1 - \frac{1}{2} \cdot e^{-(u'/S_{t,0})^{1/3}} \right) s - 0.11 \right) - \frac{1}{s+0.4} e^{-(s+0.4)} \quad \text{with: } s = \log_{10} \left( \frac{\Lambda}{\delta_f} \right) \quad (2.38)$$

## 2.2.4 Markstein Length

The most elaborate expression of the Markstein length is given by Giannakopoulos [36], given by Equation 2.39. It includes the laminar flame thickness  $\delta_f$ , the expansion ratio  $\sigma$ , the thermal conductivity  $\lambda$  and the two dimensional numbers: Ze and Le. The Zel'dovich number Ze is a quantitative number for the activation energy. The Lewis number Le is the ratio of thermal diffusivity to mass diffusivity. Taylor [37] proposes the simpler Equation 2.40, which does not include a temperature dependence.

$$L_M = \delta_f \left( \frac{1}{\sigma - 1} \int_1^\sigma \frac{\lambda(x)}{x} dx + \frac{Ze(Le - 1)}{2 \cdot (\sigma - 1)} \int_1^\sigma \ln \left( \frac{\sigma - 1}{x - 1} \right) \frac{\lambda(x)}{x} dx \right) \quad (2.39)$$

$$L_M = \frac{\delta_f \sigma}{1 - \sigma} \left( \ln \left( \frac{1}{\sigma} \right) + \frac{Ze(Le - 1)}{2} \int_0^{\frac{1-\sigma}{\sigma}} \frac{\ln(1+x)}{x} dx \right) \quad (2.40)$$

The Lewis numbers for lean hydrogen-air mixtures are below 1 ( 0.4). This results in a thermo-diffusive instability during combustion: The flame sucks fresh fuel faster towards it than it diffuses heat, and therefore, locally, the fuel becomes richer. Mathematically a low Lewis number leads to a negative Markstein length. This means that a positive flame stretch rate results in a higher burning velocity. However, both equations are based on asymptotic theory, such that they are only valid under the following conditions:

- The Lewis number Le is close to 1
- Only a single-step reaction is considered
- The composition is far from stoichiometric
- The product of density and thermal diffusivity is constant

For low Lewis numbers the first condition is not met. Taylor mentions that for lean hydrogen mixtures this model is indeed not suitable, although there are no better approximations. He also mentions that the Markstein length of lean hydrogen-air mixtures cannot be obtained accurately by experiments (with the method of spherical expanding flames), due to early onset of flame cellularity. In other words, the Markstein length is hard to determine, both experimentally and by calculations.

### 2.2.5 Turbulence

This paragraph (2.2.5) is based on a book from Nieuwstadt [38]. Turbulent flow is a fluid flow with chaotic fluctuations of the velocity in both direction and magnitude. One way of describing turbulence is by decomposing the instantaneous velocity into an average and fluctuating term. This is called the Reynolds decomposition and this is shown in Equation 2.41, where  $\bar{u}_i$  is the time-averaged velocity and  $u'_i$  is the fluctuation.

$$u_i = \bar{u}_i + u'_i \quad (2.41)$$

Internal flows (pipe and channel flows) become turbulent when the Reynolds becomes larger than 2700. This is an approximation: the transition from laminar to turbulent flow does not occur instantaneously. The Reynolds number is calculated with the (hydraulic) diameter, shown in Equation 2.42:

$$\text{Re}_D = \frac{\rho U D}{\mu} \quad (2.42)$$

A horizontal flow is called fully developed when the flow is stationary ( $\partial/\partial t = 0$ ) and horizontally homogeneous ( $\partial/\partial x = 0$  for the velocity terms). In such a flow there is a balance between the pressure gradient and the wall shear force. The velocity profiles, both averaged and fluctuating, have a fixed shape. Figure 15 shows the profile of the mean flow. From the inlet of a pipe/channel the flow needs a certain entrance length to become fully developed. This length is typically estimated as 10 times the (hydraulic) diameter.

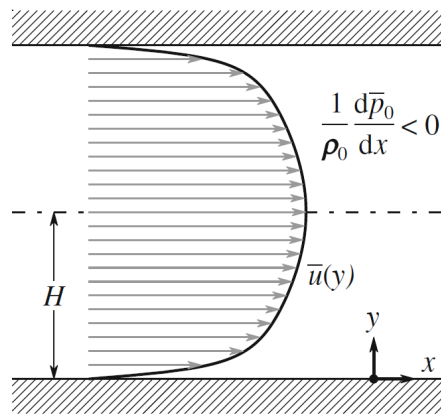


Figure 15: Fully developed turbulent velocity profile (from Nieuwstadt [38]).

When the velocity fluctuations are invariant to rotations and reflections the turbulence is called isotropic. In this case the principal Reynold stresses are equal and the shear terms drop out:

$$\overline{u'u'} = \overline{v'v'} = \overline{w'w'} \quad (2.43)$$

$$\overline{u'_i u'_j} = 0 \quad \text{for: } i \neq j \quad (2.44)$$

Fluctuations in the boundary layer are shown in Figures 16 and 17 for a pipe and channel, respectively.

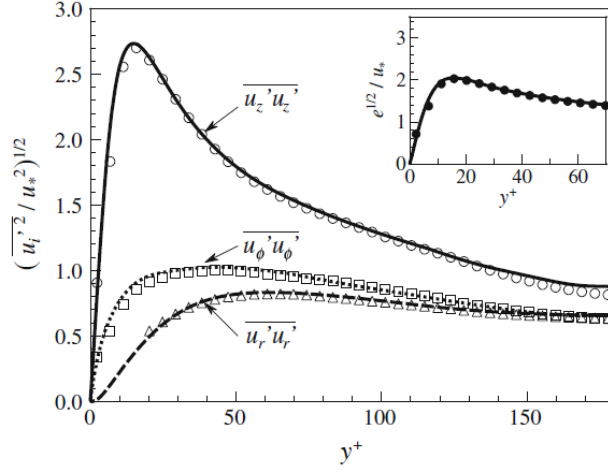


Figure 16: Fluctuations in the boundary layer of a pipe with  $Re = 5,300$ ,  $z$  the axial,  $r$  the radial and  $\phi$  the circumferential direction (from Nieuwstadt [38]).

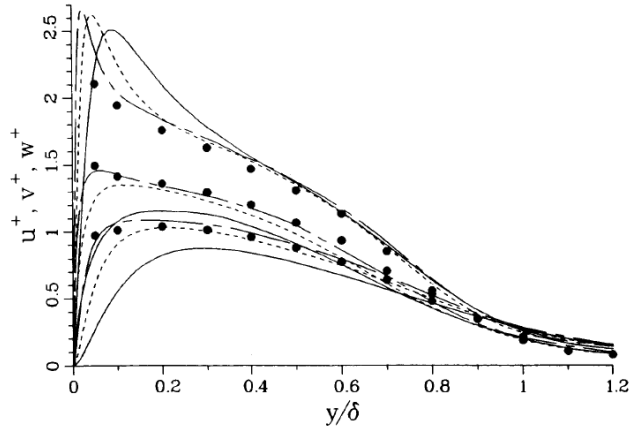


Figure 17: DNS studies showing fluctuations in the boundary layer of a channel, with  $u$  the upper,  $v$  the lower and  $w$  the middle curves.  $Re$  ranges from 300 to 7,500 (from Spalart [39]).

In the boundary layer a dimensional wall distance  $y^+$  is used, which is defined as:

$$y^+ = \frac{u_\tau y \rho}{\mu} \quad \text{with: } u_\tau^2 = \nu \frac{\partial \bar{u}}{\partial y} \quad (2.45)$$

## 2.3 Hoferichter's Model

This section explains how Hoferichter's model works and what assumptions are used. The model description starts with the Stratford separation criterion and the model output is an inlet bulk velocity for which flashback occurs. The description is followed by a comparison to experiments and a discussion.

### 2.3.1 Model Description

This paragraph (2.3.1) is based on the PhD thesis from Hoferichter [10] and one of her articles [21]. Hoferichter starts with the Stratford criterion given by Equation 2.46, because she assumes fully developed flow to neglect the downstream dependency. Then she defines a quadratic function for the pressure rise upstream of the flame (due to presence of the flame). This function is valid from  $x = 0$  to  $x_f$ , where  $x_f$  is the distance from the point of flow separation to the flame tip. Baumgartner [19] proposes a  $x_f$  of 10 mm. Together this leads to Equations 2.46 to 2.50.

$$\bar{C}_p \left( x \frac{d\bar{C}_p}{dx} \right)^{0.5} = 0.39 \quad (2.46)$$

$$p(x) = p(0) + \frac{\Delta p}{x_f^2} x^2 \quad \text{for: } x_f \geq x \geq 0 \quad (2.47)$$

$$C_p(x) = \frac{p(x) - p(0)}{0.5 \cdot \rho_u U^2} \quad (2.48)$$

$$= \frac{2 \cdot \Delta p x^2}{\rho_u U^2 x_f^2} \quad (2.49)$$

$$\frac{dC_p(x)}{dx} = \frac{4 \cdot \Delta p x}{\rho_u U^2 x_f^2} \quad (2.50)$$

In these equations  $\rho_u$  stands for the density of the unburned gas. The velocity  $U$  is the centerline velocity in  $x$  direction, which will from now on be called  $U_{FB}$ , referring to the centerline velocity limiting flashback. Rewriting yields:

$$\sqrt{2} \cdot \left( \frac{2 \cdot \Delta p}{\rho_u U_{FB}^2} \right)^{3/2} = 0.39 \quad (2.51)$$

Equation 2.51 is the separation criterion that relates the flame backpressure  $\Delta p$  to the centerline velocity at flashback conditions  $U_{FB}$ . The backpressure is defined by considering the continuity and momentum balance over the flame and by setting the velocity of the unburned gas  $u_u$  equal to the turbulent burning velocity  $S_t$ :

$$\rho_u u_u = \rho_b u_b \quad (2.52)$$

$$\rho_u u_u^2 + p_u = \rho_b u_b^2 + p_b \quad (2.53)$$

$$\Delta p = p_u - p_b \quad (2.54)$$

$$= \rho_b u_b^2 - \rho_u u_u^2 \quad (2.55)$$

$$= \rho_u S_t^2 \left( \frac{\rho_u}{\rho_b} - 1 \right) \quad (2.56)$$

$$= \rho_u S_t^2 (\sigma - 1) \quad (2.57)$$

By assuming an ideal gas the density ratio  $\sigma$  is replaced by the temperature ratio (in Kelvin) over the flame, where  $T_{ad}$  is the adiabatic temperature and  $T_u$  the unburned gas temperature:

$$\Delta p = \rho_u S_t^2 \left( \frac{T_{ad}}{T_u} - 1 \right) \quad (2.58)$$

For the turbulent burning velocity Hoferichter uses the expression derived by Damköhler, Equation 2.25. The constant  $C$  is determined with a best-fit-method by comparing predicted flashback velocities to experimental results from Eichler [7].

Due to large deviations found in literature for values of  $S_{l,0}$  at preheated temperatures, Hoferichter proposes a polynomial function based on free flame simulations. In her PhD thesis Hoferichter tabulates the coefficients for 5 different pressures (1, 3, 5, 7 and 20 bar), each for  $\phi = 0.35, 0.40..1.30$ . The dependency of  $S_{l,0}$  on the unburned pressure  $p_u$  and the equivalence ratio  $\phi$  is included in the polynomial coefficient, while the unburned temperature  $T_u$  is directly included in the equation:

$$S_{l,0} = b_7 T_u^3 + b_8 T_u^2 + b_9 T_u + b_{10} \quad (2.59)$$

The stretched laminar burning velocity is approximated with the linear relation proposed by Poinot [32], Equation 2.29. Like Equation 2.31, Hoferichter differentiates between  $\kappa_c$ ,  $\kappa_{mean}$  and  $\kappa_t$ . She relates  $\kappa_c$  to  $S_{l,0}$ , the Reynolds averaged reaction progress variable  $\bar{c}$  and the flame wrinkling length  $L$ . The latter is a function of the turbulent macroscale  $\Lambda$ ,  $S_{l,0}$  and  $u'$ . Combining these relations and setting  $\bar{c}$  equal to zero (to assess the maximum stretch rate) results in Equation 2.61.

$$\kappa_c \approx S_{l,0} \frac{0.5 - \bar{c}}{L} \quad \text{with: } L = \Lambda \frac{S_{l,0}}{u'} \quad (2.60)$$

$$\kappa_c = \frac{1}{2} \cdot \frac{u'}{\Lambda} \quad (2.61)$$

Under the assumption of isotropic turbulence, Hoferichter follows Chong's [33] simplification for the mean strain-induced flame stretch rate, given by Equation 2.62 (in Einstein notation). By considering fully developed flow only (and continuity for incompressible flow)  $\kappa_{mean}$  becomes zero. The turbulence-induced flame stretch rate  $\kappa_t$  is evaluated by approximating  $\varepsilon$  and  $k$  in terms of  $u'$  and is also based on isotropic turbulence:

$$\kappa_{mean} = \frac{2}{3} \cdot \frac{\partial u_i}{\partial x_i} = 0 \quad (2.62)$$

$$\varepsilon \approx \frac{(u')^3}{\Lambda} \quad (2.63)$$

$$k \approx \frac{3}{2} \cdot (u')^2 \quad (2.64)$$

$$\kappa_t = \frac{2}{3} \cdot \Gamma_K \frac{u'}{\Lambda} \quad (2.65)$$

For the Markstein length Hoferichter uses an asymptotic approach proposed by Bechtold and Matalon [40], which relates the Markstein length to the laminar flame thickness  $\delta_f$ , the expansion ratio  $\sigma$ , the Zel'dovich number  $Ze$ , the Lewis number  $Le$  and the constants  $\gamma_1$  and  $\gamma_2$ . By assuming a linear dependency of the thermal conductivity on temperature,  $\gamma_1 = \sigma$  and  $\gamma_2 = 1$ . The laminar flame thickness is expressed in terms of the thermal conductivity  $\lambda_u$ , the density  $\rho_u$  and the specific heat capacity for constant pressure  $c_{p:u}$ .

$$L_M = \delta_f \left( \gamma_1 + 0.5 \cdot Ze(Le - 1)\gamma_2 - (\sigma - 1) \frac{\gamma_1}{\sigma} \right) \quad (2.66)$$

$$= \delta_f (1 + 0.5 \cdot Ze(Le - 1)) \quad (2.67)$$

$$\delta_f = \frac{2 \cdot \lambda_u}{\rho_u c_{p:u} S_{l0}} \quad (2.68)$$

An effective Lewis number is calculated for the hydrogen oxygen mixture by making use of a blending factor  $a$  and the Lewis numbers of hydrogen and oxygen.

$$\text{Le} = 1 + \frac{\text{Le}_{O_2} - 1 + a(\text{Le}_{H_2} - 1)}{1 + a} \quad \text{with: } \text{Le}_{O_2} = 2.32, \text{Le}_{H_2} = 0.33 \quad (2.69)$$

$$a = 1 + \text{Ze} \left( \frac{1}{\phi} - 1 \right) \quad (2.70)$$

$$\text{Ze} = \frac{E_a(T_{ad} - T_u)}{RT_{ad}^2} \quad (2.71)$$

The turbulent fluctuations  $u'$  is required to determine both  $\Gamma_K$  and  $S_t$ . Hoferichter proposes a standard fluctuations profile as a function of  $y^+$  and  $u_\tau$ , given by Equation 2.72. This function is a fit through experimental results of fully developed flow and is used with the assumption that the flame has no effect on upstream turbulence. Equations 2.73 and 2.74 are used to obtain the friction velocity  $u_\tau$  for a circular and rectangular cross section, respectively.

$$\frac{u'}{u_\tau} = 2.661 - 7.211 \cdot \ln(y^+) + 7.600 \cdot \ln(y^+)^2 - 2.900 \cdot \ln(y^+)^3 + 0.472 \cdot \ln(y^+)^4 - 0.028 \cdot \ln(y^+)^5 \quad (2.72)$$

$$u_\tau = \sqrt{0.03955 \cdot (U_{FB} - 2.4 \cdot u_\tau)^{7/4} \left( \frac{\mu_u}{\rho_u} \right)^{1/4} (D)^{-1/4}} \quad (2.73)$$

$$\frac{U_{FB} - 2.4 \cdot u_\tau}{u_\tau} = \frac{1}{K} \ln \left( \frac{hu_\tau \rho_u}{2 \cdot \mu_u} \right) + B - \frac{1}{K} \quad \text{with: } K = 0.41, B = 5 \quad (2.74)$$

Note that both Equations 2.73 and 2.74 depend on  $U_{FB}$ , which is the output of the model. This means that the complete model needs to be solved iteratively. An estimate of  $U_{FB}$  is needed for  $u_\tau$ , which is required for the fluctuations. The fluctuations are required to calculate  $S_t$  and this results in the pressure increase. The pressure increase is used in the separation criterion to calculate  $U_{FB}$ .

### 2.3.2 Results and Validation

The results are compared to experiments from Eichler [7, 15], shown in Figures 18 and 19. Four sets of results are used: three of a channel flow, at different inlet temperatures and one of a pipe flow. All experiments were conducted at atmospheric pressures. Eichler presented the results in terms of the critical velocity gradient  $g_c$ , which is converted to a bulk velocity using Equation 2.75 (tube flow) or Equation 2.76 (channel flow). He calculated  $g_c$  by dividing the shear stress  $\tau$  (estimated numerically) by the kinematic viscosity  $\nu$ . Centerline velocities are converted to bulk velocities with Equation 2.77.

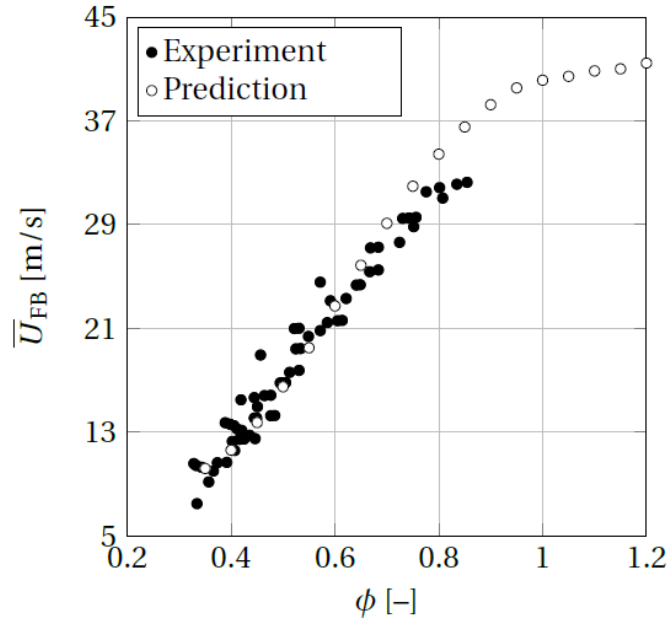


Figure 18: Comparison of Hoferichter's model to experiments from Eichler: a tube flow with of 293 K (from Hoferichter [10]).

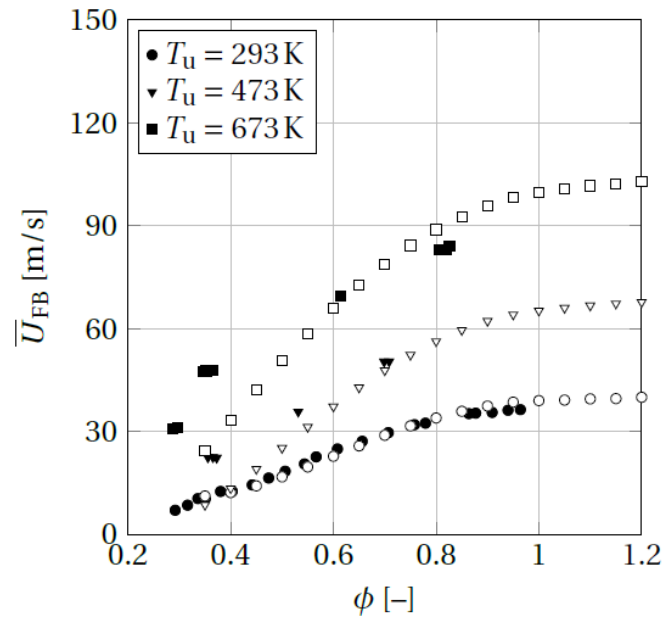


Figure 19: Comparison of Hoferichter's model to experiments from Eichler: a channel flow with different inlet temperatures (from Hoferichter [10]).

$$\bar{U}_{FB} = \left( \frac{g_c \mathcal{V}_u^{3/4} D^{1/4}}{0.03955} \right)^{4/7} \quad (2.75)$$

$$\bar{U}_{FB} = \sqrt{g_c \mathcal{V}_u} \left( \frac{1}{K} \ln \left( \frac{h \sqrt{g_c \mathcal{V}_u}}{2 \cdot \mu_u} \right) + B - \frac{1}{K} \right) \quad \text{with: } K = 0.41, B = 5 \quad (2.76)$$

$$\bar{U}_{FB} = U_{FB} - 2.4 \cdot u_\tau \quad (2.77)$$

The figures show that the BLF model accurately predicts flashback limits for room temperatures. For elevated temperatures the model underestimates, while for  $T = 673$  K at high equivalence ratios it overestimates. In her PhD thesis Hoferichter [10] performs a sensitivity analysis. Several input variables are either reduced by 20% or increased by 20% and the outcome is compared to the original results. Hoferichter concludes that the deviations between the model and the experiments could be caused by uncertainties in the temperature dependent effects of the turbulent and laminar burning velocities and the turbulent fluctuations.

### 2.3.3 Discussion

In her model Hoferichter makes a number of assumptions. The first assumption is that of fully developed flow to neglect the downstream dependency in the Stratford criterion. By calculating the hydraulic diameter the entrance length can be estimated. This is based on the channel dimensions from Eichler's [7] setup, which are given by Figure 20:

$$D_h = 2 \cdot \sqrt{\frac{wh}{\pi}} \quad (2.78)$$

$$= 2 \cdot \sqrt{\frac{0.157 \cdot 0.0175}{\pi}} = 0.059 \text{ m} \quad (2.79)$$

$$L_{en} \approx 10 \cdot D_h \quad (2.80)$$

$$= 10 \cdot 0.059 = 0.59 \text{ m} \quad (2.81)$$

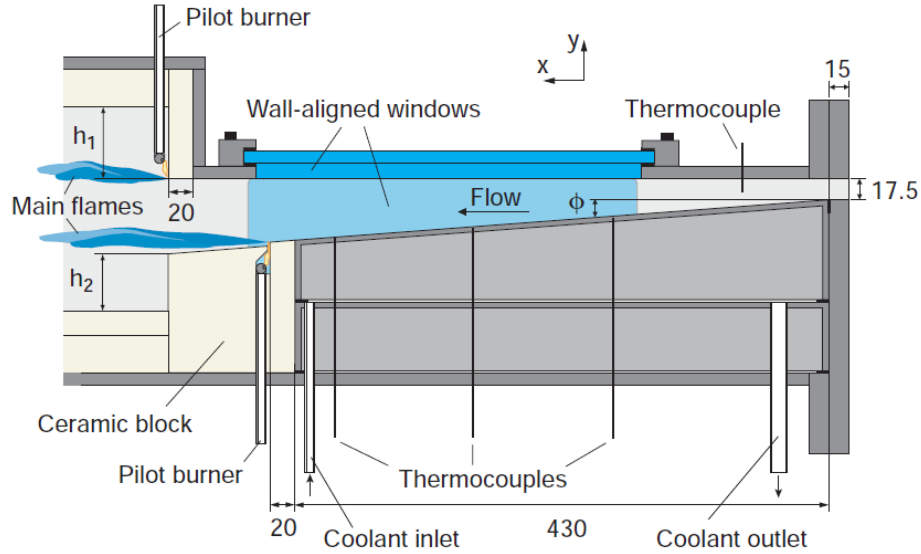


Figure 20: The channel used in Eichler's experiments (from Eichler [7]).

With a length of 0.465 m the channel is shorter than the estimated entrance length  $L_{en}$ . However, the channel (measurement section in Figure 21) inlet is connected a flow straightener and some extra piping which is longer than the measurement section. Therefore the assumption of fully developed flow is considered valid.

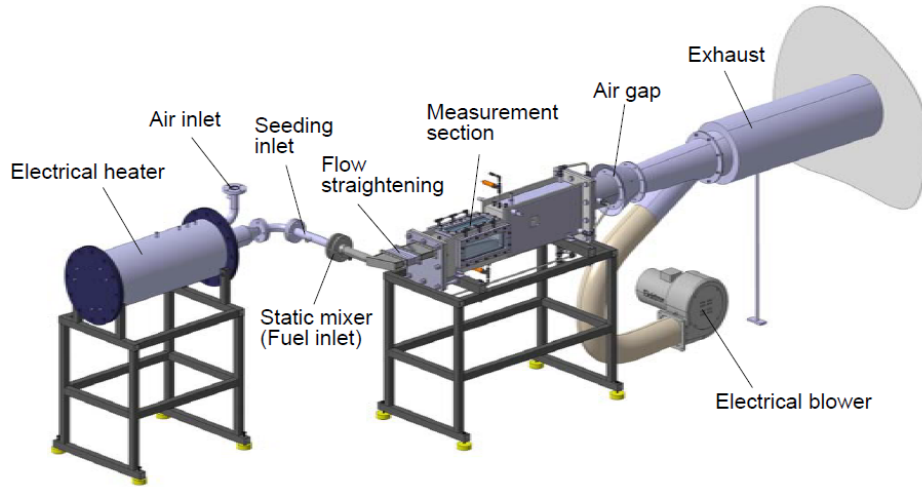


Figure 21: The whole setup used in Eichler's experiments, with the channel indicated as *Measurement section* (from Eichler [7]).

The second assumption is that of an ideal gas. This is used to replace the expansion ratio  $\sigma$  by  $T_{ad}/T_u$ . Using Cantera 2.3.0 [41] these properties have been evaluated for different  $\phi$  and  $T_u$  and are compared in Table 1. With a maximum deviation of 11.9 % the assumption of an ideal gas is acceptable.

$\phi$	$T$ in K	$\sigma$	$T_{ad}/T_u$ in K/K	Deviation in %
0.35	293	4.17	4.45	6.7
0.65	293	5.86	6.56	11.9
0.35	673	2.27	2.42	6.6
0.65	673	2.93	3.27	11.6

Table 1: Deviations from  $T_{ad}/T_u$  compared to the expansion ratio  $\sigma$ .

Another assumption is that of incompressible flow. This assumption is valid when the Mach number does not exceed 0.3 [42]. For air at atmospheric conditions this is approximately at a velocity of 100 m/s. An increasing temperature results in a high speed of sound and thus in a lower Mach number. Also, the speed of sound in hydrogen is around 4 times larger than that of ai. With all the experimental results not exceeding the velocity of 100 m/s, the assumption of incompressible flow is valid.

To calculate the flame stretch rates  $\kappa_{mean}$  and  $\kappa_t$ , Hoferichter assumes isotropic turbulence. However, it is clearly shown by Figures 16 and 17 that turbulence is far from isotropic. This assumption largely affects Equations 2.36 and 2.37 and the effect should be studied. Also, Hoferichter assumes that the effect of the flame on upstream turbulence can be neglected. The interaction between turbulence and combustion is a complex phenomena and should be studied more to validate this assumption.

Hoferichter also concludes that the effect of the Markstein length  $L_m$  on the flashback limit is negligible, since a 20% input change does hardly affect the outcome. However, this might be a premature conclusion, since the calculation of the Markstein length includes high uncertainties: different methods may result in deviations of 200% and more, which was shown in one of her articles [21].

Finally, the effect of flame instabilities is not explicitly modelled for. Gruber [18] mentions that hydrodynamic instabilities at the flame front are the responsible mechanism for flashback initiation. Eichler [7] mentions the importance of thermal-diffusive instabilities for Lewis numbers below 1, which is true for lean hydrogen-air mixtures (Figure 22). In Hoferichter’s model these instabilities are only implicitly related to the Markstein length, which is a highly uncertain parameter. With the model validation being poor for lean mixtures, where the Lewis number is low, a further study on instabilities is required.

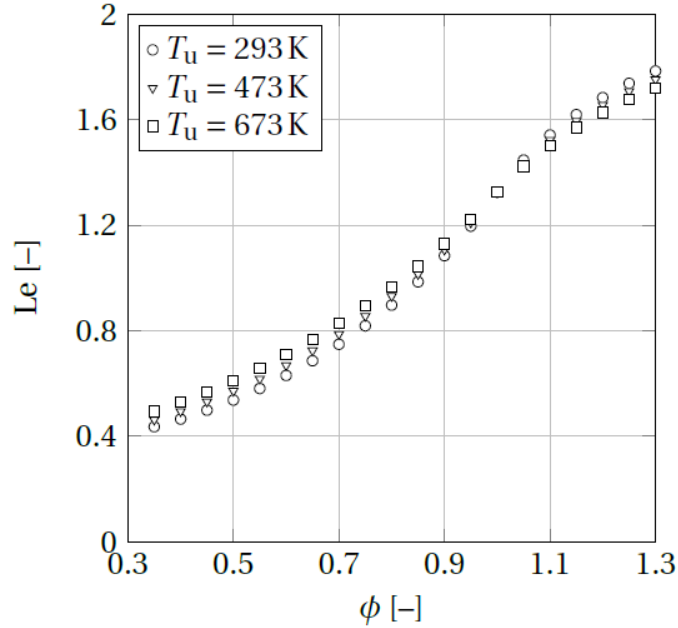


Figure 22: Lewis number for hydrogen-air mixtures at three temperatures (from Hoferichter [21]).

## 2.4 Conclusion

This chapter started with a brief historical overview of BLF models. The critical gradient model from Lewis and von Elbe was illustrated. This model is based on a comparison of the burning velocity to the flow velocity close to the wall. It does not take into account the effect of the flame on the flow. Experiments from Eichler and DNS studies from Gruber show that a mechanism between the flame and the upstream flow plays an important role in BLF. An adverse pressure gradient encourages flow separation, which initiates flashback. This theory is later used by Hoferichter to obtain the BLF model.

To fully understand Hoferichter's model first a number of physical concepts was explained: the Stratford separation criterion, the turbulent burning velocity, the stretched laminar burning velocity, the Markstein length and turbulence. This was followed by a description of Hoferichter's model and a comparison of the results to experiments. For room temperatures the model predicts very well, while for elevated temperatures at lean conditions the model underpredicts. A number of assumptions in the model were identified and validated. Some assumptions require a deeper study.

The assumption of isotropic turbulence is not valid and affects the mean strain-induced flame stretch rate  $\kappa_{mean}$  and the turbulent flame stretch rate  $\kappa_t$ . Multiplied by the highly uncertain Markstein length, they relate the unstretched to the stretched laminar burning velocity. Also, Hoferichter neglects the effect of the flame on upstream turbulence. Since the interaction between turbulence and combustion is complex, it is hard to show the effect of this assumption. The effect of both assumptions on the flashback prediction should be studied more deeply.

Two important parameters are the turbulent burning velocity  $S_t$  and the Markstein length  $L_M$ . There are many expressions for  $S_t$  that include several parameters. Hoferichter uses a simple expression derived by Damköhler, based on dimensional analysis. Other, more extensive equations are often based on empirical studies and are validated for only certain circumstances. The effect of using different expressions for  $S_t$ , that have been validated for hydrogen, should be studied.

Both hydrodynamic and thermo-diffusive instabilities are involved in lean hydrogen combustion. The Markstein length is the only parameters in Hoferichter's model that implicitly takes into account flame instabilities. However, there is not yet an accurate expression for the Markstein length and also, for lean hydrogen, it cannot be obtained experimentally. The model predicts poorly at low equivalence ratios, where the Lewis number is low and thermo-diffusive instabilities are expected. It is therefore required to study flame instabilities related.

### 3 Improvements to the Analytical Model

Based on findings of the previous chapter a number of topics is studied in more detail. These studies are used to modify the existing BLF model with the goal of improving it. Therefore, first it is explained how the BLF model is duplicated. This is followed by the three studies that include a description of the modifications:

1. **Turbulence-flame interaction:** The effect of a flame on upstream turbulence is studied here. Also the effect of another expression for the turbulent burning velocity is investigated here.
2. **Flame instabilities:** This section shows more information on the hydrodynamic Darrieus-Landau instability and the thermal-diffusive instability. These instabilities can lead to cellular flame formation. This is a different flame structure with an increasing effect on the turbulent burning velocity.
3. **Flame stretch:** More specifically the effect of anisotropic turbulence on the flame stretch rate, which affects both  $\kappa_{mean}$  and  $\kappa_t$ .

Then the results of the modifications are compared to both the original BLF model and the experiments from Eichler [7]. After a discussion a final modification is proposed. The conclusion ends the chapter by answering the following questions:

- *Where in the BLF model can improvements be made?*
- *How well does the improved model matches experiments?*

#### 3.1 Model Duplication

To duplicate Hoferichter’s model, a code has been written in Python 3.6.5 [43]. Fluid properties, both unburned and burned, are extracted from Cantera 2.3.0 [41]. When the code runs, different pre-exponential factors  $C$  are tried and the resulting  $\bar{U}_{FB}$ ’s are compared to experiments from Eichler [7], by making use of four trend lines given by Equations 3.1 to 3.4 (shown in Figure 23). An error is defined by taking the sum of the absolute differences between the predicted results and the corresponding trend line, normalized by the maximum value of the trend line. Similar to Hoferichter’s approach, an optimum value for  $C$  is chosen based on the best fit to all the results simultaneously. The complete Python code is given in the appendix (6.1). Also, the exact code modifications that are proposed in this chapter can be found in the code as well. They are grey in colour and are indicated by a ‘#’ at the begin of the line.

$$\bar{U}_{FB} = 48.12 \cdot \phi - 6.68 \quad \text{Tube, T=293 K} \quad (3.1)$$

$$\bar{U}_{FB} = 50.85 \cdot \phi - 7.28 \quad \text{Channel, T=293 K} \quad (3.2)$$

$$\bar{U}_{FB} = 78.83 \cdot \phi - 6.63 \quad \text{Channel, T=473 K} \quad (3.3)$$

$$\bar{U}_{FB} = 48.09 \cdot \ln(\phi) + 93.27 \quad \text{Channel, T=673 K} \quad (3.4)$$

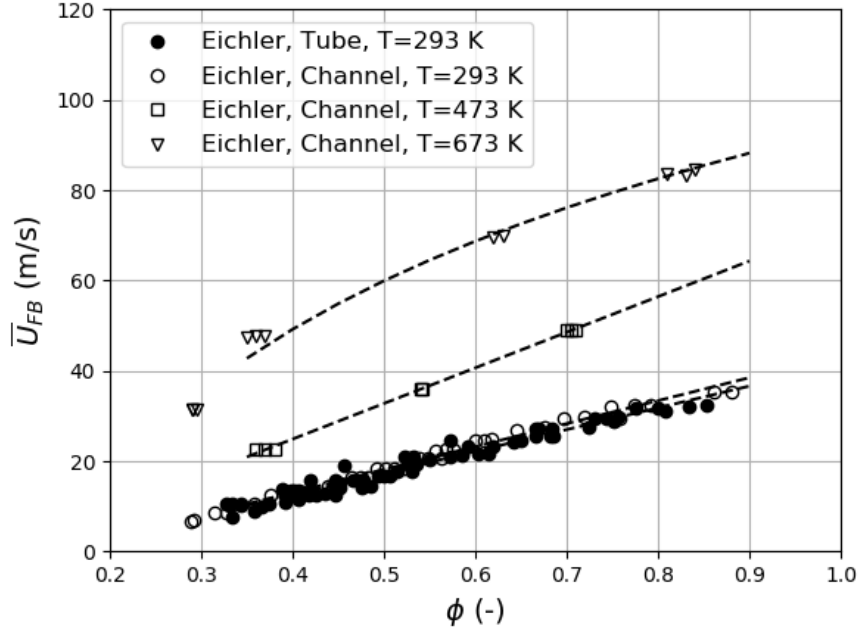


Figure 23: Experimental data converted from  $g_c$  to critical bulk velocity  $\bar{U}_{FB}$ , with corresponding trend lines (data from Eichler [7]).

Figure 24 shows the results of the Python code in a comparison to the experiments. The results are in good agreement with the predicted flashback limits provided by Hoferichter: For room temperatures the model works, while for elevated temperatures the model underpredicts (and overpredicts for high  $\phi$  at  $T = 673$  K). Also, the pre-exponential factor  $C$  was found to be 2.3, which is equal to the value Hoferichter [10] determined.

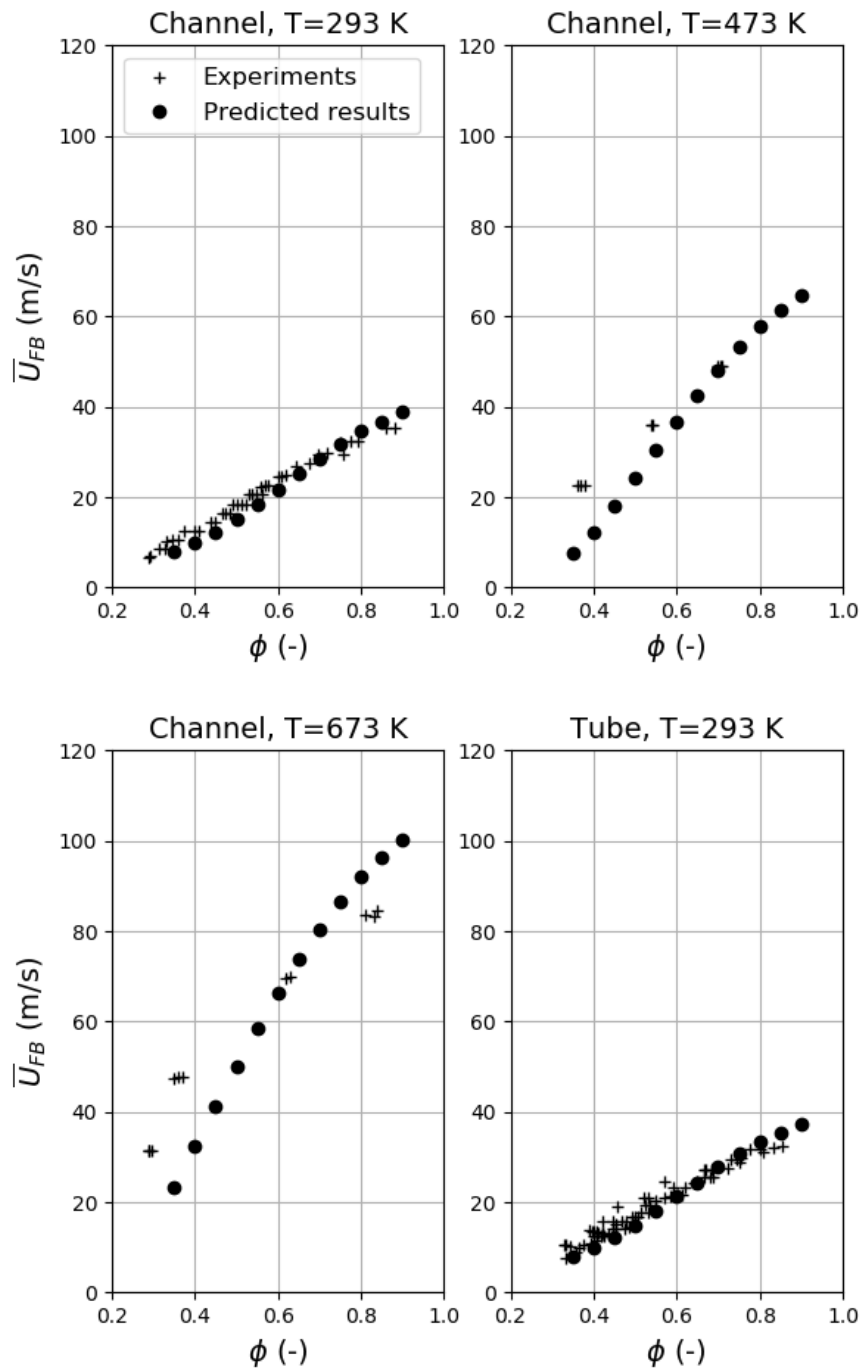


Figure 24: Comparing the results of the duplicated model to experimental data from Eichler [7].

### 3.2 Improvement Study 1: Turbulence-Flame Interaction

Detailed interaction between combustion and turbulence is a complex subject. One major overview is provided by Lipatnikov [44] in 2010. He concludes that the physics of the interac-

tion mechanisms are not yet fully understood and this holds especially for the case where the laminar flame speed and the turbulent fluctuations are of the same order. Also, DNS studies are yet too computational expensive to include both detailed combustion kinetics and high Reynolds number turbulence.

Four different types of turbulence-flame interaction can be defined: effect of turbulence on the flame and effect of the flame on turbulence upstream of the flame, in the reaction zone and downstream of the flame. The second interaction type is of importance: the effect of the flame on upstream turbulence. This is because the BLF model is based on upstream fluctuations. For the same reason the effect on downstream turbulence is disregarded. Of interest are also the first and third interactions, since they affect the turbulent burning velocity  $S_t$ .

### 3.2.1 Effect of the Flame on Upstream Turbulence

Measurements presented by Jainski [45] in 2018 show that turbulence upstream of a V-shaped flame is affected by the flame. The turbulent fluctuations, obtained by using PIV, are shown for both unreacted (no flame) and reacted flow (with flame) in Figures 25 and 26, respectively. The setup he uses is shown in Figure 27.

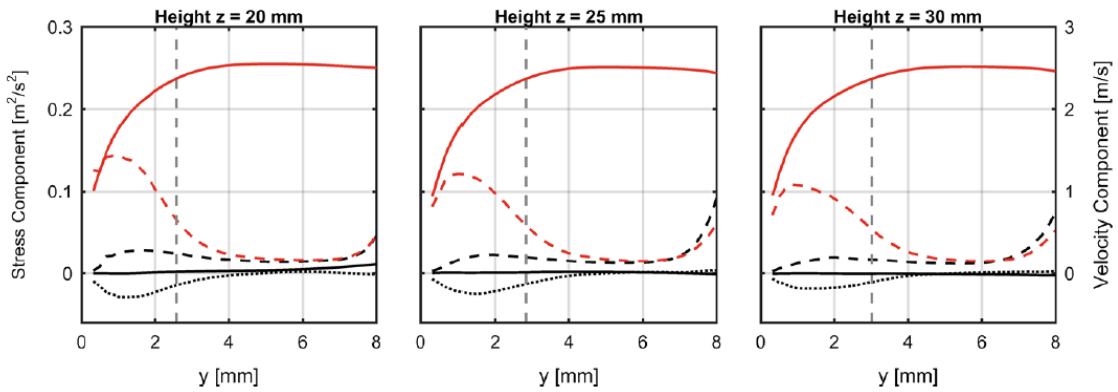


Figure 25: Turbulent fluctuations in the unreacted flow (from Jainski [45]).

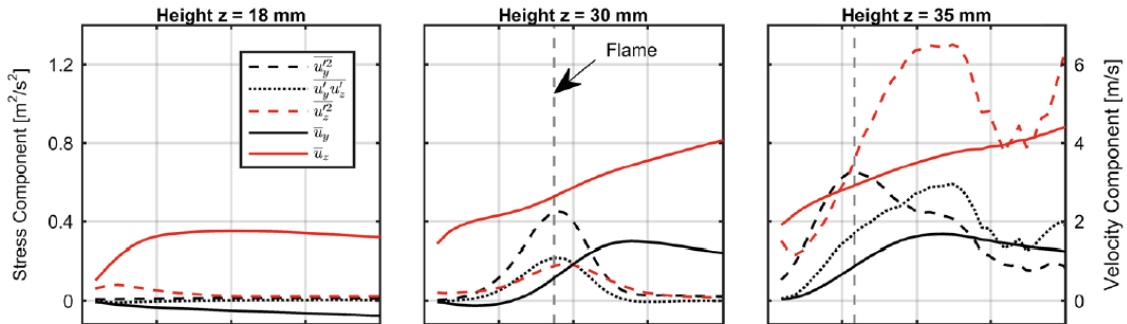


Figure 26: Turbulent fluctuations in the reacted flow (from Jainski [45]).

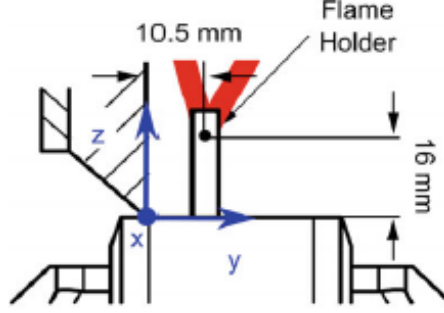


Figure 27: Jainiski's setup: a V-shaped flame approaching a wall on one side (from Jainiski [45]).

Of interest is the Reynolds stress in  $z$  direction  $\overline{u_z'^2}$ , the red dashed line, since this is the fluctuation parallel to the flow. The profiles for the unreacted and reacted flow differ in shape, but also the magnitude of the  $y$  axis changes. The graphs in Figure 26 include the location of the flame front, such that it can be concluded that the fluctuations upstream of the flame (left of the flame in the graphs) have increased.

In most burner configurations the flame front is in opposite direction of Jainiski's V-shaped flame. His fluctuation profiles can therefore not simply be copied for other burner configurations. However, the unreacted fluctuations, shown in Figure 25, can be compared to Hoferichter's fluctuations profile. This requires some additional steps, since a Reynolds stress  $\overline{u_z'^2}$  is compared to a normalized fluctuation  $\frac{u'}{u_\tau}$ . These equations calculate the shear velocity  $u_\tau$  by estimating the shear stress:

$$u_\tau = \sqrt{\frac{\tau_w}{\rho}} \quad (3.5)$$

$$\tau_w = 0.5 \cdot C_f \rho U^2 \quad (3.6)$$

$$C_f = 0.074 \cdot \text{Re}_l^{-0.2} \quad \text{for a flat plate, Jainiski's setup} \quad (3.7)$$

$$C_f = 0.079 \cdot \text{Re}_D^{-0.25} \quad \text{for a duct, Hoferichter's model} \quad (3.8)$$

Jainiski states that the fluctuations for the unreacted flow are in agreement with literature. This is based on comparison to direct simulations from Spalart [39]. Figure 28A shows the Reynolds stress  $\overline{u_z'^2}$  with a maximum value of 0.12, while the validation curve, shown in Figure 28C shows a peak value of 0.5. The results of Figure 28C are related to the normalized fluctuations in Figure 28D. Comparing the graph with the highest peak (which is in the direction of the flow) to the normalized fluctuations used by Hoferichter [21], Figure 28B, shows that the peak values are of the same order. Also the location of the peaks are similar. The main difference is a factor 4 between Jainiski's and Spalart's Reynolds stress. 9

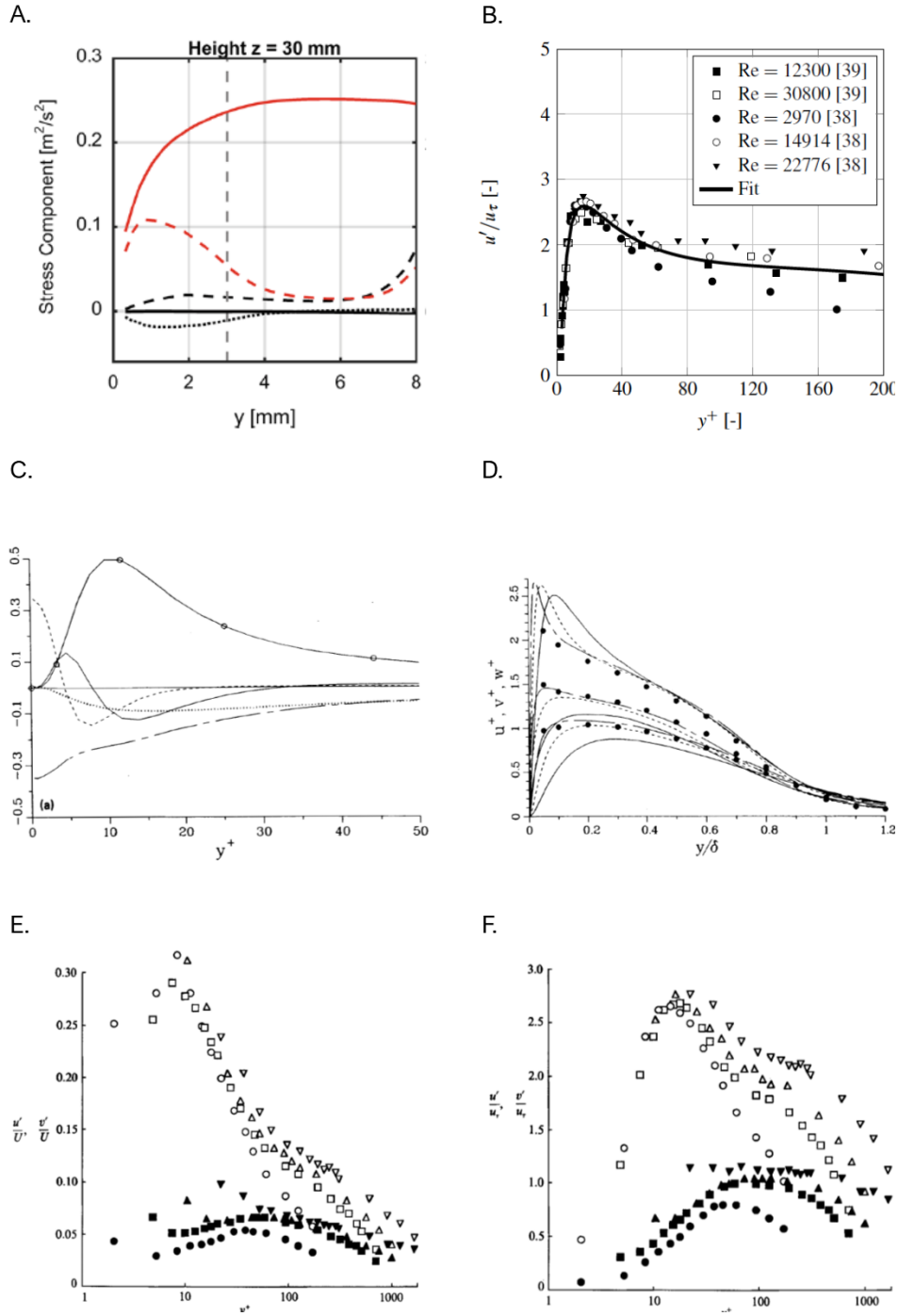


Figure 28: A: Turbulent fluctuations in unreacted flow (from Jainiski [45]). B: Normalized fluctuations as used in the BLF model (from Hoferichter [21]). C: Reynolds stress parallel to the flow (from Spalart [39]). D: Normalized fluctuations (from Spalart [39]). E and F: Turbulence intensities and normalized fluctuations for different  $Re$  from 3,000 to 40,000. Empty symbols correspond to fluctuations parallel to the flow (from Wei [46]).

Hoferichter's fluctuations graph is based on measurements from Wei [46]. The results are

shown in Figure 28E. Wei also included a graph of the turbulence intensity (Figure 28F), showing peak values of around 0.30. Jainki mentions that a turbulence intensity of around 6-7 % is established. Since this is approximately 4 times smaller than the peak value of 0.30 (= 30%), the difference in magnitude between Jainki's and Hoferichter's plots is explained.

Finally, for increasing values of  $y$  the fluctuations in Jainki's graph (Figure 28A) approached relatively lower values than the fluctuations in Hoferichter's graph (Figure 28B) do. However, in Wei's graph (Figure 28E) the fluctuations drop quite well for increasing  $y$ . The qualitative difference between Jainki's and Hoferichter's graph could just depend on the way Hoferichter selected data from Wei.

It is concluded that the fluctuations of Jainki's measurements of unreacted flow are similar to those used by Hoferichter. Also, the reacted flow shows clear differences in the fluctuations upstream of the flame. It is therefore worth trying to add this interaction to the BLF model, even with a different flame configuration.

### 3.2.2 Code Modification

The first modification is based on a different expression for  $S_t$ : Equation 2.25 is replaced by Lin's correlation, Equation 2.28. This correlation shows good agreement with experiments (a maximum error of 20%) and it includes the Lewis number, which is one the important parameters that characterises hydrogen combustion. For this modification the pre-exponential factor  $C$  disappears.

The second modification uses Jainki's fluctuations upstream of the flame. A polynomial fit has been made to mimic the  $\overline{u_z'^2}$  curve of the middle graph ( $z = 30\text{mm}$ ) of Figure 26. This fit was transformed to the notation of Hoferichter: the difference in turbulence intensity is accounted for (Jainki: 6-7 %, for Hoferichter: 30%) and  $\overline{u_z'^2}$  is converted to  $u'/u_\tau$ . Equation 3.9 shows the resulting polynomial fit. Together with Hoferichter's graph the fit is shown in Figure 29.

$$\begin{aligned} \frac{u'}{u_\tau} = & -1.561 \cdot 10^{-7} \cdot (y^+)^6 + 2.729 \cdot 10^{-6} \cdot (y^+)^5 - 1.722 \cdot 10^{-4} \cdot (y^+)^4 \\ & + 4.644 \cdot 10^{-3} \cdot (y^+)^3 - 4.854 \cdot 10^{-2} \cdot (y^+)^2 + 1.590 \cdot 10^{-1} \cdot y^+ + 1.974 \end{aligned} \quad (3.9)$$

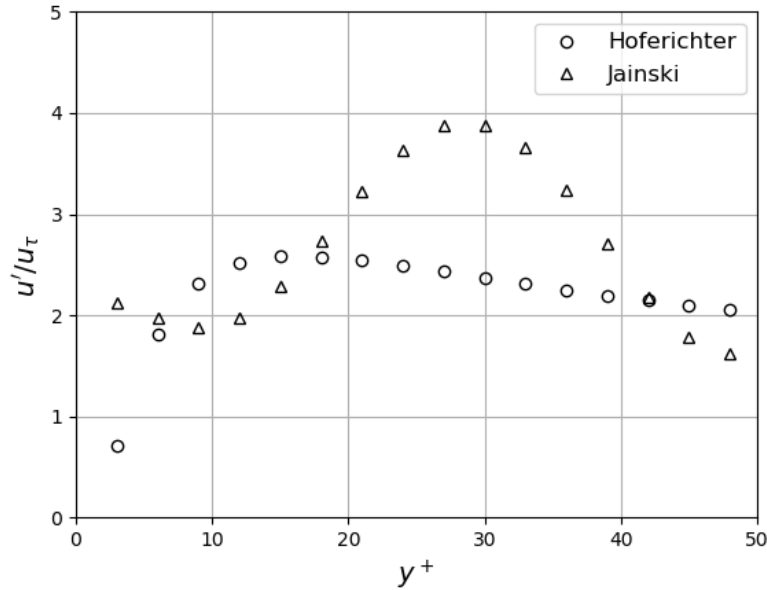


Figure 29: Jainski’s reacted flow fluctuations compared to Hoferichter’s in the near wall region  $y^+$  is 0 to 50 for  $u_\tau = 1$  m/s.

### 3.3 Improvement Study 2: Flame Instabilities

Two major difficulties in lean premixed hydrogen combustion are the hydrodynamic Darrieus Landau instability (DL instability) and the thermal-diffusive instability. Eichler [7] already mentions the importance of those instabilities, since they are responsible for the onset to a cellular flame structure. Also, based on DNS studies, Gruber [18] argues that BLF is initiated by instability mechanisms, including the DL instability.

Figure 30 illustrates the DL instability. A small perturbation causes the flame front locally to move upstream and the high burned temperature causes the upstream unburned flow to expand. Expanding results in divergence and thus a velocity decrease, which then enables the flame front to propagate upstream even more.

Figure 31 shows the thermal-diffusive instability. Poinot [32] explains that a perturbation in a flame with  $Le < 1$  will increase because heat is transferred (from the burned to the unburned mixture) faster than mass is transferred in opposite direction. The most upstream flame tip sucks fresh fuel faster than it diffuses heat, and therefore, locally, the fuel becomes more rich.

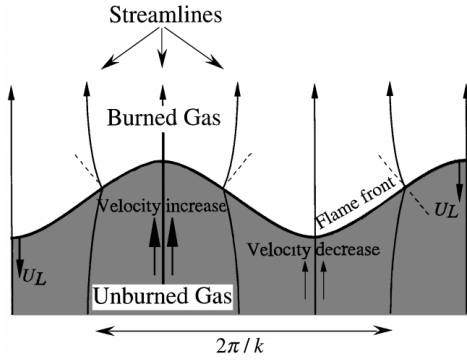


Figure 30: DL instability caused by expansion and contraction of the flow due to combustion (from Clanet [47]).

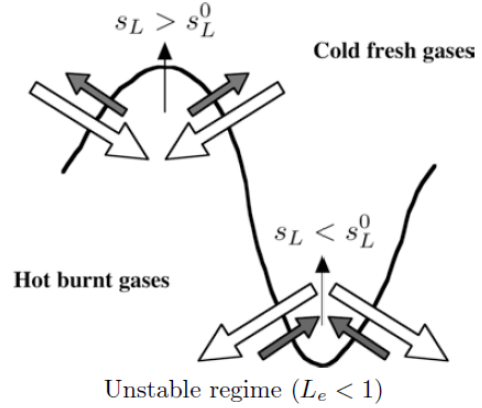


Figure 31: Instability caused by a Lewis number lower than 1 (from Poinsot [32]).

Okafor [48] observed that instability in lean flames is either due to thermal-diffusive effects or hydrodynamic instability. The former plays a predominant role for  $Le < 1$ , while for higher Lewis numbers the hydrodynamic instability is dominant. Still, these two instabilities interact and cannot simply be separated. The main parameters involved are the Markstein Length and the Lewis number.

Lean hydrogen-air mixtures are one of the few fuels with a negative Markstein length and therefore flame stretch needs to be taken into account. According to Troiani [49], who performed experiments on DL instability effects in turbulent premixed flames, a critical disturbance wave length can be defined that depends on  $L_M$ :

$$\lambda_{w,c} = 2 \cdot \pi (3 \cdot \sigma - 1) \frac{L_M}{\sigma - 1} \quad (3.10)$$

This equation includes the expansion ratio  $\sigma$  and defines the lower limit of an unstable domain:  $\lambda_{w,c} < \lambda_w < h$ . It means that for all wavelengths  $\lambda_w$  higher than  $\lambda_{w,c}$ , DL instability occurs. The upper limit is simply the tube diameter or channel height. This equation shows that a negative value of  $L_M$  always results in DL instability.

### 3.3.1 Onset to a Cellular Flame Structure

Following the definition of Gelfand [50]: a cellular flame is a flame with a curved surface, which is caused by instability of the combustion process. This is the result of expansion and heat-mass transfer diffusion processes. A cellular flame structure consists of a number of cellular flames. Two examples are shown in Figures 32 and 33.



Figure 32: Picture of a real flame with a cellular structure (from [www1.gifu-u.ac.jp](http://www1.gifu-u.ac.jp)).

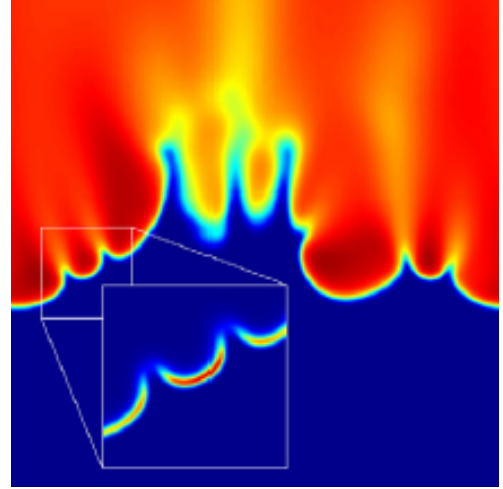


Figure 33: DNS results with cellular flames (from Aspden [51]).

Not all cellular flame structures are as clearly visible as in Figure 32. Hertzberg [52] estimates the cell diameter based on a local balance over the flame front:

$$d_{cell} \approx \frac{\alpha^2 \sigma}{(D_i - D_j) \frac{\partial S_t}{\partial C_i}} \quad (3.11)$$

This relation depends on the difference in molecular diffusivities  $D$  (from the fuel and oxidizer), the burning velocity  $S_t$ , the concentration of the most diffusive component  $C_i$ , the mixture averaged thermal diffusivity  $\alpha$  and the expansion ratio  $\sigma$ . This relation has been verified with experimental data. Cell sizes are typically in the order of millimeters. For leaner fuels the cell sizes decrease and also the cells might be further away from each other (in contrast to Figure 32, where the cells are close to each other) and this makes it harder to detect them.

Hertzberg [52] relates the onset to a cellular structure to the derivative of the burning velocity w.r.t. the concentration of the most diffusive component:  $\frac{\partial S_t}{\partial C_i}$ . He states that cellular structures are formed (and are stable) only when  $\frac{\partial S_t}{\partial C_i} > 0$ . This means that, if in a non-cellular flame structure, locally the concentration of the most diffusive component increases (due to a fluctuation), the burning velocity also increases. This accelerates until a cellular flame structure is formed.

For lean mixtures the burning velocity increases if the mixture becomes richer  $\frac{\partial S_t}{\partial \phi} > 0$ , while for rich mixtures the burning velocity increases if the mixture becomes leaner  $\frac{\partial S_t}{\partial \phi} < 0$ . The highest burning velocity is found at the stoichiometric ratio ( $\phi = 1$ ). Figure 34 shows that for a hydrogen-air mixture the most diffusive component is hydrogen. Increasing the concentration of this component is similar to an increase in the equivalence ratio  $\phi$ , and thus  $\frac{\partial S_t}{\partial \phi} > 0$  has a similar effect as  $\frac{\partial S_t}{\partial C_i} > 0$ : lean hydrogen-air mixtures form a cellular flame structure.

Of interest are also other fuels, since for most fuels the most diffusive component is oxygen. The opposite happens now: when the oxygen concentration increases, the equivalence ratio decreases. A rich mixture is subject to the formation of a cellular structure. This is of importance if the BLF model is validated using fuels other than pure hydrogen, while the effect of flame structure needs to be taken into account.

Substance	Symbol	Diffusivity (cm <sup>2</sup> /sec)
Flame gases (average effective value)	$\alpha$	0.55
Oxygen	$D_{O_2}$	0.43
Methane	$D_{CH_4}$	0.47
Ethane	$D_{C_2H_6}$	0.30
Propane	$D_{C_3H_8}$	0.25
Butane	$D_{C_4H_{10}}$	0.22
Hexane	$D_{C_6H_{14}}$	0.18
Heptane	$D_{C_7H_{16}}$	0.17
Octane	$D_{C_8H_{18}}$	0.16
Decane	$D_{C_{10}H_{22}}$	0.15
$C_nH_{2n+2}$ ( $n \rightarrow \infty$ )	$D_{M \rightarrow \infty}$	0
Hydrogen	$D_{H_2}$	1.86
Deuterium	$D_{D_2}$	1.32

Figure 34: Diffusivities for different substances showing the high diffusivity for hydrogen (from Hertzberg [52]).

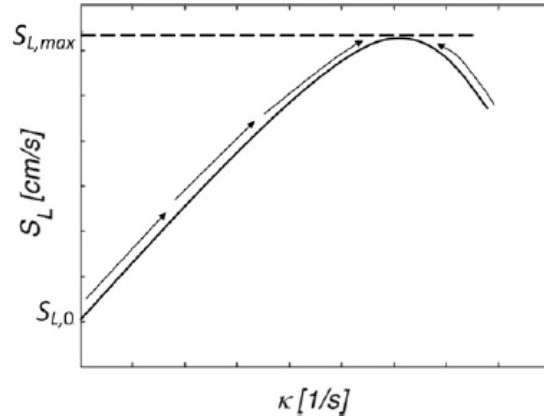


Figure 35: The laminar burning velocity: an attractor for thermal-diffusively unstable flames (from Venkateswaran [53]).

Venkateswaran [53, 54] shows that the laminar burning velocity for unstable flames (with a negative Markstein length) grows towards a stable attractor. This concept is illustrated in Figure 35. Although he does not mention transition to a cellular flame structure, he does analyse an unstable, negative Markstein length flame. This indicates that once the transition to a cellular flame structure has taken place, the flame structure is stable again. Venkateswaran states that this theory is only applicable to flames that are thermal-diffusively unstable.

Based on the observations of Hertzberg and Venkaterwaran the following is concluded: for thermal-diffusively unstable flames a cellular flame structure is formed, due to an increase in the burning velocity. The cellular structure itself is stable.

### 3.3.2 Effect of Flame Instabilities on Burning Velocity

This paragraph provides an overview of the effect of instabilities on the burning velocity. Zaytsev [55] studied the effect of the DL instability on turbulent flame velocity, numerically. For different expansion ratios, the normalized turbulent burning velocity is plotted against the normalized turbulent fluctuations, shown in Figure 36. The full lines show a model with the DL instability included, the dashed lines without. This model is validated for moderate Reynolds numbers.

Kadowaki [56] performed a numerical study on the flame velocity of cellular structured flames at low Lewis numbers ( $Le < 1$ ). He concludes that the local flame velocity increases at a convex flame (w.r.t. the unburned mixture) and decreases at a concave flame. This is in agreement

with the DL instability. Also, Kadowaki states that, due to the Arrhenius nonlinearity the velocity increase in the convex flame front is larger than the velocity decrease at a concave flame front. He presented a graph for the burning velocity against the Lewis number, which is shown in Figure 37.

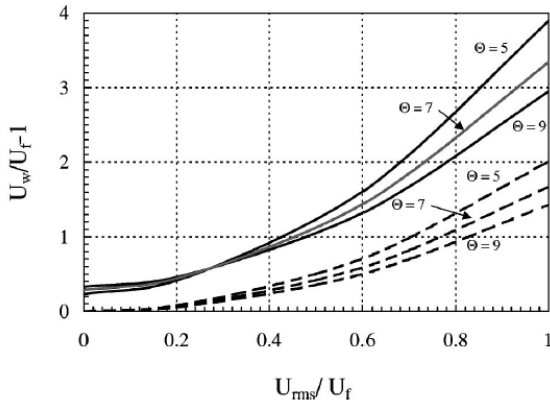


Figure 36: Turbulent burning velocity against turbulent fluctuations, both normalized, for different expansion ratios (from Zaytsev [55]).

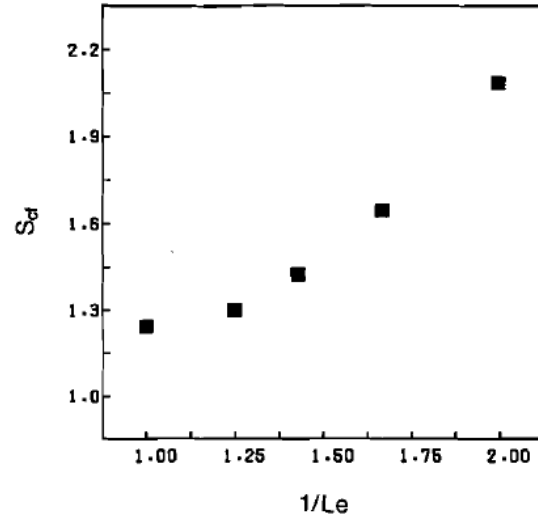


Figure 37: Relation between the turbulent burning velocity (divided by flame surface area) and Lewis number for cellular structured flames (from Kadowaki [56]).

Aspden [51] studied the characterization of low Lewis number flames, numerically. For lean premixed hydrogen ( $\phi < 0.5$ ) and low Lewis numbers ( $Le < 0.4$ ) his results show local maximum burning velocities that are four times higher than the laminar burning velocity. This occurs at the presence of cellular flames.

Aspden also notes that the Karlovitz number  $Ka$  and the Damköhler number  $Da$  for low Lewis number flames should be calculated with the freely propagating properties instead of the laminar properties. Only then the diagram shown in Figure 11 can be used accurately. This is based on the observation of different behaviour of flames for different equivalence ratios, while the Karlovitz, Damköhler and Lewis number were constant. For lean cases ( $\phi < 0.4$ ) the corrected Karlovitz number is 5.2 times smaller than the laminar one.

Finally, in a numerical study of unstable hydrogen/air flames, Frouzakis [57] proposes an increase of 22-24% from the laminar to turbulent burning velocity. This holds for an equivalence ratio between 0.75 and 1. For lower equivalence ratios (0.5 to 0.75) he proposes a ratio of the turbulent to laminar burning velocity of 1.65.

To conclude with: the effect of instabilities and onset to a cellular flame structure on the burning velocity has been studied by several researchers. Although different theories are provided, one common result is an increase in burning velocity, which is related to flame instability and flame structure.

### 3.3.3 Code Modification

The occurrence of flame instability (and cellular flame formation) is commonly attributed to a Lewis number below 1. Also, the burning velocity knows many different expressions and is therefore one of the uncertain variables in the BLF model. For this reason the correlation from Kadowaki is added to the code: it relates the Lewis number directly to the burning velocity. A polynomial fit through the data of Figure 37 is given by Equation 3.12. In the code a multiplication factor is used for  $S_t$ , and therefore Equation 3.12 is normalized by the value of  $S_{cf}$  at  $Le = 1$ . This results in Equation 3.13. Note that in 37 Kadowaki uses a different symbol for the burning velocity.

$$S_{cf} = 0.7516 \cdot \left(\frac{1}{Le}\right)^2 - 1.405 \cdot \left(\frac{1}{Le}\right) + 1.8906 \quad (3.12)$$

$$\frac{S_{t:cf}}{S_t} = 0.6052 \cdot \left(\frac{1}{Le}\right)^2 - 1.1314 \cdot \left(\frac{1}{Le}\right) + 1.5224 \quad (3.13)$$

Equation 3.13 is based on data up to  $1/Le = 2$ , so this relation should only be used in the range of  $Le$  is 0.5 to 1. Above 1 the relation does not make sense, since cellular flames are not present there. Below a Lewis number of 0.5 the graph can either continue with the same quadratic trend or the increase stagnates. Based on findings from Hertzberg and Venkateswaran, it is assumed that stagnation occurs due to the self-stabilization of a cellular flame. For Lewis numbers below 0.5 the multiplication factor at  $Le = 0.5$  is used.

From now on Equation 3.13 will be referred to as the Lewis number correction. Two modifications are examined: the first uses the Lewis number correction for all temperatures, the second for elevated temperatures only. The reason for this is that the prediction of the Markstein length for elevated temperatures is very uncertain and has never been validated.

## 3.4 Improvement Study 3: Flame Stretch

In Paragraph 2.2.3 the flame stretch rate was discussed. This section shows the changes in  $\kappa_{mean}$  and  $\kappa_t$  when turbulence cannot be assumed isotropic. First  $\kappa_{mean}$  is discussed and for convenience the expression is shown again (Equation 3.14).

$$\begin{aligned} &= \left( \frac{\partial \bar{u}}{\partial x} + \frac{\partial \bar{v}}{\partial y} + \frac{\partial \bar{w}}{\partial z} \right) - \frac{1}{2 \cdot k} \left[ \overline{u'u'} \frac{\partial \bar{u}}{\partial x} + \overline{u'v'} \frac{\partial \bar{u}}{\partial y} + \overline{u'w'} \frac{\partial \bar{u}}{\partial z} \right. \\ &\quad \left. + \overline{v'u'} \frac{\partial \bar{v}}{\partial x} + \overline{v'v'} \frac{\partial \bar{v}}{\partial y} + \overline{v'w'} \frac{\partial \bar{v}}{\partial z} + \overline{w'u'} \frac{\partial \bar{w}}{\partial x} + \overline{w'v'} \frac{\partial \bar{w}}{\partial y} + \overline{w'w'} \frac{\partial \bar{w}}{\partial z} \right] \end{aligned} \quad (3.14)$$

The velocity components for fully developed flow have partial derivatives w.r.t.  $x$  equal to zero. Since Hoferichter's model works in the 2D xy-plane, and side wall ( $z = 0, z = w$ ) effects are avoided, it is valid to take the xy-plane at  $z = w/2$ , which is in the middle of the

channel width. Symmetry then allows to cross out all partial derivatives w.r.t. to  $z$  and also everything that includes the time averaged velocity component  $\bar{w}$ . What is left then are 3 terms:

$$\kappa_{mean} = \frac{\partial \bar{v}}{\partial y} - \frac{1}{2 \cdot k} \left[ \overline{u'v'} \frac{\partial \bar{u}}{\partial y} + \overline{v'v'} \frac{\partial \bar{v}}{\partial y} \right] \quad (3.15)$$

With  $\frac{\partial \bar{u}}{\partial x}$  and  $\frac{\partial \bar{w}}{\partial z}$  being zero and by assuming incompressible flow (which is valid for the velocities of interest), continuity results in  $\frac{\partial \bar{v}}{\partial y} = 0$ . This simplifies Equation 3.15 to Equation 3.16:

$$\kappa_{mean} = -\frac{\overline{u'v'}}{2 \cdot k} \frac{\partial \bar{u}}{\partial y} \quad (3.16)$$

Also, the  $k$  in Equation 2.37, that is used to determine  $\kappa_t$ , should now be replaced by Equation 3.18, resulting in Equation 3.19. Note that a similar modification is made to  $\varepsilon$ .

$$\kappa_t = \Gamma_K \frac{\varepsilon}{k} \quad (3.17)$$

$$k = \frac{1}{2} \cdot \left( \overline{(u')^2} + \overline{(v')^2} + \overline{(w')^2} \right) \quad (3.18)$$

$$\kappa_t = 2 \cdot \Gamma_K \frac{\overline{u'v'w'}}{\Lambda \left( \overline{(u')^2} + \overline{(v')^2} + \overline{(w')^2} \right)} \quad (3.19)$$

### 3.4.1 Code Modification

To evaluate Equation 3.16 all components of the r.h.s. need to be determined. First  $\overline{u'v'}$  is related to  $\overline{u'} \overline{v'}$  by using the correlation coefficient  $K$ , which is defined by Equation 3.20. In 1951 Laufer [58] performed measurements on turbulence in fully developed channel flow and he also measured and plotted  $K$  for three different Reynolds numbers. This plot is shown in Figure 38.

$$K = \frac{\overline{u'v'}}{\sqrt{\overline{(u')^2}} \sqrt{\overline{(v')^2}}} \quad \text{with: } \overline{u'v'} = K \overline{u'} \overline{v'} \quad (3.20)$$

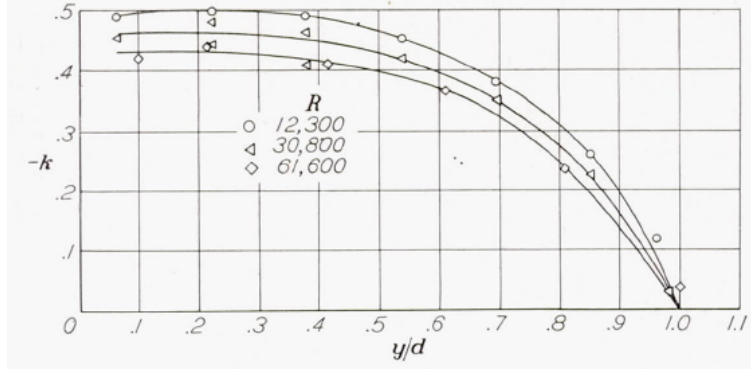


Figure 38: Experimentally obtained correlation coefficient  $K$  (in the figure  $k$ ) against the ratio of the distance from the wall  $y$  and half the channel height  $d$ , for fully developed channel flow (from Laufer [58]).

Since the BLF model focuses on the near-wall region, only the left asymptotic values of Figure 38 are of relevance, which are independent of  $y$  (the plots are approximately horizontal close to the wall). For  $\text{Re} = 12300, 30800, 61600$ ,  $-K = 0.5, 0.46, 0.43$ , respectively. To get Reynolds numbers in between a simple fit function is used, which is given by Equation 3.21.

$$-K = -0.10 \cdot \log_{10}(\text{Re}) + 0.91 \quad (3.21)$$

The second component of Equation 3.16 that needs to be defined is the (anisotropic) turbulence kinetic energy  $k$ . The definition given by Equation 3.18 is used. For the  $u'$  fluctuations Hoferichter used Equation 2.72. A polynomial fit for  $v'$  is made, in the range of  $y^+$  is 0 to 50, by using data from Wei [46], which is shown in Figure 28F. Finally, based on Figure 28D the  $w'$  fluctuations are estimated at 1.4 times  $v'$  in the region close to the wall. The corresponding equations are given by Equations 3.22 to 3.24 and plotted in Figure 39.

$$\begin{aligned} \frac{u'}{u_\tau} &= 2.661 - 7.211 \cdot \ln(y^+) + 7.600 \cdot \ln(y^+)^2 - 2.900 \cdot \ln(y^+)^3 \\ &\quad + 0.472 \cdot \ln(y^+)^4 - 0.028 \cdot \ln(y^+)^5 \end{aligned} \quad (3.22)$$

$$\frac{v'}{u_\tau} = -0.00052 \cdot (y^+)^2 + 0.045873 \cdot y^+ - 0.014410 \quad (3.23)$$

$$\frac{w'}{u_\tau} = -0.000728 \cdot (y^+)^2 + 0.064222 \cdot y^+ - 0.020174 \quad (3.24)$$

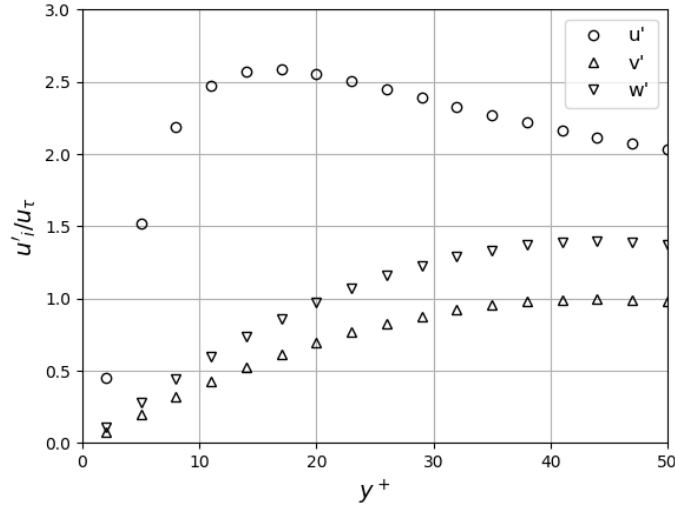


Figure 39: Normalized fluctuations in the near wall region  $y^+$  is 0 to 50 for  $u_\tau = 1$  m/s.

The last component of Equation 3.16 is the mean velocity derivative w.r.t.  $y$ . The  $\bar{u}$  profile can be approximated with Equation 3.25, which is commonly used to estimate the fully developed turbulent velocity profile. This function depends on the centerline velocity  $U_{FB}$  and is valid from the wall ( $y = 0$ ) to the channel half height  $h/2$ . Taking the derivative w.r.t  $y$  results in 3.26. Substituting all the components into Equation 3.16, and removing the bars for convenience, results in Equation 3.27.

$$u = U_{FB} \left( \frac{y}{h/2} \right)^{1/7} \quad (3.25)$$

$$\frac{\partial u}{\partial y} = \frac{2}{7 \cdot h} \cdot U_{FB} \left( \frac{y}{h/2} \right)^{-6/7} \quad (3.26)$$

$$\kappa_{mean} = \frac{(-0.1 \cdot \log_{10}(\text{Re}) + 0.91) u'v'}{(u')^2 + (v')^2 + (w')^2} \cdot \frac{2}{7 \cdot h} \cdot U_{FB} \left( \frac{y}{h/2} \right)^{-6/7} \quad (3.27)$$

Together with Equations 3.23 and 3.24, the last expression will be used to account for the effect of anisotropic turbulence of the flame stretch rate. Also,  $\kappa_t$  is now determined by 3.19. Together the new expressions for  $\kappa_{mean}$  and  $\kappa_t$  form the modification.

However, the model was executed and a numerical convergence problem occurred. Equation 2.74 needs to be solved numerically for  $u_\tau$  and with both the  $\kappa_{mean}$  and  $\kappa_t$  being modified, the value of  $u_\tau$  diverges and the model crashes. Several initial guesses were tried, as well as larger residual errors and different numerical solvers. However, the model is highly non-linear and it is non-trivial to detect the relation between the modifications and the numerical divergence. For this reason  $\kappa_{mean}$  and  $\kappa_t$  have been modified separately and this shows that the modified  $\kappa_{mean}$  results into the numerical divergence. For this reason only the  $\kappa_t$  modification is used.

### 3.5 Results and Discussion

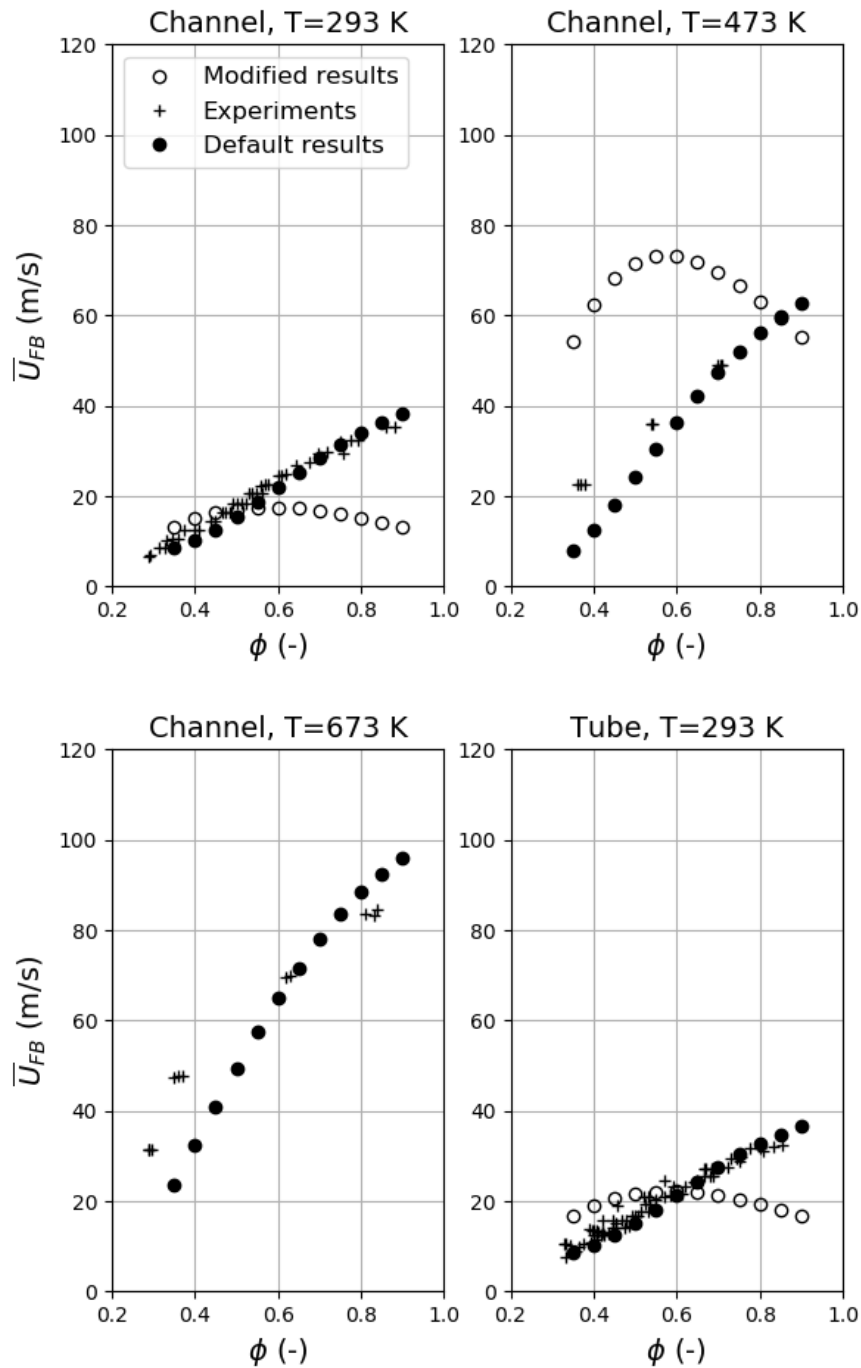


Figure 40: Model with Lin's correlation for  $S_t$ , with the modified results for  $T = 673$  K being too large to show up.

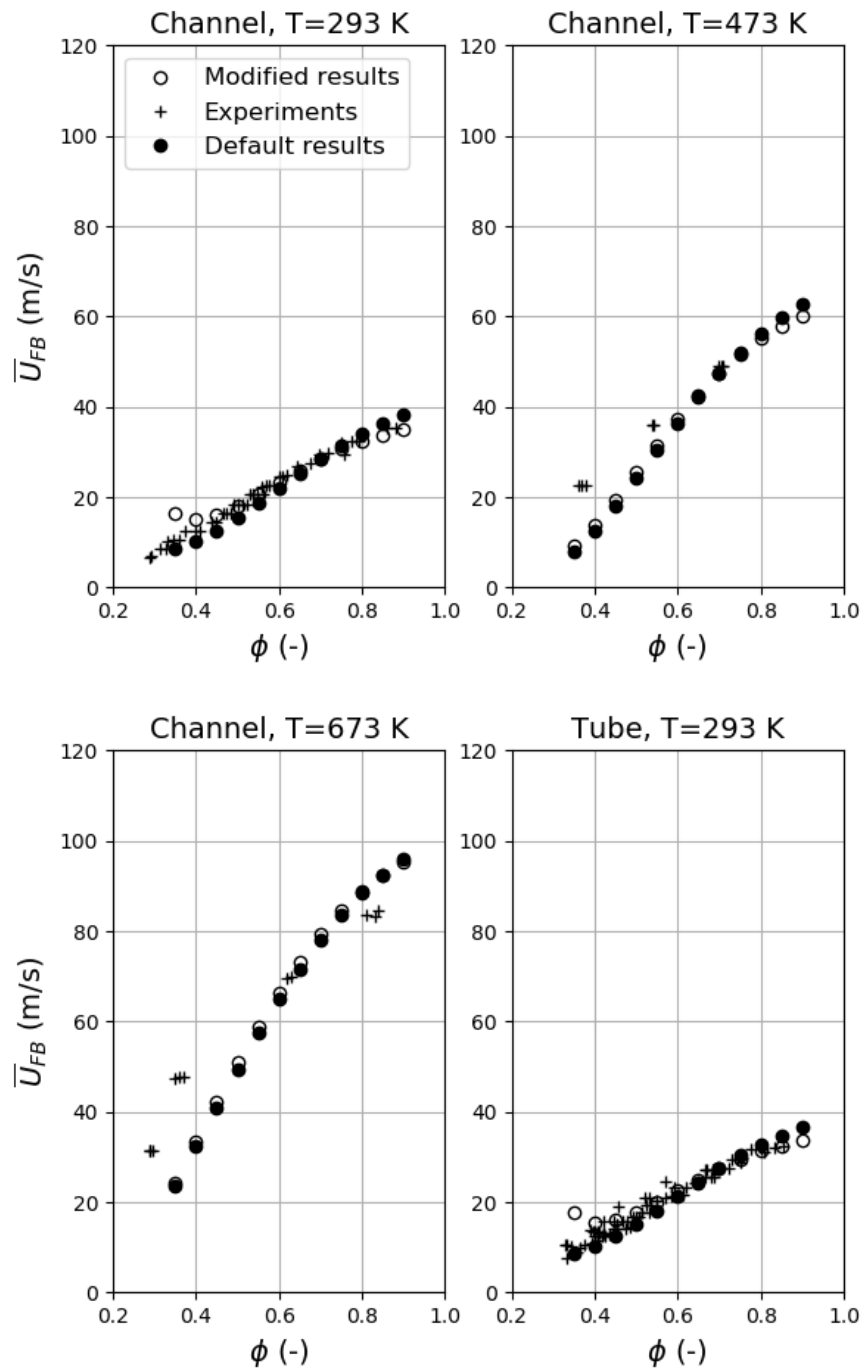


Figure 41: Model with Jainki's fluctuations graph for reacted flow, with  $C = 1.9$ .

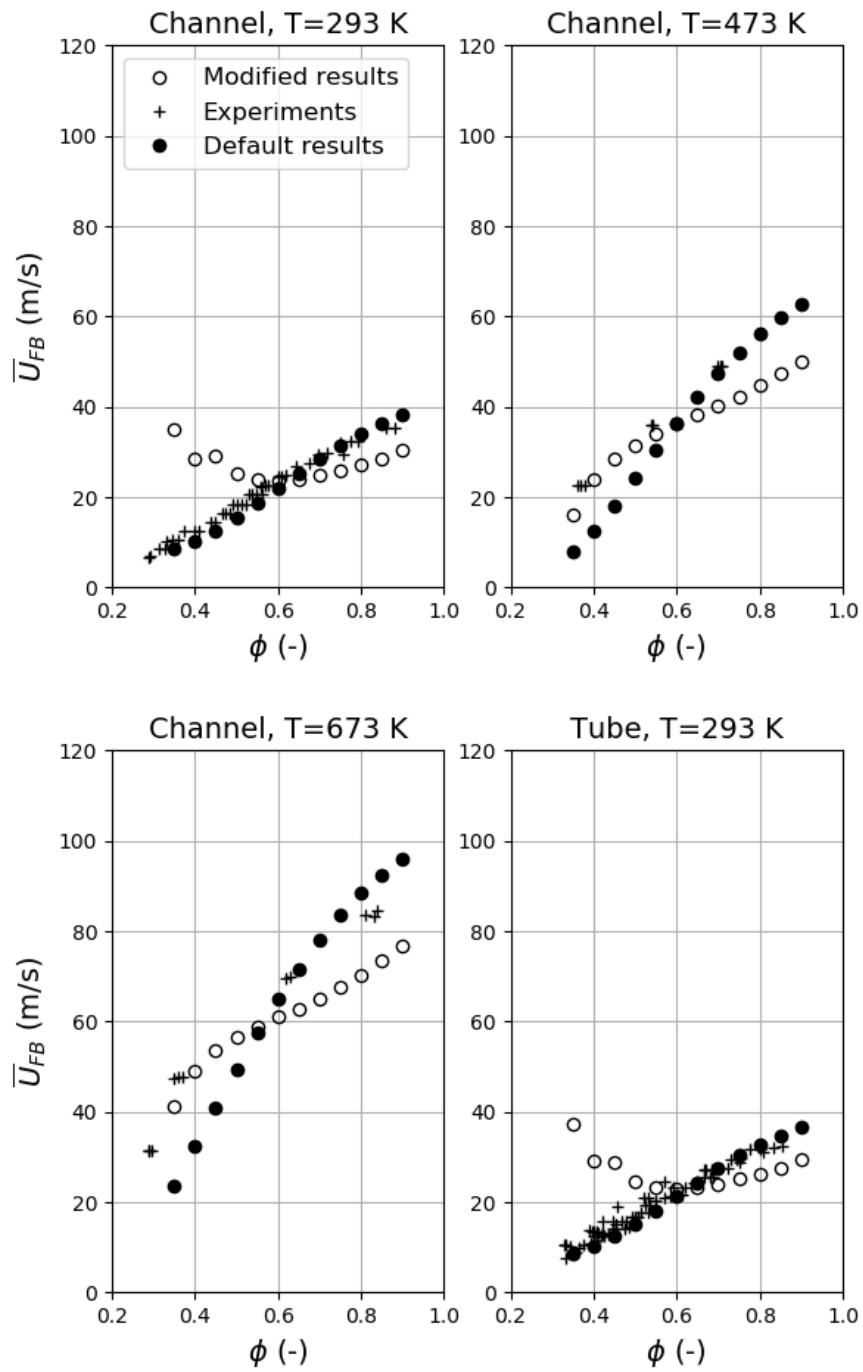


Figure 42: Model with Lewis number correction for all temperatures, with  $C = 2.0$ .

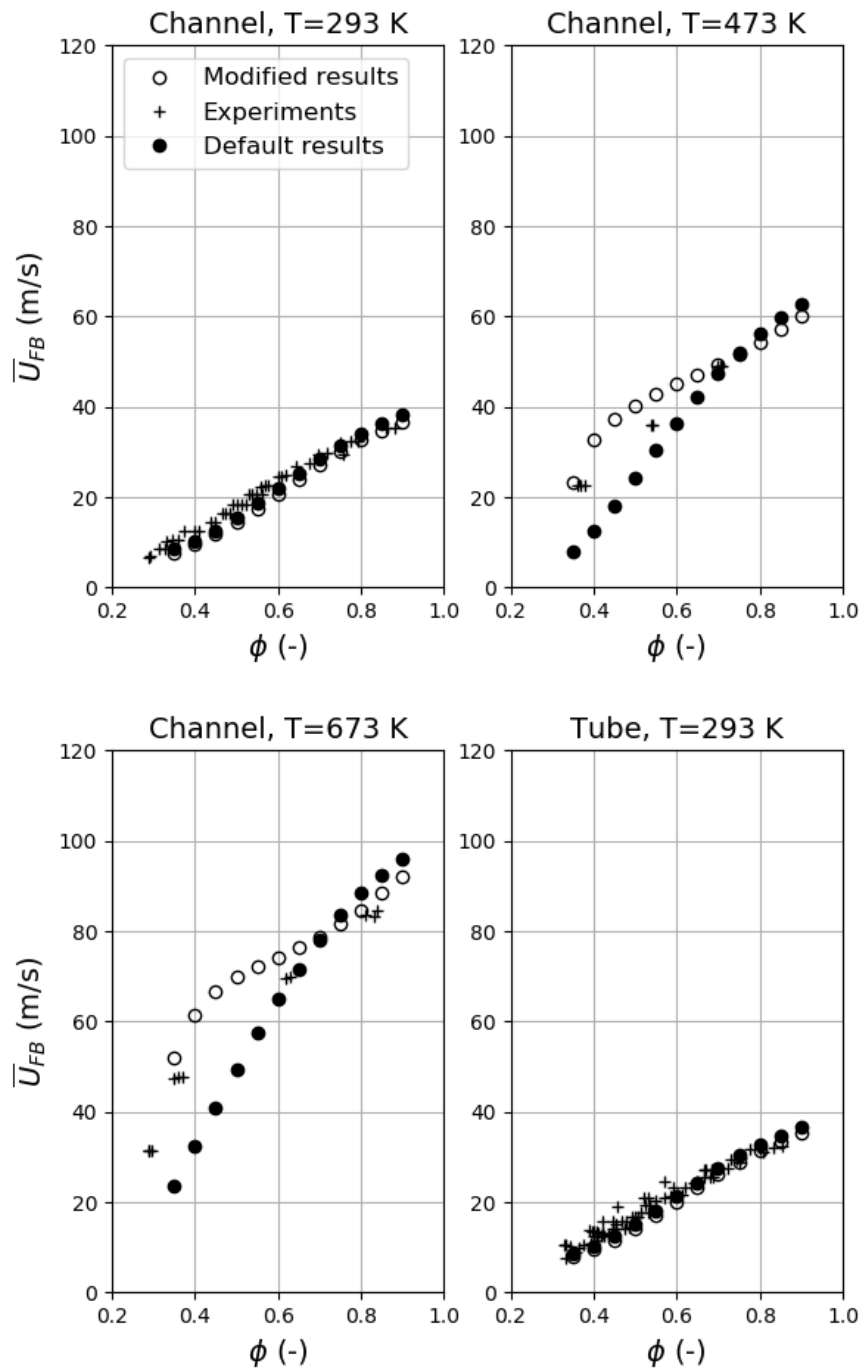


Figure 43: Model with Lewis number correction for elevated temperatures only, with  $C = 2.4$ .

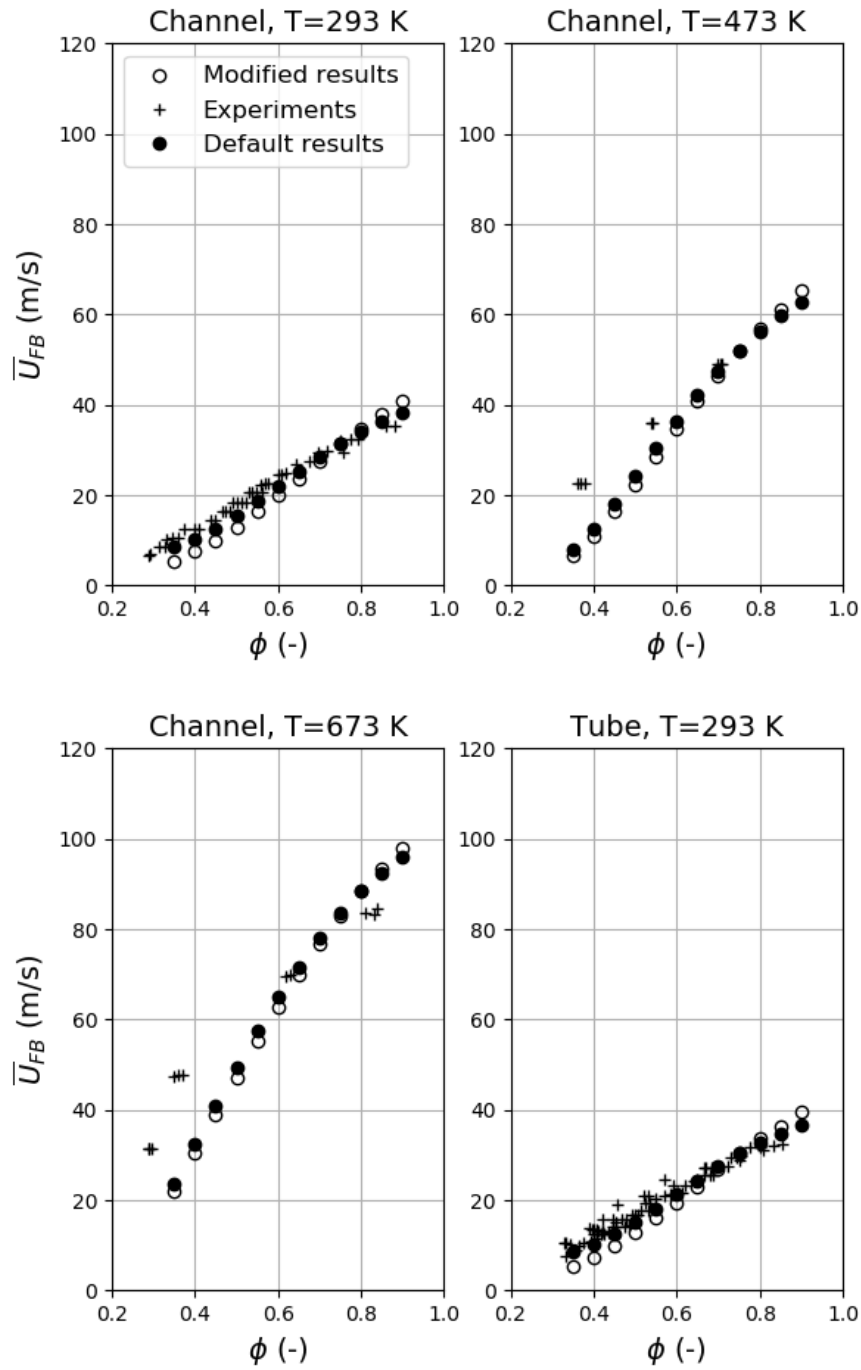


Figure 44: Model with anisotropic flame stretch included in  $\kappa_t$ , with  $C = 2.4$ .

According to Figure 40 Lin's correlation does not improve the model. Negative parabolic results show up and this can be explained by looking at Equation 3.28. The pressure term can be neglected (pressures are constant). With the Lewis number increasing with the equivalence ratio (Figure 22), the  $Le_{eff}^{-0.82}$  term results in a decreasing  $S_t$ . This explains the decrease in

flashback limit for higher  $\phi$ 's. The increase can be explained by the dominant effect of  $u'$  w.r.t.  $S_{l,0}$  for lower  $\phi$ 's: the flame is classified as *thin reaction zone*, while for higher  $\phi$ 's this is a *corrugated flame*. Figure 11 shows that for the *thin reaction zone* the fluctuations are more dominant.

$$\frac{S_t}{S_{l,0}} = 10.5 \cdot \text{Le}_{eff}^{-0.82} \left( \frac{u'}{S_{l,0}} \right)^{0.45} \left( \frac{\Lambda}{\delta_f} \right)^{-0.41} \left( \frac{P_0}{P} \right)^{0.75} \left( \frac{T_0}{T} \right)^{-1.33} \quad (3.28)$$

While Lin's correlation relates  $S_t$  directly to  $S_{l,0}$ , Hoferichter uses more equations to model the flame stretch and the corresponding burning velocity  $S_{l,s}$ . Although Hoferichter uses a simpler expression for  $S_t$ , Lin's correlation simplifies the modelling of flame stretch and could therefore give the inaccurate results.

Figure 41 shows that Jainiski's fluctuations do not affect the results much. However, the pre-exponential factor  $C$  drops from 2.3 to 1.9. This means that  $C$  has corrected for an overall overprediction. With Jainiski's fluctuations being larger than Hoferichter's, the overprediction can be explained. Still there are two tail-like trends at the left of the 293 K graphs. An explanation can be given by the difference in Markstein length's between the different inlet temperatures, shown by Figure 45. At 293 K the Markstein length is much larger and this results in a higher response to the flame stretch rate, following Equation 2.29. The flame stretch rate increases with turbulence by means of  $\kappa_t$ .

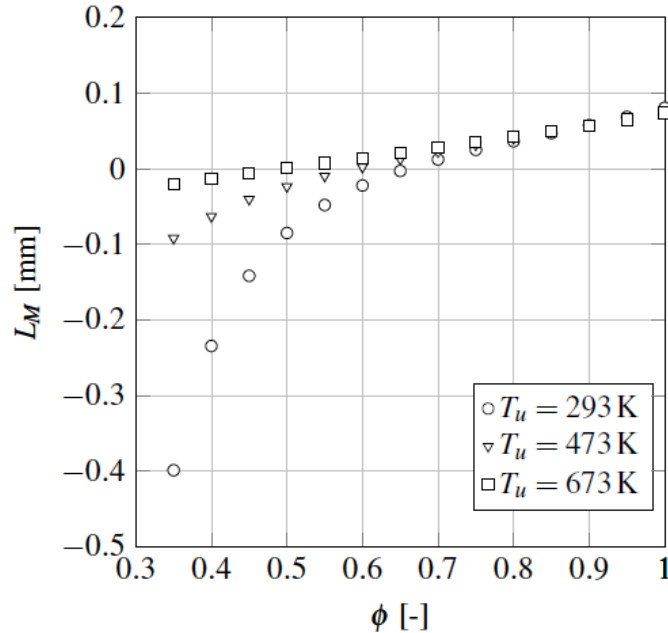


Figure 45: Markstein length for hydrogen-air mixtures at three temperatures (from Hoferichter [21]).

Figure 42 includes the results of the Lewis number correction for all temperatures. For elevated temperatures and low  $\phi$ 's the experiments are predicted really well. Also the trends

of the predictions agree more to the trend of the experiments (a steep slope for low  $\phi$ 's that reduces when  $\phi$  increases). However, for 293 K the model predicts poorly. The Lewis numbers for different temperatures are comparable to each other, which excludes that the large differences in accuracy is caused by the Lewis number correction. With only the Lewis number correction for elevated temperatures the model shows a higher overall accuracy. This is shown in Figure 43. Compared to Figure 42 the elevated temperatures are overpredicting. This is caused by a higher value for  $C$ , since  $C$  does not have to correct for the overprediction at 293 K anymore.

Finally Figure 44 shows the results of the anisotropic  $\kappa_t$  modification. Compared to the original BLF model the modified model underpredicts for low  $\phi$ 's and overpredicts for high  $\phi$ 's. The latter can be explained by an increase of  $C$  from 2.3 to 2.4. This means that the modification mainly affects the low equivalence ratios by underpredicting. As explained before, at 293 K the Markstein length is much larger and this results in a higher response to the flame stretch rate, following Equation 2.29. The flame stretch rate decreases now that both  $\varepsilon$  and  $k$  are determined with  $u'$ ,  $v'$  and  $w'$  instead of  $u'$  only (which is higher).

Based on these five modifications a final modification is proposed. While Jainski's fluctuations are based on a different flame shape and Lin's correlation simplifies the modelling of flame stretch, both the Lewis number correction and the anisotropic  $\kappa_t$  can be supported by theory. Therefore the final modification combines these two. The Lewis number correction is applied for all temperatures. The overprediction for 293 K and low  $\phi$ 's now is balanced out by the underprediction due to the anisotropic  $\kappa_t$  modification. The results are shown in Figure 46, and they show good agreement with the experiments.

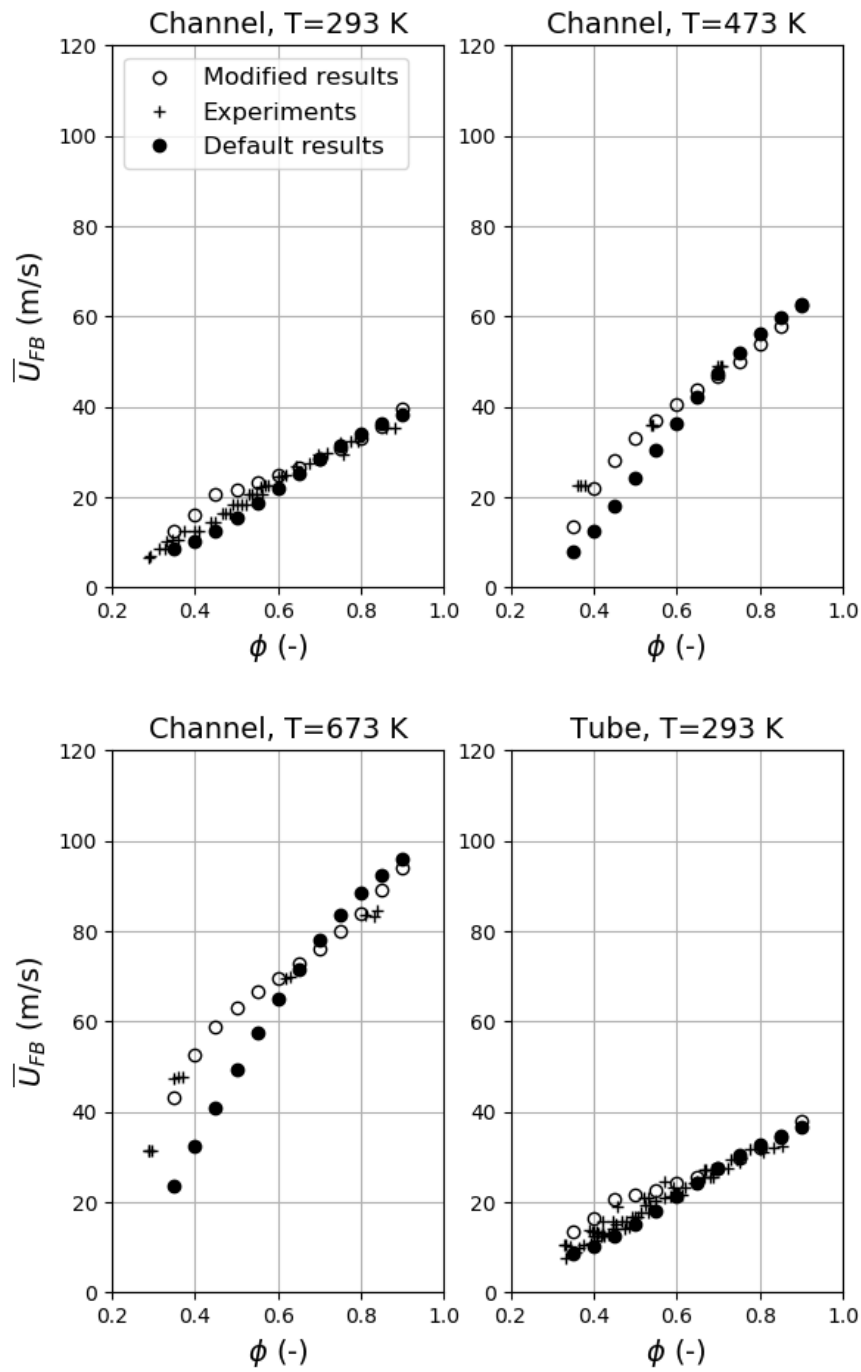


Figure 46: Combined modifications: Lewis number correction for all temperatures and anisotropic flame stretch included in  $\kappa_t$ , with  $C = 2.0$ .

### 3.6 Conclusion

To improve the original BLF model, three physical phenomena have been studied in detail. Starting with the turbulence-flame interaction, the effect of the flame on upstream turbulence was discussed. Jainski performed experiments showing that turbulence upstream of a flame can be affected significantly. Two modifications were proposed: Lin's correlation for  $S_t$  and the fluctuations from Jainski's experiments.

The second study was on flame instabilities. Both hydrodynamic DL instability and thermal-diffusive instability may lead to unstable flame fronts. This leads to the formation of cellular flames (which are stable itself), that have an increasing effect on the turbulent burning velocity. DL instabilities can be related to the Markstein length  $L_M$ , which depends on the Lewis number  $Le$ . This implies that a DL instability and a thermal-diffusive instability cannot be fully separated. Kadowaki presented a relation between the Lewis number and the increase in burning velocity during formation of cellular flames. This relation was used for a third and fourth model modification. The third model includes the correction for all temperatures, while the fourth is only applied to elevated temperatures.

The third study was on the effect of anisotropic turbulence on flame stretch. In fully developed channel flow turbulence cannot be assumed isotropic and thus both  $\kappa_{mean}$  and  $\kappa_t$  were redefined. However, by modifying both parameters in the model, the code was not able to converge numerically, caused by the modification of  $\kappa_{mean}$ . Therefore only  $\kappa_t$  was considered. This led to the fifth modification.

Based on the five modifications a final modification was proposed that includes both the Lewis number correction and the anisotropic  $\kappa_t$ . In contrast to the other modifications, these two are well supported by theory. The resulting flashback prediction accurately matches the experiments for all three temperatures and therefore the improved model shows superior accuracy compared to the original model. The improved model is recommended for future BLF predictions and will be used in the following chapter to study the effect of flow divergence on flashback tendency.

## 4 Effect of a Diverging Flow on Flashback Tendency

In order to use the improved BLF prediction model for geometries that are more complex than straight channels and tubes, a good understanding of the effect of the geometry on flashback tendency is required. Therefore, in this chapter the flashback tendency of a straight channel is compared to two diverging channels with inclinations of 2 deg and 4 deg, respectively. Experimental results obtained by Eichler [7] (critical velocity gradients) are converted to bulk velocities with Equation 2.76. They are plotted in Figure 47. In the diverging channels flashback initiates at the inclined wall, which is shown in Figure 48.

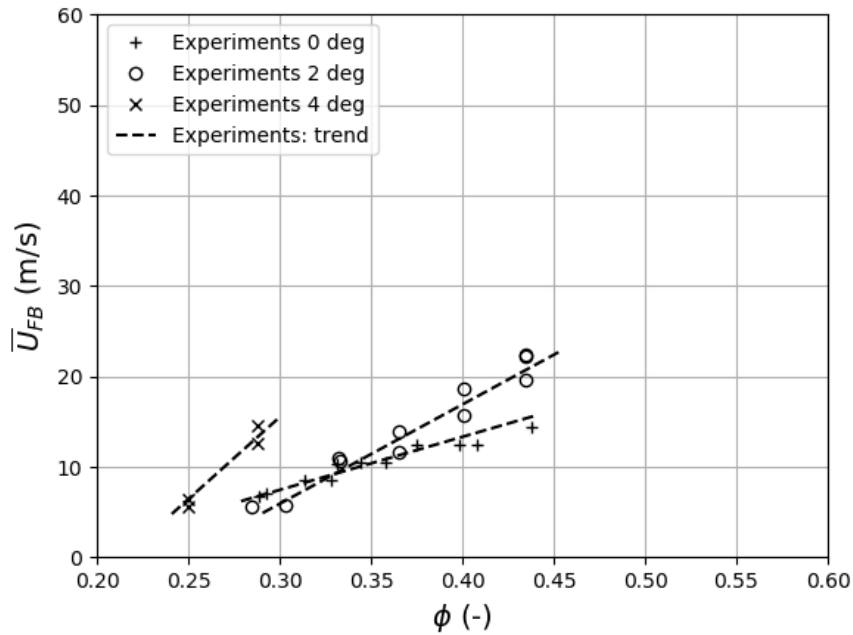


Figure 47: Experimental results from Eichler: a straight channel, a 2 deg and a 4 deg inclined channel, with  $T=293$  K. [7]

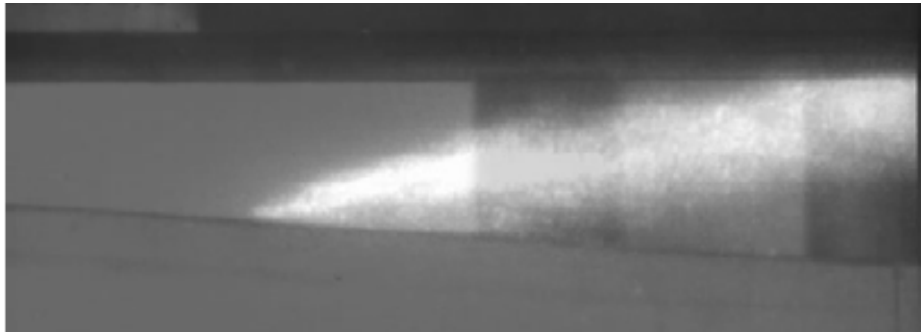


Figure 48:  $\text{OH}^*$  image of BLF of a  $\text{H}_2$ -flame in a 4 deg diffuser (from Eichler [7]).

It can be seen that an increase in channel inclination results in a steeper slope in the graphs. The straight and 2 deg results intersect at  $\phi = 0.33$ . This can be explained by the way Eichler calculates the critical velocity gradient  $g_c$ . He expresses the velocity gradient as the ratio of wall shear  $\tau$  to  $\nu$  and then  $\tau$  is estimated numerically. Eichler [7] shows that the numerical estimation of  $\tau$  may be underpredicted below  $\phi = 0.35$ . Due to the overall increase of flashback tendency the following question will be answered in this chapter:

*Why does a diverging channel lead to higher flashback limits and what physical mechanism is responsible for this?*

The approach is to first understand the effect of the geometry on the flow parameters: pressure and velocities (and their gradients), and turbulence parameters. These parameters are obtained with CFD and the results of the three channels are then compared. Then, differences in the flow parameters are used as an input of the improved BLF prediction model.

#### 4.1 Effect of the Geometry on the Flow Parameters

The channel geometries are shown in Figure 49. The CFD simulations are performed with ANSYS Fluent 19.0. [59] Unreacted, adiabatic flow is simulated for a 2D geometry with a very fine mesh (cells  $y^+ = 1$ ) close to the wall. Turbulence is modelled by the Reynolds Stress Model (RSM) to include anisotropic effects. At the inlet an uniform velocity is defined and the outlet has a pressure boundary condition. Material properties are obtained by using Cantera [41]. Also, more details on the CFD-setup are provided in the Appendix (6.2).



Figure 49: Side views of the three channels.

The point of interest for the comparison is at  $\phi = 0.35$  with an inlet velocity of 10 m/s. Below this equivalence ratio the BLF model is not valid, because it uses the unstretched laminar burning velocity, while a leaner (than  $\phi = 0.35$ ) H<sub>2</sub>-flame is only possible with sufficient stretch. Figure 50 shows the velocity profiles T  $x = 300$  mm. The diverging channels results in lower velocity magnitudes, due to the increase in flow area. However, to study the effect of the geometry, the velocity magnitudes should be equal. For this reason the CFD results are scaled.

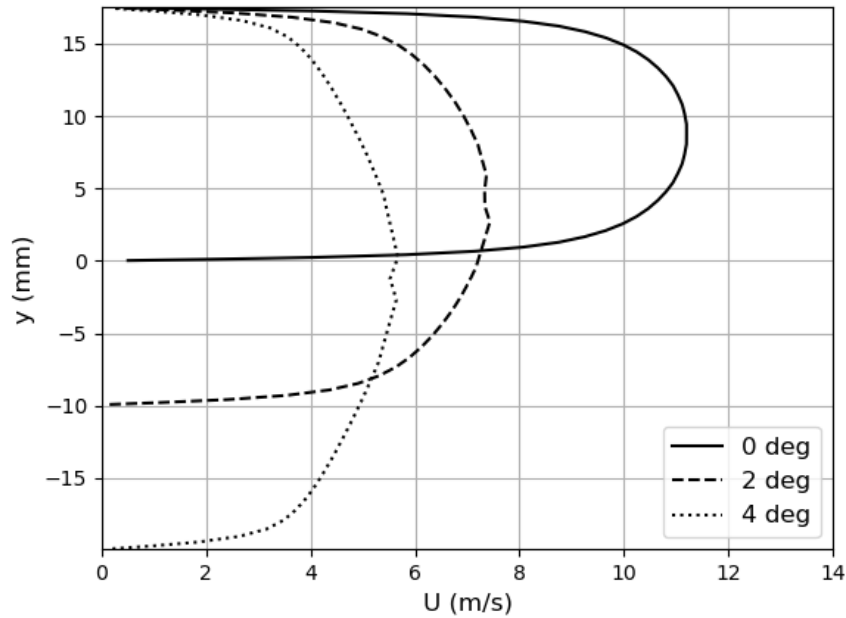


Figure 50: CFD results: velocity profiles over the full height at  $x = 300$  mm.

Three different scales have been used:  $U$ ,  $V$ , and their gradients are divided by the maximum value of  $U$  (for that geometry) and multiplied by the maximum value of  $U$  for the straight channel. For the pressure  $p$ , the Reynolds stresses  $u'u'$ ,  $v'v'$ ,  $w'w'$  and  $u'v'$  and the turbulent kinetic energy  $k$  the same has been done, but with the maximum velocities squared. For the turbulent dissipation rate  $\varepsilon$  a cubed velocity scaling is used.

The results (except the pressure) are plotted against  $y$ , at  $x = 300$  mm from the inlet. Figures 51 and 52 show the CFD results over the full channel heights and Figures 53 and 54 show them in the lower near-wall region up to  $y^+ = 40$ . The non-scaled results can be found in the Appendix (6.3).

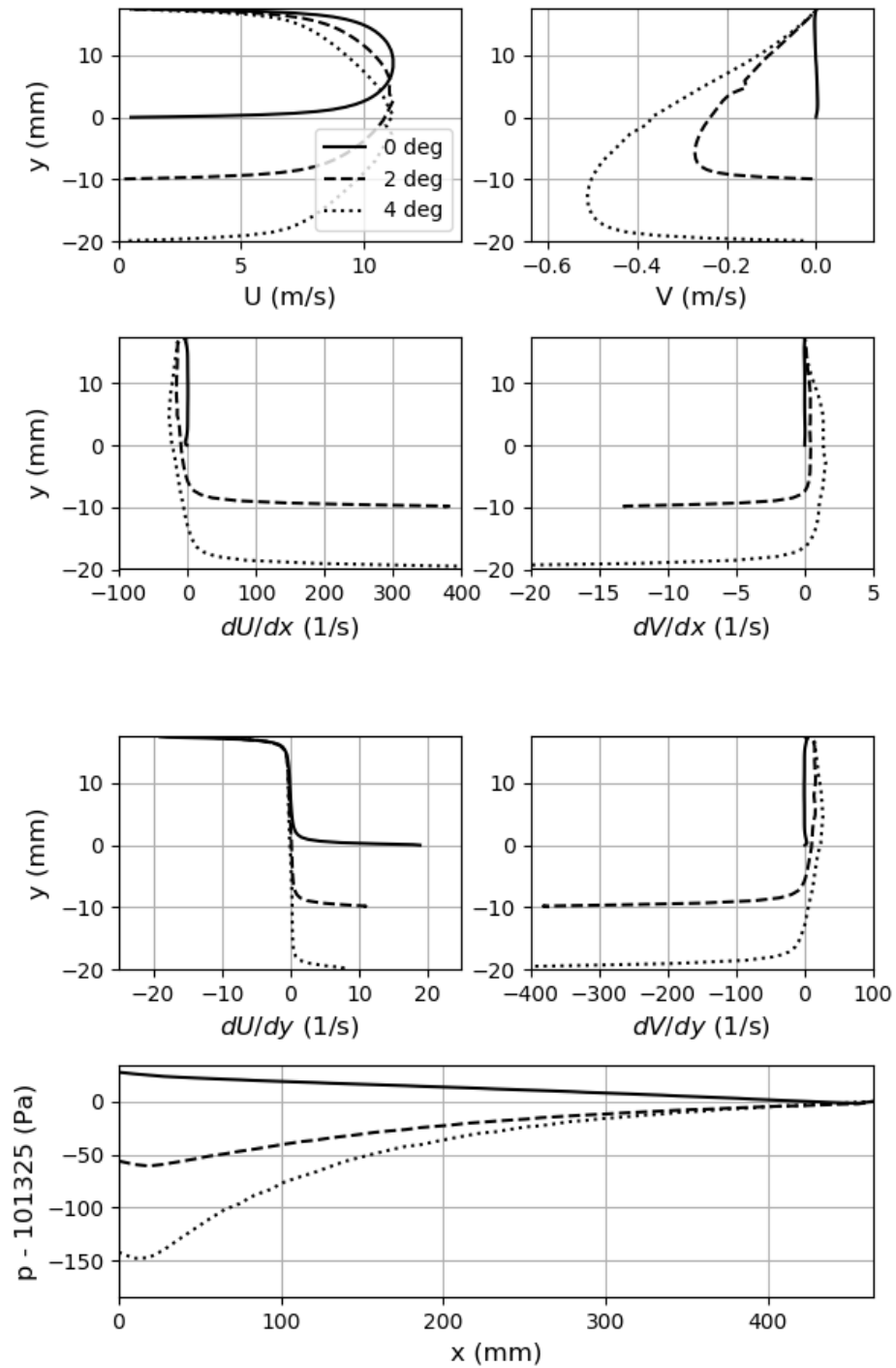


Figure 51: Scaled CFD results: velocity profiles over the full channel height at  $x = 300$  mm and the pressure over the full length at half the inlet height.

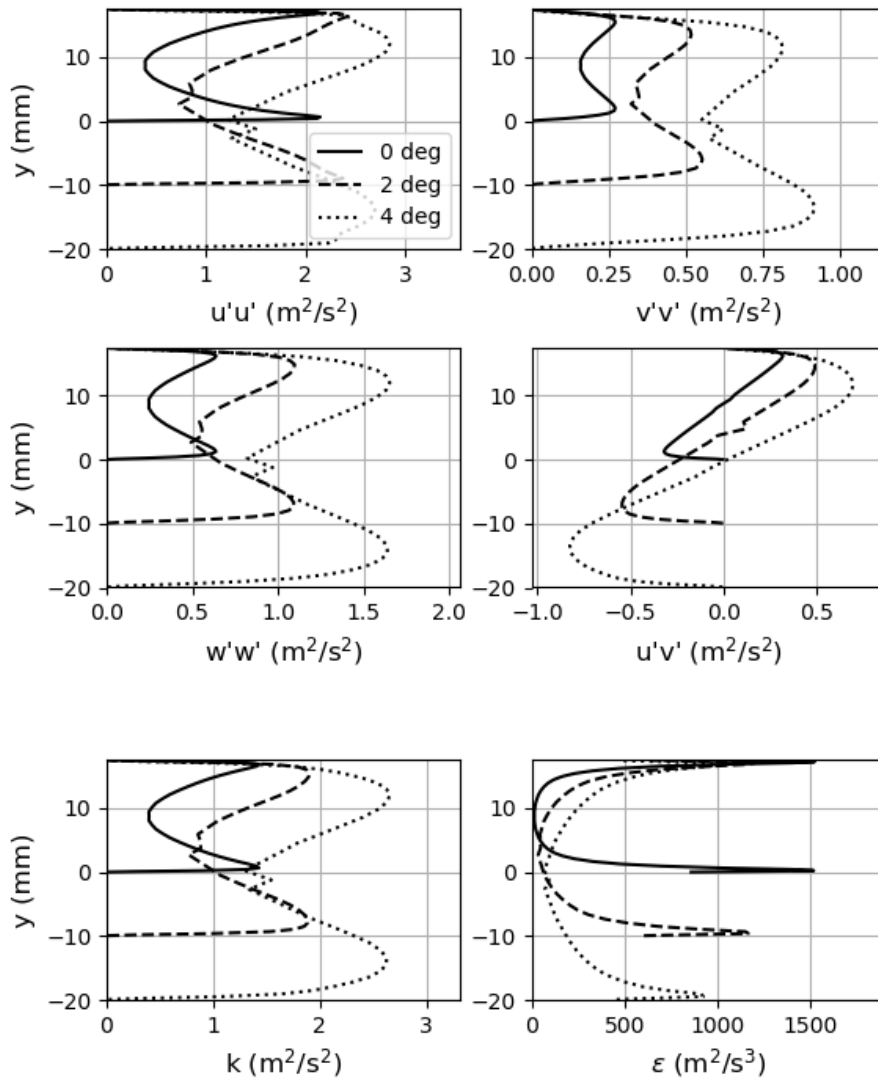


Figure 52: Scaled CFD results: turbulence profiles over the full channel height at  $x = 300$  mm.

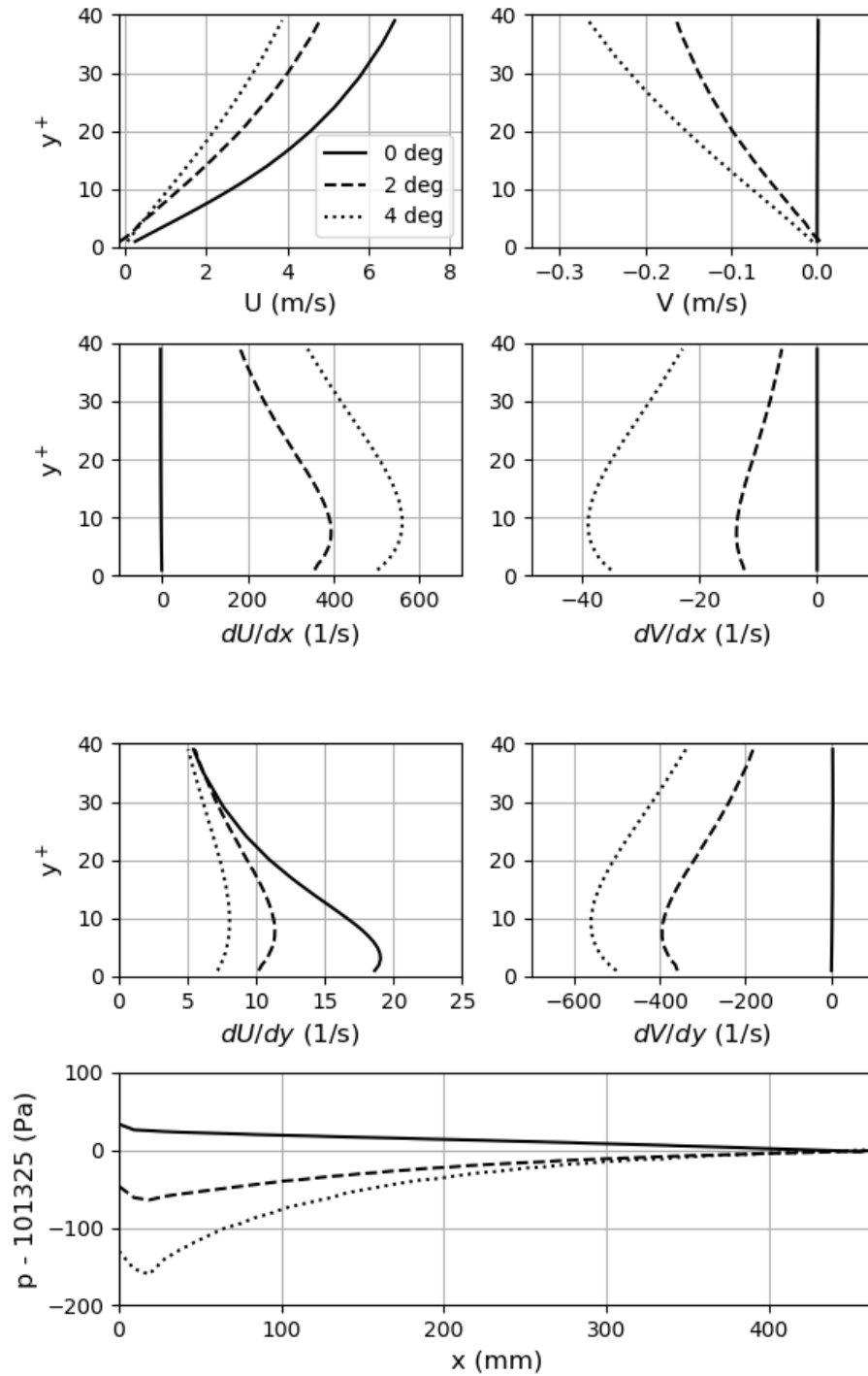


Figure 53: Scaled CFD results: velocity profiles in the lower wall region at  $x = 300$  mm and the pressure over the full length at  $y^+ = 15$ .

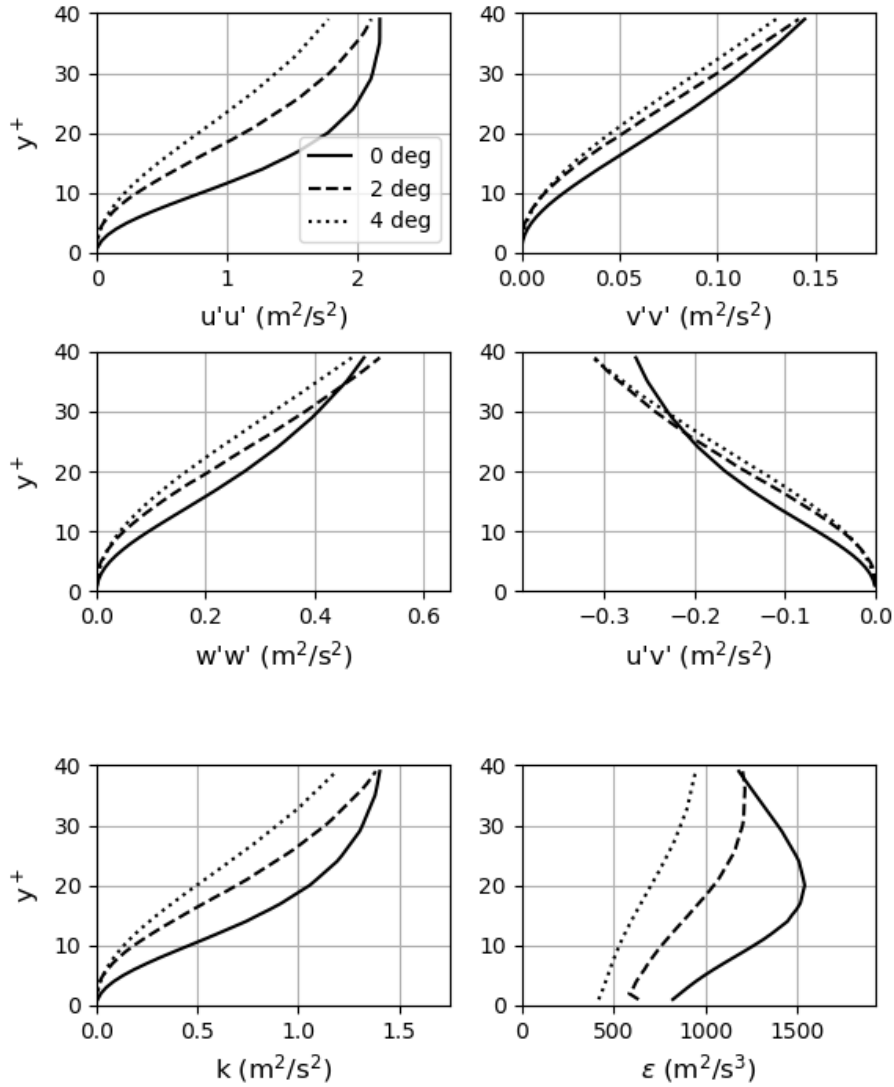


Figure 54: Scaled CFD results: turbulence profiles in the lower wall region at  $x = 300$ .

Compared to the straight channel, the diverging channels show three deviations:

1. **An adverse pressure gradient:** Due to the diverging geometry, the flow area increases and continuity results in a velocity decrease. This decrease is shown in the  $dU/dx$  graph of Figure 51, where the diverging channels take negative values in the core of the channel. The velocity decrease leads directly to an increase in pressure, since dynamic pressure is converted to static pressure. A positive pressure gradient enhances flow separation and thus flashback.
2. **High velocity gradients in the boundary layer:** All velocity gradient profiles (except for  $dU/dy$ ) show very high values increasing towards the lower wall. The peaks

are opposite to the magnitudes in the center of the channel. In other words, the velocity gradients flip signs. Figure 53 shows that an increase of inclination angle results in an increase of  $dU/dx$ ,  $dV/dx$  and  $dV/dy$ , while the  $dU/dy$  term decreases.

3. **Turbulence shifts towards the core region:** Figure 52 shows that turbulence increases, while Figure 54 shows that the turbulence close to the lower wall decreases slightly. The latter is caused by a shift of the location of maximum turbulence from the wall towards the core. This would result in a decrease of the turbulent burning velocity in the wall region and a lower tendency of BLF.

## 4.2 Effect of the Flow Parameters on Flashback Tendency

The three deviations in flow parameters will now be used in the improved BLF prediction model. The first effect is the decrease in turbulence. Based on Figure 54 a scaling is used to reduce the  $u'u'$ ,  $v'v'$  and  $w'w'$  curves. This is done by simply multiplying them with a scalar. The results are given by Figure 55. A decrease of turbulence results in lower flashback limits. This can be explained by a decrease of the turbulent burning velocity.

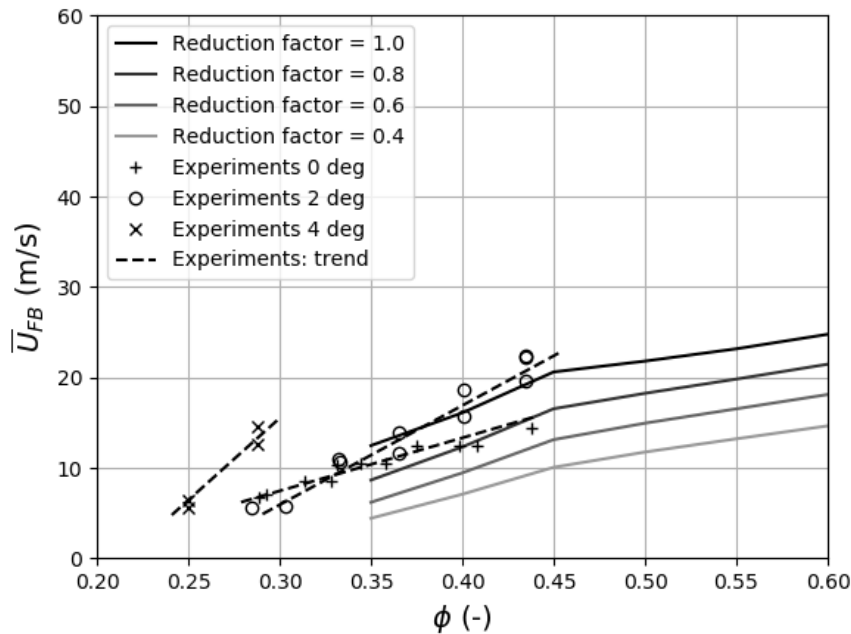


Figure 55: The effect of smaller turbulent fluctuations on flashback tendency, compared to experimental results from Eichler [7].

Second the effect of the adverse pressure gradient is implemented. This is done by adding an extra pressure term to the separation criterion. The criterion is evaluated at  $x = x_f = 0.01$  m, which is at the flame tip. This value is recommended by Baumgartner [19].

$$C_p \left( x \frac{dC_p}{dx} \right)^{0.5} = 0.39 \quad (4.1)$$

$$C_p = \frac{2 \cdot \Delta p x^2}{\rho_u U^2 x_f^2} + \frac{2 \cdot \frac{dp}{dx} x}{\rho_u U^2} \quad (4.2)$$

$$\frac{dC_p(x)}{dx} = \frac{4 \cdot \Delta p x}{\rho_u U^2 x_f^2} + \frac{2 \cdot \frac{dp}{dx}}{\rho_u U^2} \quad (4.3)$$

$$\frac{(2 \cdot \Delta p + 2 \cdot \frac{dp}{dx} x_f) (4 \cdot \Delta p + 2 \cdot \frac{dp}{dx} x_f)^{0.5}}{(\rho_u U^2)^{3/2}} = 0.39 \quad (4.4)$$

$$U = \sqrt{\frac{\left( \frac{\sqrt{8} \cdot (\Delta p + \frac{dp}{dx} \cdot 0.01) (2 \cdot \Delta p + \frac{dp}{dx} \cdot 0.01)^{0.5}}{0.39} \right)^{2/3}}{\rho_u}} \quad (4.5)$$

Different values are now given to  $\frac{dp}{dx}$  based on the pressure gradients in Figure 53. The results are compared to the experiments and this is shown in Figure 56. An increase of flashback limits is observed. While the 2 deg channel is in line with a zero pressure gradient, the 2,000 Pa/s gradient points towards the limits of the 4 deg channel.

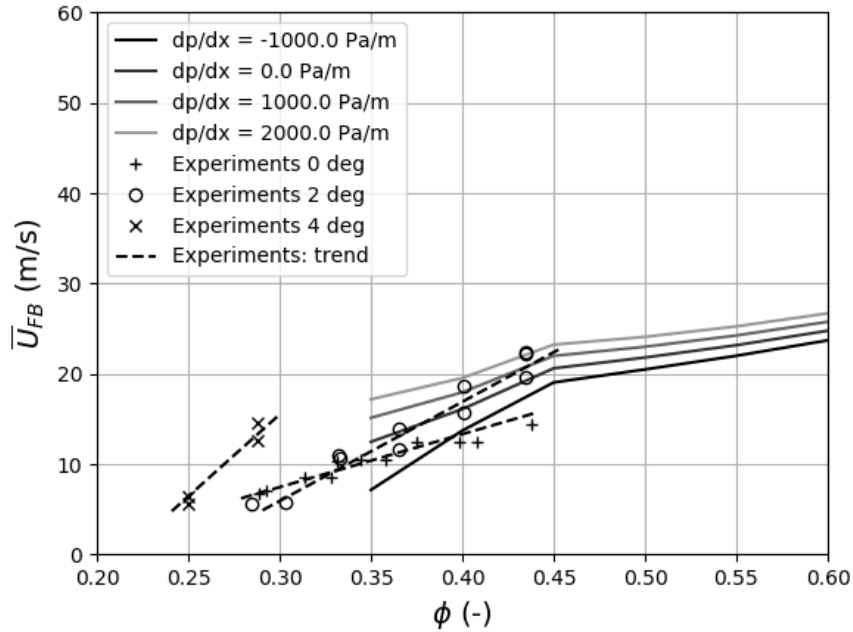


Figure 56: The effect of a pressure gradient on flashback tendency, compared to experimental results from Eichler [7].

The third effect is related to the high velocity gradients. These directly affect the flame

stretch. Equation 4.6 shows again the expression for the mean strain-induced flame stretch rate  $\kappa_{mean}$ . There the expression was simplified by assuming fully developed, incompressible flow in a symmetric plane. However, the diverging flow is not fully developed. Still the assumption for incompressible flow is valid and by choosing the xy-plane at  $z = w/2$ , which is illustrated in Figure 57, symmetry is also used.

$$\begin{aligned} \kappa_{mean} = & \left( \frac{\partial \bar{u}}{\partial x} + \frac{\partial \bar{v}}{\partial y} + \frac{\partial \bar{w}}{\partial z} \right) - \frac{1}{2 \cdot k} \left[ \overline{u'u'} \frac{\partial \bar{u}}{\partial x} + \overline{u'v'} \frac{\partial \bar{u}}{\partial y} + \overline{u'w'} \frac{\partial \bar{u}}{\partial z} \right. \\ & \left. + \overline{v'u'} \frac{\partial \bar{v}}{\partial x} + \overline{v'v'} \frac{\partial \bar{v}}{\partial y} + \overline{v'w'} \frac{\partial \bar{v}}{\partial z} + \overline{w'u'} \frac{\partial \bar{w}}{\partial x} + \overline{w'v'} \frac{\partial \bar{w}}{\partial y} + \overline{w'w'} \frac{\partial \bar{w}}{\partial z} \right] \end{aligned} \quad (4.6)$$

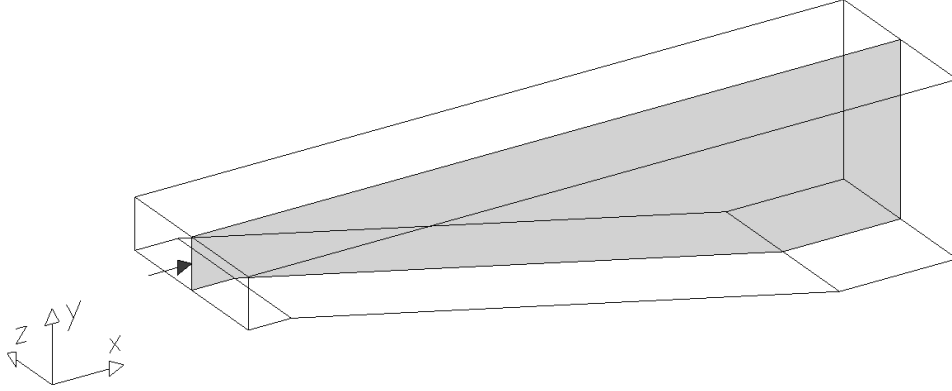


Figure 57: Symmetry plane in a diverging channel.

Due to continuity the first three terms of Equation 4.6 drop out. Then due to symmetry in  $z$  direction both the partial derivatives w.r.t.  $z$  and all terms including  $\bar{w}$  are zero. This results in Equation 4.7. Figure 58 shows the corresponding plots for the three channels.

$$\kappa_{mean} = -\frac{1}{2 \cdot k} \left[ \overline{u'u'} \frac{\partial \bar{u}}{\partial x} + \overline{u'v'} \frac{\partial \bar{u}}{\partial y} + \overline{v'u'} \frac{\partial \bar{v}}{\partial x} + \overline{v'v'} \frac{\partial \bar{v}}{\partial y} \right] \quad (4.7)$$

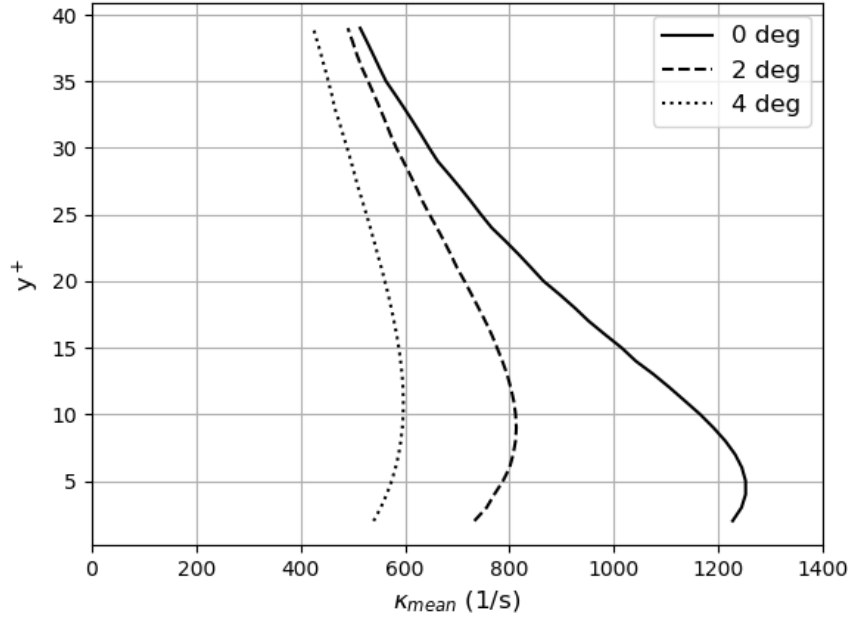


Figure 58: The mean strain-induced flame stretch rate calculated from CFD results.

The first thing Figure 58 shows is a  $\kappa_{mean}$  ranging from 500 to 1,250 1/s for the straight channel. With the assumption of isotropic turbulence Hoferichter [21] neglected the contribution of  $\kappa_{mean}$ , while the total flame stretch rate she presents, ranges from 1,000 to 8,000 1/s. This shows that isotropic turbulence can be assumed for the  $\kappa_{mean}$  term. Also, it explains why the  $\kappa_{mean}$  term in the anisotropic modification (discussed in Section 3.4) was not the main contributor.

Secondly, the diverging flows have a lower  $\kappa_{mean}$ . The diverging flows have non-zero values for all four terms of Equation 4.7, while the straight channel has only a non-zero second term. However, the  $dU/dy$  term is larger for the straight channel, resulting in a higher  $\kappa_{mean}$ .

It is hard to decide now how  $\kappa_{mean}$  should be changed in the improved BLF model, since  $\kappa_{mean}$  was never taken into account. Also, in Section 3.4 it was discussed that a modification of  $\kappa_{mean}$  led to a model crash. Compared to  $\kappa_{mean} = 0$  an increase could be implemented, while the  $\kappa_{mean}$ 's of the diverging channels suggest a decrease compared to the straight channel. For this reason a  $\kappa_{mean}$  has been varied from -1,000 to 500 1/s. The results are given by Figure 59.

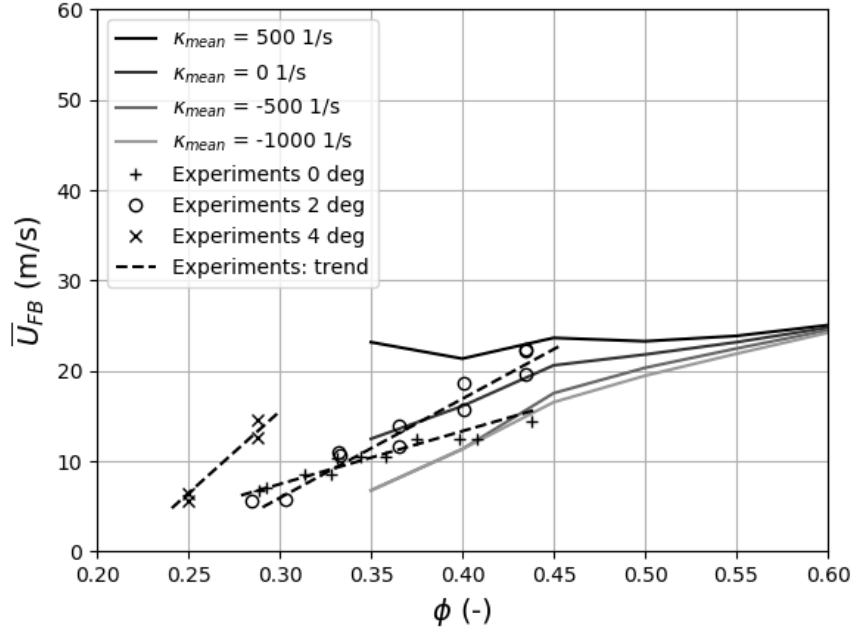


Figure 59: The effect of additional flame stretch on flashback tendency, compared to experimental results from Eichler [7].

From the results it can be seen that an increase in  $\kappa_{mean}$  leads to higher flashback limits. However, this is not in line with the higher flashback limits for the diverging flows, since these have a lower  $\kappa_{mean}$  than the straight flow.

### 4.3 Conclusion

This chapter used the improved BLF model to study the effect of a diverging geometry on flashback tendency. CFD was performed in three different channels: a straight channel, a 2 deg and a 4 deg diverging channel. Cold flow simulations with a refined mesh in the boundary layer were performed with a RSM turbulence model. Besides the velocity and pressure gradients, this led to insights in directional turbulence close to the wall.

In the flow parameters three major differences were observed between the straight and diverging flows: a decrease in turbulent fluctuations, an adverse pressure gradient and high velocity gradients in the boundary layer. These changes were used as an input for the improved BLF model to evaluate their effect on flashback tendency.

It has been shown that both the original and the improved BLF model's do not take into account  $\kappa_{mean}$  and CFD results of the straight channel show that this is a valid assumption. Different values were used to show the effect of  $\kappa_{mean}$  on the flashback tendency. Although  $\kappa_{mean}$  and the turbulence parameters (in the wall region) are weaker in the diverging flows, the flashback limits are higher. This is caused by an adverse pressure gradient, which is due to continuity: a diverging flow loses speed by expanding and this results in an increasing static pressure.

## 5 Conclusion and Recommendations

Using pure hydrogen combustion for industrial gas turbines contributes to solving the imbalance between fluctuating renewable power supply and required power. CO<sub>2</sub> emissions are eliminated and by using lean premixed combustion also NO<sub>x</sub> emissions are minimized. Due to the high diffusivity and burning velocity of hydrogen, flame flashback is a serious threat for premixed hydrogen combustion. One of the most important flashback types for hydrogen premixed flames is boundary layer flashback (BLF). Within the past 5 years a semi-analytical model has been developed by TU Munich to predict BLF. This model has only been validated for atmospheric conditions, while for gas turbines operating temperatures and pressures are much higher. Also, the validation applies only to simple geometries and cannot be used for new burner concepts. This leads to the thesis objective:

- *To improve the semi-analytical boundary layer flashback model and, by feeding the model with Computational Fluid Dynamics (CFD) results, to study the effect of a geometry change on flashback tendency.*

The thesis has been divided into three parts. First an *exploring* chapter explains the BLF model from TU Munich, its main assumptions and critical parameters. After a historical overview of BLF theory, background theory is provided on relevant concepts: the Stratford criterion, the turbulent burning velocity, the stretched laminar burning velocity, the Markstein length and turbulence. The model is then explained and discussed, resulting in the critical assumptions and parameters:

- The assumption of isotropic turbulence
- The assumption of no effect of the flame on upstream turbulence
- The critical parameter: the turbulent burning velocity  $S_t$
- The critical parameter: the Markstein length  $L_M$  and the effect of flame instabilities

The *improving* chapter focuses on specific phenomena with the goal of improving the model. It is shown first how the original model is duplicated. Then three topics are discussed: turbulence-flame interaction, flame instabilities and flame stretch. This leads to five model modifications that were compared to the original model and experiments of Eichler:

- Another expression for the turbulent burning velocity, based on a correlation proposed by Lin
- Another fluctuations curve, based on Jain's experiments to account for the upstream effect of the flame on turbulence
- A correction factor for the turbulent burning velocity as a function of the Lewis number, to account for cellular flame formation (one for all temperatures and one for elevated temperatures only)
- A modified expression for the turbulence-induced flame stretch that includes anisotropic turbulence

A combination of two modifications, the correction factor and the anisotropic  $\kappa_t$ , resulted in significant improvements. The resulting flashback prediction accurately matches the experiments and therefore the improved model is recommended for future BLF predictions.

Finally the *applying* chapter uses the improved model to study the effect of a diverging geometry on flashback tendency. With experimental results being available for a 2 deg and 4 deg channel, this is a first step towards the validation of the model for different geometries. With the use of Computational Fluid Dynamics (CFD) the flow through the channels is modelled and relevant flow parameters are obtained. Three major differences between the diverging and straight flows are used as an input of the improved BLF model. It was shown that an adverse pressure gradient is responsible for a higher flashback tendency for a diverging channel compared to a straight channel/

Together these chapters result in a better understanding of BLF and an improved prediction model, validated for gas turbine relevant temperatures, that can be used to study the effect of geometrical modifications on flashback tendency. This is a tool that could significantly contribute to the development of lean premixed hydrogen burners.

However, based on the underlying physical concepts, the model's applications are limited. Firstly the Stratford separation criterion, which is derived for 1D flow, should be adapted to 2D flow. Next to this the model is based on two uncertain parameters: the Markstein length  $L_M$  and the turbulent burning velocity  $S_t$ . For the Markstein length no general expression exists yet and for both parameters the uncertainty increases for lean hydrogen-air mixtures. On top of this they are also difficult to obtain experimentally.

Recommendations for future research includes:

- Experimental studies of BLF of lean premixed hydrogen combustion for different burner geometries. The currently available experimental results are limited to straight channels, 2 and 4 deg channels and tubes. Also, only for the straight channel elevated temperatures are tested for. Eventually experiments should be performed at gas turbine operating conditions (elevated pressures and temperatures).
- Fundamental studies of the Markstein length of lean hydrogen-air mixtures. Only at room temperatures the Markstein length can be predicted and this is still without good accuracy. For elevated temperatures and pressures no solid theories exist yet. The Markstein length is of great importance for lean premixed hydrogen flames at high temperatures, because it plays an important role in the stretched burning velocity and flame instabilities.
- Further improvement of the prediction model. This can be done by extending the Stratford criterion to 2D and by using advanced CFD simulations to obtain more accurate flame stretch rates. Also, CFD simulations could be used to get information on local flow properties (velocity and pressure gradients) in new geometry concepts. A correlation between flashback limits (from experiments) and a momentum balance (velocity versus pressure gradient) could be found that gives insight on the effect of the geometry on boundary layer flashback tendency.

## References

- [1] International Energy Agency. Statistics - total primary energy supply (tpes) by source\*. <http://www.iea.org/statistics>.
- [2] Gurutze Arzamendi Luis M. Gandia and Pedro M. Diéguez. Renewable hydrogen energy: An overview. In Luis M. Gandia and Pedro M. Diéguez, editors, *Renewable hydrogen technologies: production, purification, storage, applications and safety.*, chapter 1, pages 1–18. Elsevier, 2013.
- [3] Ad van Wijk. The green hydrogen economy in the northern netherlands. Technical report, Noordelijke Innovation Board, 2018.
- [4] How nitrogen oxides affect the way we live and breathe. Technical report, Environmental Protection Agency, 1998.
- [5] S. Verhelst et al. Update on the progress of hydrogen-fueled internal combustion engines. In Luis M. Gandia and Pedro M. Diéguez, editors, *Renewable hydrogen technologies: production, purification, storage, applications and safety.*, chapter 16, pages 381–400. Elsevier, 2013.
- [6] Técnico Lisboa. Flame stabilization. <https://fenix.tecnico.ulisboa.pt>.
- [7] C. Eichler. *Flame flashback in wall boundary layers of premixed combustion systems*. PhD thesis, Technische Universität München, 2011.
- [8] F.A. Hatem. *Flashback analysis and avoidance in swirl burners*. PhD thesis, Cardiff University School of Engineering, 2017.
- [9] M.A.H. Al-fahham. *A modelling and experimental study to reduce boundary layer flashback with microstructure*. PhD thesis, Cardiff University School of Engineering, 2017.
- [10] Vera Hoferichter. *Boundary Layer Flashback in Premixed Combustion Systems*. PhD thesis, Technische Universität München, 2017.
- [11] Ali Cemal Benim and Khawar J. Syed. *Flashback Mechanisms in Lean Premixed Gas Turbine Combustion*. Elsevier, The Boulevard, Langford Lane, Kidlington, Oxford OX5 1GB, UK, 2015.
- [12] E. Sullivan-Lewis A. Kalantari and V. McDonell. Flashback Propensity of Turbulent Hydrogen–Air Jet Flames at Gas Turbine Premixer Conditions. *Journal of Engineering for Gas Turbines and Power*, 138, 2016.
- [13] E. Sullivan-Lewis A. Kalantari and V. McDonell. Application of a Turbulent Jet Flame Flashback Propensity Model to a Commercial Gas Turbine Combustor. *Journal of Engineering for Gas Turbines and Power*, 139, 2017.
- [14] A. Kalantari and V. McDonell. Boundary layer flashback of non-swirling premixed flames: Mechanisms, fundamental research, and recent advances. *Progress in Energy and Combustion Science*, 61:249–292, 2017.

- [15] G. Baumgartner C. Eichler and T. Sattelmayer. Experimental Investigation of Turbulent Boundary Layer Flashback Limits for Premixed Hydrogen-Air Flames Confined in Ducts. *Journal of Engineering for Gas Turbines and Power*, 134(011502), 2012.
- [16] C. Eichler and T. Sattelmayer. Premixed flame flashback in wall boundary layers studied by long-distance micro-PIV. *Exp fluids*, 52:347–360, 2012.
- [17] A. Gruber et al. Turbulent flame–wall interaction: a direct numerical simulation study. *J. Fluid Mech.*, 658:5–32, 2010.
- [18] A. Gruber et al. Direct numerical simulation of premixed flame boundary layer flashback in turbulent channel flow. *J. Fluid Mech.*, 709:516–542, 2012.
- [19] G. Baumgartner. *Flame Flashback in Premixed Hydrogen-Air Combustion Systems*. PhD thesis, Technische Universität München, 2014.
- [20] L.R. Boeck G. Baumgartner and T. Sattelmayer. Experimental Investigation of the Transition Mechanism From Stable Flame to Flashback in a Generic Premixed Combustion System With High-Speed Micro-Particle Image Velocimetry and Micro-PLIF Combined With Chemiluminescence Imaging. *Journal of Engineering for Gas Turbines and Power*, 138(021501), 2016.
- [21] Christoph Hirsch Vera Hoferichter and Thomas Sattelmayer. Prediction of confined flame flashback limits using boundary layer separation theory. *Proceedings of ASME Turbo EXPO 2016*, 2016.
- [22] B. Lewis and G. von Elbe. Stability and Structure of Burner Flames. *The journal of chemical physics*, 11:75–96, 1943.
- [23] B. S. Stratford. The prediction of separation of the turbulent boundary layer. *J. Fluid Mech.*, 5(1):1–16, 1959.
- [24] Stavros Tavoularis. Additional notes. <http://by.genie.uottawa.ca/mcg4345/AdditionalNotes/AdditionalNotes.pdf>.
- [25] N. Peters. *Turbulent Combustion*. Cambridge University Press, Cambridge, UK, 2000.
- [26] N. Peters. Lecture 13 - the turbulent burning velocity. <https://cefrc.princeton.edu/sites/cefrc/files/Files/2010%20Lecture%20Notes/Norbert%20Peters/Lecture13.pdf>.
- [27] F. Güthe E.M. Burke and R.F.D. Monaghan. A comparison of turbulent flame speed correlations for hydrocarbon fuels at elevated pressures. *Proceedings of ASME Turbo EXPO 2016*, 2016.
- [28] Yasuhiro Ogami. Jhon Pareja, Hugo J. Burbano. Measurements of the laminar burning velocity of hydrogen–air premixed flames. *International Journal of Hydrogen Energy*, 35:1812–1818, 2010.
- [29] R.K. Kumar G.W. Koroll and E.M. Bowles. Burning velocities of hydrogen-air mixtures. *Combustion and Flame*, 94:330–340, 1993.

- [30] S. Daniele et al. Turbulent flame speed for syngas at gas turbine relevant conditions. *Proceedings of the Combustion Institute*, 33:2937–2944, 2011.
- [31] Peter Jansohn Yu-Chun Lin and Konstantinos Boulouchos. Turbulent flame speed for hydrogen-rich fuel gases at gas turbine relevant conditions. *International Journal of Hydrogen*, 39:20242–20254, 2014.
- [32] Thierry Poinso and Denis Veynante. *Theoretical and Numerical Combustion*. Edwards, Philadelphia, PA 19118 USA., 2005.
- [33] L. Tay Wo Chong et al. Influence of strain and heat loss on flame stabilization in a non-adiabatic combustor. *Proceedings of the European Combustion Meeting*, pages 1–6, 2009.
- [34] D. Veynante et al. Experimental analysis of flame surface density models for premixed turbulent combustion. *Twenty-Sixth Symposium (International) on Combustion/The Combustion Institute*, pages 413–420, 1996.
- [35] C. Meneveau and T. Poinso. Stretching and quenching of flamelets in premixed turbulent combustion. *Combustion and Flame*, 86:311–332, 1991.
- [36] G.K. Giannakopoulos et al. Consistent definitions of “flame displacement speed” and “markstein length” for premixed flame propagation. *Combustion and Flame*, 162:1249–1264, 2015.
- [37] Simon Crispin Taylor. *Burning velocity and the influence of flame stretch*. PhD thesis, University of Leeds, 1991.
- [38] Bendiks J. Boersma Frans T.M. Nieuwstadt and Jerry Westerweel. *Turbulence: Introduction to Theory and Applications of Turbulent Flows*. Springer International Publishing Switzerland, 2016.
- [39] P.R. Spalart. Direct simulation of a turbulent boundary layer up to  $re=1410$ . Technical report, NASA, 1986.
- [40] J.K. Bechtold and M. Matalon. The dependence of the markstein length on stoichiometry. *Combustion and Flame*, 127:1906–1913, 2001.
- [41] Cantera Developers. Cantera 2.3.0. <https://www.cantera.org>, 2001–2018.
- [42] Jr. John D. Anderson. *Fundamentals of Aerodynamics*. McGraw-Hill Education, 2 Pennsylvania Plaza New York City, 2011.
- [43] Python Software Foundation. Python 3.6.5. <https://www.python.org/>, 2001–2018.
- [44] A.N. Lipatnikov and J. Chomiak. Effects of premixed flames on turbulence and turbulent scalar transport. *Progress in Energy and Combustion Science*, 36:1–102, 2010.
- [45] C. Jainski et al. Quenching of premixed flames at cold walls: Effects on the local flow field. *Flow Turbulence Combust*, 100:177–196, 2018.
- [46] T. Wei and W.W. Willmarth. Reynolds-number effects on the structure of a turbulent channel flow. *Journal of Fluid Mechanics*, 204:57–95, 1989.

- [47] C. Clanet and G. Searby. First experimental study of the darrieus-landau instability. *Physical Review Letters*, 80(17), 1998.
- [48] E.C. Okafor et al. Effects of hydrogen concentration on premixed laminar flames of hydrogen-methane-air. *International Journal of Hydrogen Energy*, 39:2409–2417, 2014.
- [49] G. Troiani et al. Experimental investigation of darrieus-landau instability effects on turbulent premixed flames. *Proceedings of the Combustion Institute*, 35:1451–1459, 2015.
- [50] B.E. Gelfand et al. *Thermo-Gas Dynamics of Hydrogen Combustion and Explosion*. Springer-Verlag, Berlin Heidelberg, 2012.
- [51] M.S. Day A.J. Aspden and J.B. Bell. Characterization of low lewis number flames. *Proceedings of the Combustion Institute*, 33:1463–1471, 2011.
- [52] M. Hertzberg. Selective diffusional demixing: occurrence and size of cellular flames. *Progress in Energy and Combustion Science*, 15:203–239, 1989.
- [53] P. Venkateswaran et al. Measurements and analysis of turbulent consumption speeds of h<sub>2</sub>/co mixtures. *Combustion and Flame*, 158:1602–1614, 2011.
- [54] P. Venkateswaran et al. Scaling turbulent flame speeds of negative markstein length fuel blends using leading points concepts. *Combustion and Flame*, 162:375–387, 2015.
- [55] M. Zaytsev and V. Bychkov. Effect of the darrieus-landau instability on turbulent flame velocity. *Physical Review*, 66, 2002.
- [56] S. Kadowaki. Flame velocity of cellular flames at low lewis numbers. *Combustion Sciences and Technology*, 162:223–234, 2001.
- [57] C.E. Frouzakis et al. Numerical study of unstable hydrogen/air flames: Shape and propagation speed. *Proceedings of the Combustion Institute*, 35:1087–1095, 2015.
- [58] John Laufer. Investigation of turbulent flow, two-dimensional channel. Technical report, NACA, 1951.
- [59] Inc. Ansys. Ansys 19.0. <https://www.ansys.com/>, 2018.

# 6 Appendix

## 6.1 BLF Model - Python Code

```
import numpy as np
from scipy.optimize import fsolve
import cantera as ct
import LFS as LFS
import matplotlib.pyplot as plt

def BLFmodel(C,PRINT):

    ### Creating empty Lists -----
    T_ad_list = []
    phi_list = []
    S_l0_list = []
    S_ls_list = []
    Lm_list = []
    u_fluc_tau_list = []
    y_plus_list = []
    Le_list = []
    LE_list = []
    kappa_list = []
    U_FB_bar_list = []
    u_fluc_list = []
    kappa_ratio_list = []
    Re_list = []
    Ka_list = []
    TI_x_list = []
    TI_y_list = []
    TI_loc_list = []
    flame_x_list = []
    flame_y_list = []
    Local_Error_List = []

    ### Starting the Loops (mm for different cases, m for different equivalence ratios) -----
    for mm in range(1,5,1):
        for m in range(9,21,1):
            if mm==5 and m==9:
                m=10

            phi = m/20.-0.1
            if mm==1:

                T_u = 293
                GEOMETRY =1
            if mm==2:
                T_u = 473
                GEOMETRY =1
            if mm==3:
                T_u = 673
                GEOMETRY =1
            if mm==4:
                T_u = 293
                GEOMETRY =2

            p_u = 101325
            R = 8.314
            Ea = 125604.
            Le_O2 = 2.32
            Le_H2 = 0.33
            gamma2 = 1.

            h = 0.0175
            w = 0.157
            if GEOMETRY==1:
                D_h = ((w*h)/3.14)**0.5 * 2
            if GEOMETRY==2:
                D_h = 0.04

    ### An equilibrium reaction (with Cantera) results in burned properties -----
    gas1 = ct.Solution('gri30.xml')
    mix = 'H2:'+str(2*phi)+'', O2:1, N2:3.76'
    gas1.transport_model = 'Multi' # 'Multi' or 'Mix'
    gas1.X = mix
    gas1.TP = T_u,p_u
    rho_u = gas1.TD[1]
    cp_u = gas1.cp_mass
    lambda_u = gas1.thermal_conductivity
    LE = lambda_u / (np.dot((gas1.X),(gas1.mix_diff_coeffs_mole))*rho_u*cp_u)
    mu_u = gas1.viscosity
    thermal_diff_u = lambda_u / (rho_u * cp_u)
    gas1.equilibrate('HP', solver='gibbs')
```

```

cp_b = gas1.cp_mass
lambda_b = gas1.thermal_conductivity
T_ad = gas1.T
rho_b = gas1.TD[1]
thermal_diff_b = lambda_b / (rho_b * cp_b)

S_l0 = LFS.inter(phi,T_u,p_u*10**(-5))
sigma = rho_u / rho_b
gamma1 = sigma
deltaf = 2*lambda_u / (rho_u * cp_u * S_l0)
beta = Ea*(T_ad - T_u)/(R*T_ad**2)
A = 1+ beta*(1/phi-1)
Le = 1+ (Le_O2 - 1 + A*(Le_H2-1))/(1+A)
alfa = gamma1 + 0.5*beta*(Le-1)*gamma2
Lm = deltaf*(alfa-(sigma-1))*(gamma1/sigma)
l_t = 0.07 * D_h
s = np.log10(l_t/deltaf)

error = 10
count = 0
U_FB = 1
while abs(error)>0.01:
    def equation1(eq1):
        u_tau = eq1
        if GEOMETRY ==1:
            return ((U_FB-2.4*u_tau)/u_tau - (1/0.41 * np.log((h/2.*u_tau)/(mu_u/rho_u)) + 5 - 1/0.41))
        if GEOMETRY ==2:
            return (u_tau**2 - (0.03955 * (U_FB-2.4*u_tau)**(7/4.)*(mu_u/rho_u)**(1/4.)*(D_h)**(-1/4.)))
        u_tau = fsolve(equation1,0.1,xtol=1.49012e-2)
    S_t = 0
    if mm==1 and m==9:
        imax = 50
    else:
        imax = 50
    for i in range(5,imax,1):
        y = i * (mu_u/(rho_u*u_tau))
        u_fluc = u_tau*(2.661 - 7.211*np.log(u_tau*y*rho_u/mu_u) + 7.600*np.log(u_tau*y*rho_u/mu_u)**2
                - 2.900*np.log(u_tau*y*rho_u/mu_u)**3 + 0.472*np.log(u_tau*y*rho_u/mu_u)**4
                - 0.028*np.log(u_tau*y*rho_u/mu_u)**5)

# MODIFICATION: Jainski's fluctuation
# u_fluc = u_tau*(-0.00000015613432*(u_tau*y*rho_u/mu_u)**6 + 0.00002729809731*(u_tau*y*rho_u/mu_u)**5
# - 0.000172250265584*(u_tau*y*rho_u/mu_u)**4 + 0.0046443496*(u_tau*y*rho_u/mu_u)**3
# - 0.0485448388*(u_tau*y*rho_u/mu_u)**2 + 0.1590653579*(u_tau*y*rho_u/mu_u) + 1.9742528316)
Gamma = 10**(-1/(s+0.4)*np.exp(-(s+0.4))+(1-np.exp(-(s+0.4)))*(2/3.*(1-1/2.*np.exp(-(u_fluc/S_l0)**(1/3.))))*s-0.11 ))

# MODIFICATION: Anisotropic flame stretch
# v_fluc = u_tau*(-0.00052*(u_tau*y*rho_u/mu_u)**2 + 0.045873*(u_tau*y*rho_u/mu_u) - 0.014410)
# w_fluc = u_tau*1.4*(-0.00052*(u_tau*y*rho_u/mu_u)**2 + 0.045873*(u_tau*y*rho_u/mu_u) - 0.014410)
# k = 1/2. * (u_fluc**2 + v_fluc**2 + w_fluc**2)
# kappa_mean = (-0.1*np.log10(U_FB*D_h*rho_u/mu_u)+0.91)*u_fluc*v_fluc/(2*k) * (1/7.*U_FB*(y/(h/2.))**(-6/7.)) * 2./h
# kappa_turb = Gamma*u_fluc*v_fluc*w_fluc/(l_t*k)
kappa_mean = 0.
kappa_turb = 2/3. * Gamma*u_fluc/l_t
kappa_s = 1/2.*u_fluc/l_t
kappa = (kappa_mean + kappa_turb + kappa_s)
S_ls = S_l0 - kappa*Lm
S_t_new = (S_ls*(1+C*(u_fluc/S_ls)**0.5))

# MODIFICATION: Lin's correlation
# S_t_new = 10.5 * S_l0 * (Le**(-0.82)) * (u_fluc/S_l0)**0.45 * (l_t/deltaf)**(-0.41)
# * (100000/p_u)**0.75 * (293/T_u)**(-1.33)

# MODIFICATION: Lewis correction for elevated temperatures only
# if T_u > 200:
#     if Le < 1.0 and Le >=0.50:
#         S_t_new = (0.6052*(1/Le)**2 - 1.1314*(1/Le) + 1.5224) * S_t_new # only valid down to phi = 0.5
#     if Le < 0.50:
#         S_t_new = S_t_new * 1.678

## MODIFICATION: Lewis correction for all temperatures
# if T_u > 200:
#     if Le < 1.0 and Le >=0.50:
#         S_t_new = (0.6052*(1/Le)**2 - 1.1314*(1/Le) + 1.5224) * S_t_new # only valid down to phi = 0.5
#     if Le < 0.50:
#         S_t_new = S_t_new * 1.678

if S_t_new > S_t:

```

```

S_t = S_t_new
Y = u_tau * y * rho_u / mu_u
kappa_FB, Gamma_FB, S_ls_FB = kappa, Gamma, S_ls
u_fluc_FB = u_fluc
S_l0_FB = S_l0
S_ls_FB = S_ls
Ka = (u_fluc / S_l0)**(3/2.) * (l_t/deltaf)**(-1/2.)
u_TAU = u_tau

if mm==1 and m==9 and count==0:
    u_fluc_tau_list.append(u_fluc/u_tau)
    y_plus_list.append(y * u_tau * rho_u / mu_u)

### Stratford's criterium -----
dp_max = rho_u * S_t**2 * (T_ad/T_u - 1)
dpx = 0.
U_FB_new = (((dp_max + dpx*0.01)*(2*dp_max+dpx*0.01)**0.5 / 0.39)**(2/3.) * 2/rho_u)**0.5

error = U_FB_new - U_FB
U_FB = U_FB_new
count = count+1

if Ka > 1:
    flame = 'Thin reaction zone'
elif Ka < 1:
    flame = 'Corrugated flamelets'

U_FB_bar = U_FB[0] - 2.4*u_TAU[0]

if PRINT == 1:
    print('T_u = ', T_u, 'K ', 'phi = ', round(phi, 2), ' ', 'U_FB_bar = ', round(U_FB_bar, 1), 'm/s ',
          'u_fluc_FB/S_ls_FB = ', round(u_fluc_FB[0]/S_ls_FB[0], 1), ' ', 'l_t/deltaf = ', round(l_t/deltaf, 1),
          ' ', 'y+FB = ', round(Y[0], 0), ' ', 'Re_h = ', round(U_FB_bar*h*rho_u/mu_u, 0), ' ', flame)
    print(' ')

if m==20:
    print(' ')
    print('-----')

print(' ')

### Filling Lists -----
Re_list.append(round(U_FB_bar*h*rho_u/mu_u, 0))
Ka_list.append(float(Ka))
TI_x_list.append(float(((mu_u/rho_u)**3*l_t/(u_fluc_FB)**3)**(1/4.)/deltaf))
TI_y_list.append(float(u_fluc_FB/(2*S_l0)))
TI_loc_list.append(round(u_fluc_FB[0]/S_ls_FB[0], 1))
flame_x_list.append(l_t/deltaf)
flame_y_list.append(u_fluc_FB/S_l0_FB)
phi_list.append(phi)
T_ad_list.append(T_ad)
S_l0_list.append(S_l0)
S_ls_list.append(S_ls)
Lm_list.append(1000*Lm)
Le_list.append(Le)
LE_list.append(LE)
kappa_list.append(kappa_FB/1000)
U_FB_bar_list.append(U_FB_bar)
u_fluc_list.append(u_fluc_FB)
kappa_ratio_list.append(100 * 2/3.*Gamma_FB/(2/3.*Gamma_FB+1/2.))

### Defining error to get best value for C, and returning outputs -----
if mm==1:
    U_FB_Data = 50.8502675059 * phi - 7.2760562413
    Local_Error_List.append(abs(U_FB_bar-U_FB_Data)/35.28)
if mm==2:
    U_FB_Data = 78.8293368674 * phi - 6.6335530372
    Local_Error_List.append(abs(U_FB_bar-U_FB_Data)/49.12)
if mm==3:
    U_FB_Data = 48.0853332972*np.log(phi) + 93.2665966307
    Local_Error_List.append(abs(U_FB_bar-U_FB_Data)/84.69)
if mm==4:
    U_FB_Data = 48.1158091256* phi - 6.6807553719
    Local_Error_List.append(abs(U_FB_bar-U_FB_Data)/32.42)

Error_total = sum(Local_Error_List)
print('C = ', round(C, 1), 'Error = ', round(Error_total, 3))
return(Error_total, U_FB_bar_list, phi_list)

```

```

### Finding optimum C -----
Error_0 = 10000.
delta_Error = 1.
C = 1.8
while delta_Error > 0:
    C = C + 0.1
    Error_1,U_FB_bar_list,phi_list = BLFmodel(C,0)
    delta_Error = Error_0 - Error_1
    Error_0 = Error_1
C_optimum = round(C - 0.1,1)
print(' ')
print('Optimum C = ',C_optimum)
print(' ')

### Evaluating for this C -----
Error_model,U_FB_bar_list,phi_list = BLFmodel(C_optimum,1)

### Default values (from Hoferichter) and experimental results (Eichler) -----
Default_Model_phi = [0.35,0.4,0.45,0.5,0.55,0.6,0.65,0.7,0.75,0.8,0.85,0.9]

Default_Model_UFB = [ 8.45698472, 10.31915582, 12.63297894, 15.51082699, 18.61602674,
21.92871719, 25.17090436, 28.52621328, 31.52168034, 34.14735101,
36.21113684, 38.31325107, 7.85085045, 12.59570915, 18.22011575,
24.2874666 , 30.4117381 , 36.43550811, 42.11137157, 47.28936131,
52.03341047, 56.27141839, 59.7308201 , 62.86691147, 23.53936365,
32.25597853, 41.01390014, 49.42428701, 57.4092592 , 64.87625382,
71.67542777, 77.94897827, 83.54016192, 88.4518415 , 92.47539058,
96.14188181, 8.74907499, 10.36201519, 12.51505931, 15.23352964,
18.17568597, 21.31713644, 24.38743799, 27.56425899, 30.39262171,
32.86334311, 34.79180371, 36.75913529]

phi_data = []
U_FB_bar_data = []
file_name="C:/Users/tober/Desktop/EPT/H2 Flashback/Experimental Data/Correct/EichlerUFB3"
f=open(file_name+".txt",'r+')
lines_data=f.readlines()

for data in range(len(lines_data)):
    lines_split_data = lines_data[data].split('\t')
    phi_data.append(float(lines_split_data[0]))
    U_FB_bar_data.append(float(lines_split_data[1]))

### Plotting -----
plt.figure()

C1 = 'k'

plt.subplot(1,2,1)
plt.plot(phi_list[0:12],U_FB_bar_list[0:12],label='Modified results',c=C1,marker='o',linestyle='none',fillstyle='none')
plt.plot(phi_data[67:67+39],U_FB_bar_data[67:67+39],marker='+',c='k',linestyle='none',label='Experiments')
plt.plot(Default_Model_phi,Default_Model_UFB[0:12],label='Default results',c=C1,marker='o',linestyle='none')
plt.xlabel('$\phi$ (-)', fontsize=14)
plt.ylabel('$\overline{U}_{FB}$ (m/s)', fontsize=14)
plt.title('Channel, T=293 K',fontsize=14)
XLIM = [0.2,1]
YLIM = [0,120]
NN = 4
plt.xlim(XLIM[0],XLIM[1])
plt.ylim(YLIM[0],YLIM[1])
plt.xticks=(np.arange(XLIM[0],XLIM[1]+(XLIM[1]-XLIM[0])/NN,step=(XLIM[1]-XLIM[0])/NN))
plt.yticks=(np.arange(YLIM[0],YLIM[1]+(YLIM[1]-YLIM[0])/NN/2,step=(YLIM[1]-YLIM[0])/NN/2))
plt.grid(True)
plt.legend(loc=2,fontsize=12)
plt.show()

plt.subplot(1,2,2)
plt.plot(phi_list[0:12],U_FB_bar_list[12:24],label='Modified results',c=C1,marker='o',linestyle='none',fillstyle='none')
plt.plot(phi_data[67+39:75+39],U_FB_bar_data[67+39:75+39],marker='+',c='k',linestyle='none',label='Eichler(2012) confined tube, T=473 K')
plt.plot(Default_Model_phi,Default_Model_UFB[12:24],label='Default results',c=C1,marker='o',linestyle='none')
plt.xlabel('$\phi$ (-)', fontsize=14)
plt.title('Channel, T=473 K',fontsize=14)
XLIM = [0.2,1]
YLIM = [0,120]
NN = 4
plt.xlim(XLIM[0],XLIM[1])
plt.ylim(YLIM[0],YLIM[1])

```

```

plt.xticks=(np.arange(XLIM[0],XLIM[1]+(XLIM[1]-XLIM[0])/NN,step=(XLIM[1]-XLIM[0])/NN))
plt.yticks=[]
plt.grid(True)
plt.show()

plt.figure()

plt.subplot(1,2,1)
plt.plot(phi_list[0:12],U_FB_bar_list[24:36],label='Modified results',c=C1,marker='o',linestyle='none',fillstyle='none')
plt.plot(phi_data[75+39:86+39],U_FB_bar_data[75+39:86+39],marker='+',c='k',linestyle='none',label='Eichler(2012) confined tube, T=673 K')
plt.plot(Default_Model_phi,Default_Model_UFB[24:36],label='Default results',c=C1,marker='o',linestyle='none')
plt.xlabel('$\phi$ (-)', fontsize=14)
plt.ylabel('$\overline{U}_{FB}$ (m/s)', fontsize=14)
plt.title('Channel, T=673 K',fontsize=14)
XLIM = [0.2,1]
YLIM = [0,120]
NN = 4
plt.xlim(XLIM[0],XLIM[1])
plt.ylim(YLIM[0],YLIM[1])
plt.xticks=(np.arange(XLIM[0],XLIM[1]+(XLIM[1]-XLIM[0])/NN,step=(XLIM[1]-XLIM[0])/NN))
plt.yticks=[]
plt.grid(True)

plt.subplot(1,2,2)
plt.plot(phi_list[36:48],U_FB_bar_list[36:48],label='Modified results',c=C1,marker='o',linestyle='none',fillstyle='none')
plt.plot(phi_data[0:67],U_FB_bar_data[0:67],marker='+',c='k',linestyle='none',label='Experiments by Eichler')
plt.plot(Default_Model_phi,Default_Model_UFB[36:48],label='Default results',c=C1,marker='o',linestyle='none')
plt.xlabel('$\phi$ (-)', fontsize=14)
plt.title('Tube, T=293 K',fontsize=14)
XLIM = [0.2,1]
YLIM = [0,120]
NN = 4
plt.xlim(XLIM[0],XLIM[1])
plt.ylim(YLIM[0],YLIM[1])
plt.xticks=(np.arange(XLIM[0],XLIM[1]+(XLIM[1]-XLIM[0])/NN,step=(XLIM[1]-XLIM[0])/NN))
plt.yticks=[]
plt.grid(True)

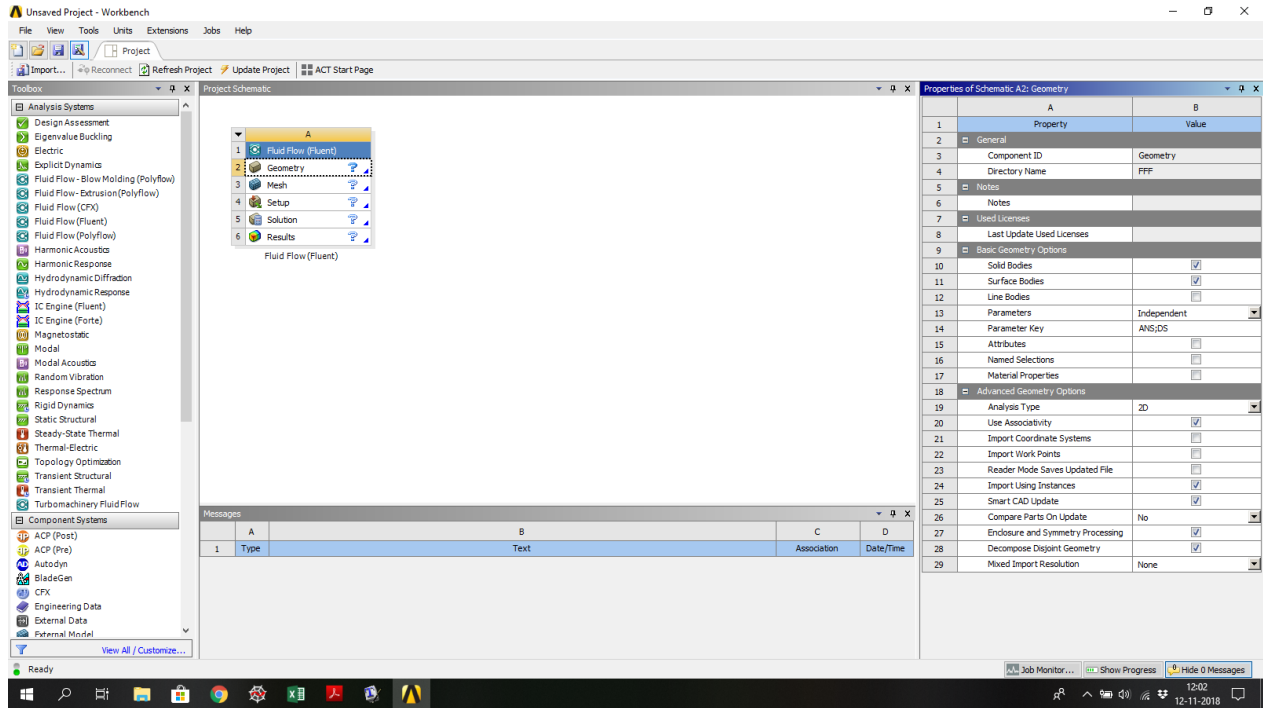
plt.show()

```

## 6.2 Fluent Example: Basics

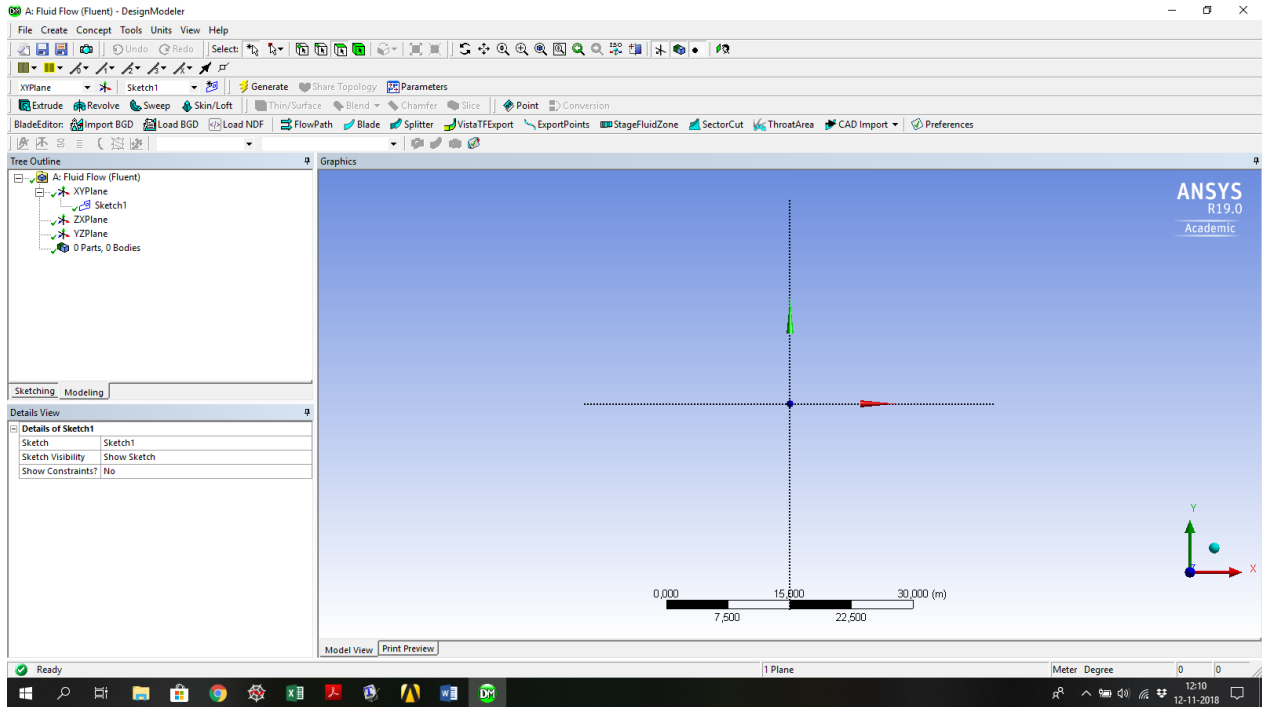
Step 1:

- Launch *Workbench*.
- Drag the *Fluid Flow (Fluent)* icon into the empty field (*Project Schematic*).
- Click once on *Geometry* and make sure to check the 2D option of *Analysis Type*.
- Then right-click on *Geometry* and choose *New DesignModeler Geometry*.



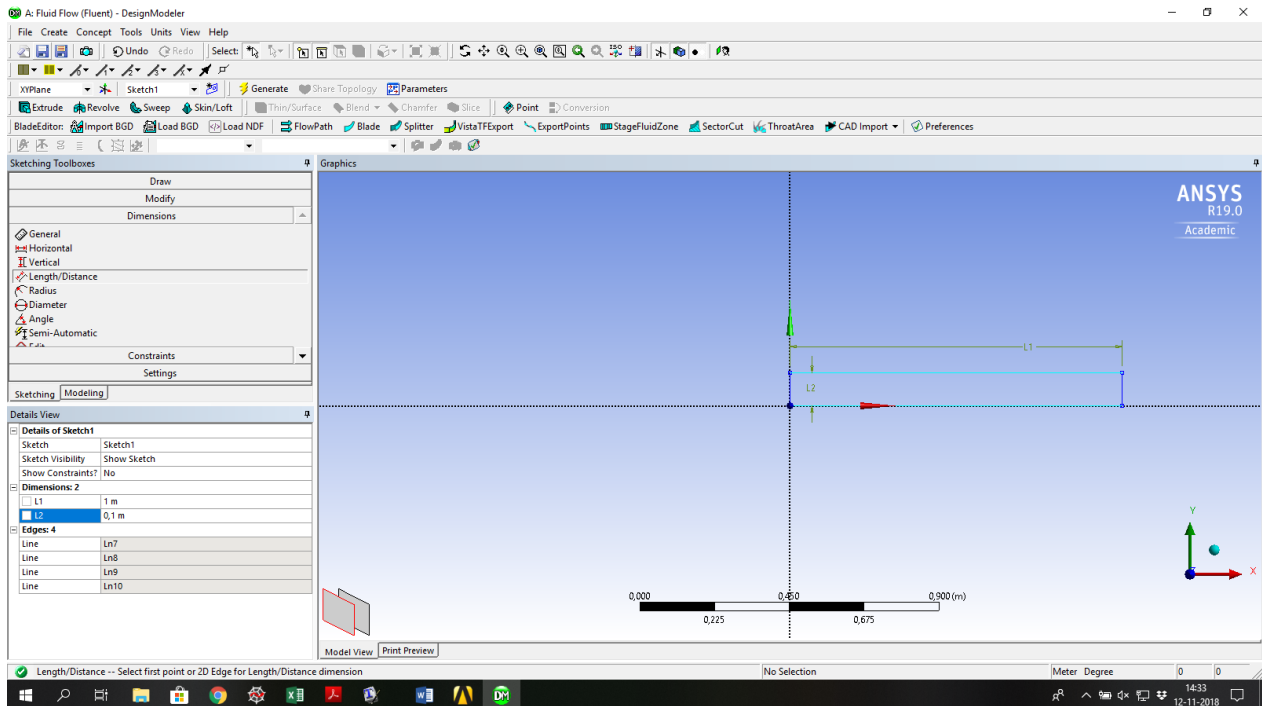
Step 2:

- Click on the blue z axis in the bottom right to work in the xy -plane (since 2D is required).
- In the *Tree Outline* select the *XYPlane* and click on *New Sketch*.
- Then right-click on *Geometry* and choose *New DesignModeler Geometry*.



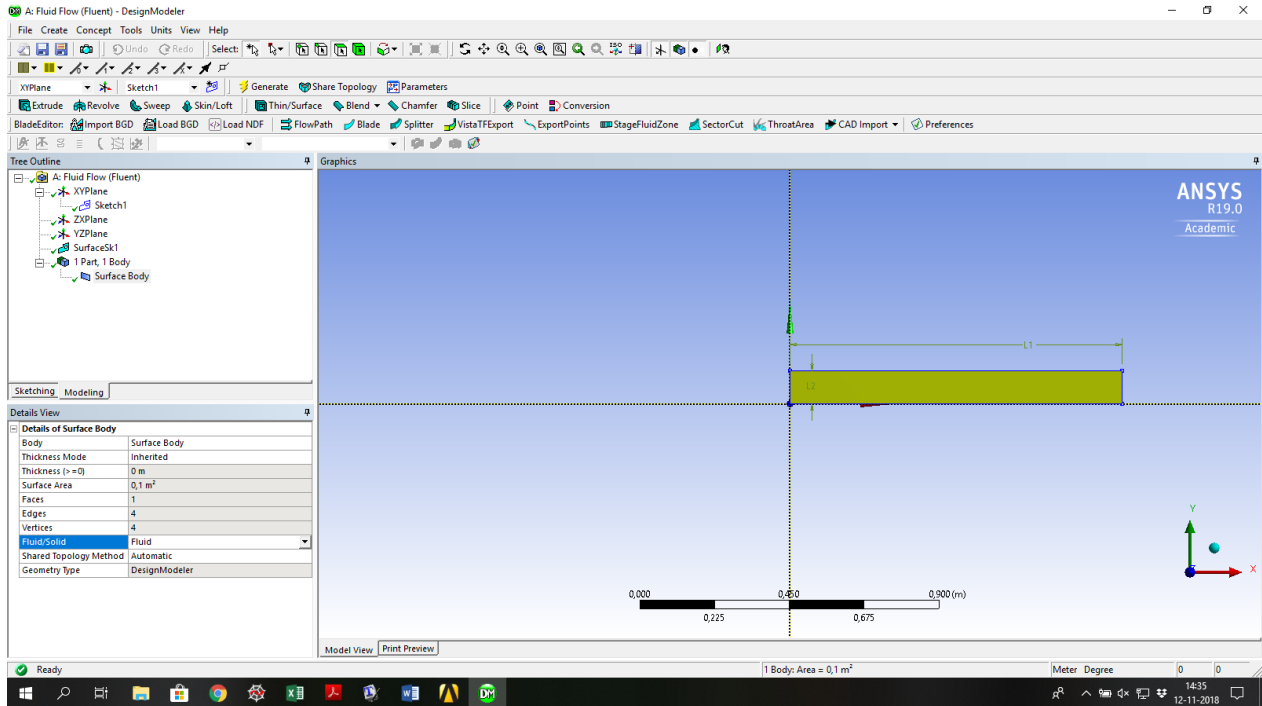
### Step 3:

- Under *Draw* select *Rectangle* and click twice in the model to define the rectangle. In my case the first point is at the origin and the second to the upright. My coordinates are then always positive and start at zero, which is useful for reading data.
- Under *Dimensions* and *Constraints* some tools can be used to constraint your geometry. I only use the *Length/Distance* tool under *Dimensions* to set the height and length of my rectangle. First select the *Length/Distance* tool and then click on two lines. Set the length to 1 m and the height to 0.1 m.



#### Step 4:

- Then go to *Concept* on the top left and choose *Surface From Sketches*. Select *Sketch1* and press *Apply* in the *Details View* option: *Base Objects*. Evaluate by clicking on *Generate*.
- Finally, in the *Tree Outline* unfold *1 Part, 1 Body* and select *Surface Body*. Make sure to check *Fluid* in the *Fluid/Solid* option.
- Close *DesignModeler*.



## Step 5:

- In *Workbench* now double-click on *Mesh*. Check if there is a green 'V' behind *Geometry*.

The screenshot displays the ANSYS Workbench interface. The central 'Project Schematic' shows a sequence of components: Fluid Flow (Fluent), Geometry, Mesh, Setup, Solution, and Results. The 'Mesh' component is selected, and a green checkmark is visible next to it. The 'Properties of Schematic A3: Mesh' panel on the right shows the following table:

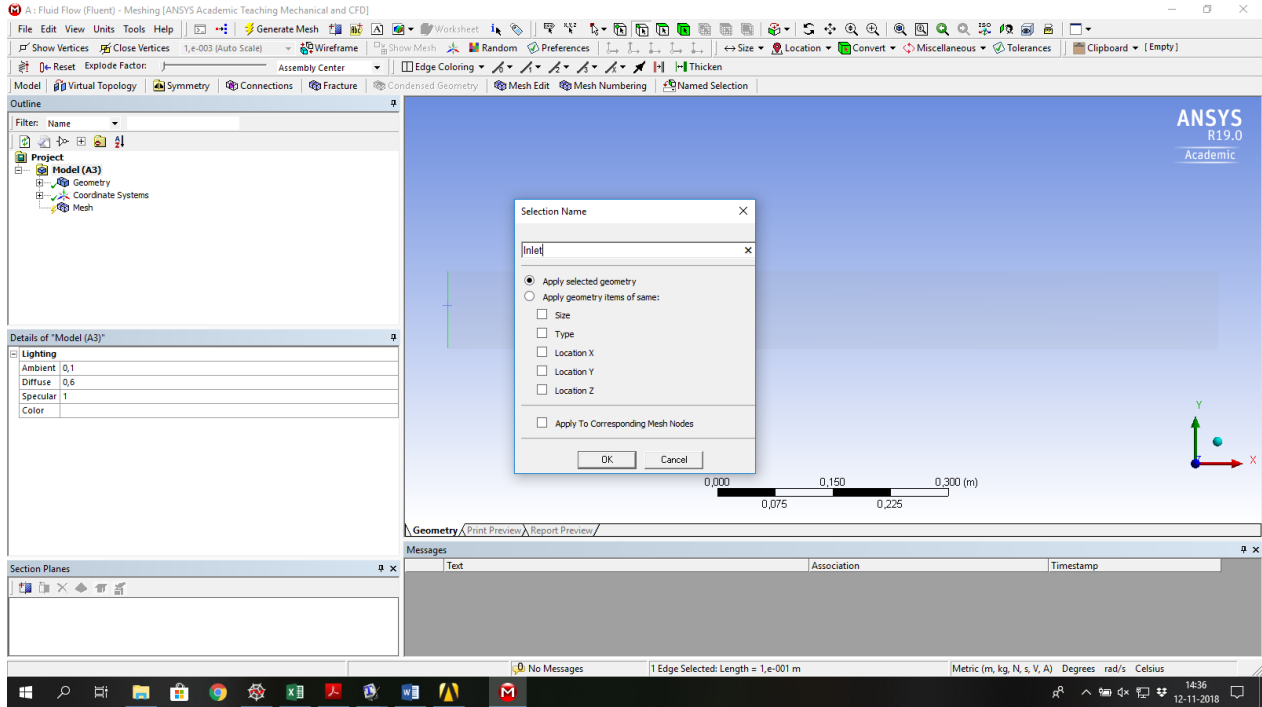
	A	B
1	Property	Value
2		
3	General	
4	Component ID	Mesh
5	Directory Name	FFF
6		
7	Notes	
8	Notes	
9	Used Licenses	
10	Last Update Used Licenses	
11	System Information	
12	Physics	CFD
13	Analysis	Any
14	Solver	FLUENT
15	Mesh	
16	Save Mesh Data In Separate File	<input type="checkbox"/>

The 'Messages' panel at the bottom shows a table with columns A, B, C, and D:

	A	B	C	D
1	Type	Text	Association	Date/Time

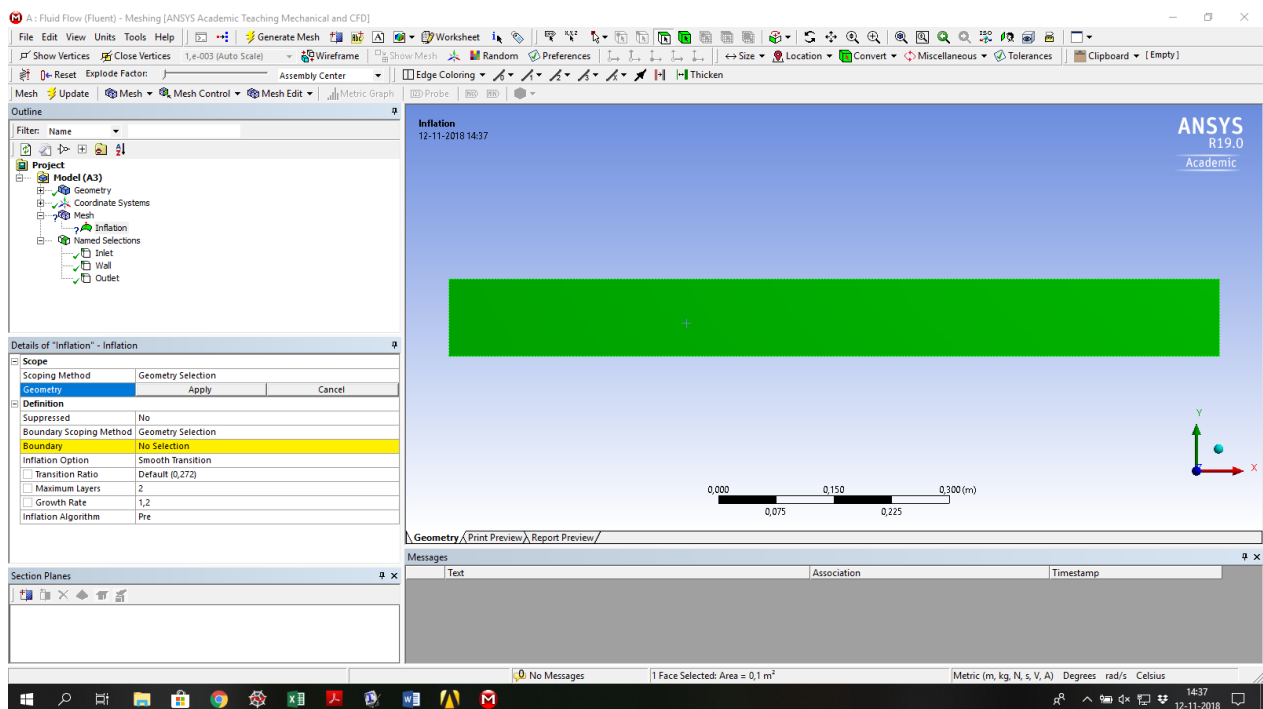
## Step 6:

- Choose *Single Select* and *Edge* in the top bar to enable selecting lines. Select the inlet boundary and right-click and then select *Create Named Selection*. Enter a name such as 'Inlet' and press ok. Repeat this step for the outlet and for the (in this case) two wall boundaries. Selecting more than one item can be done by holding the *Ctrl* key.



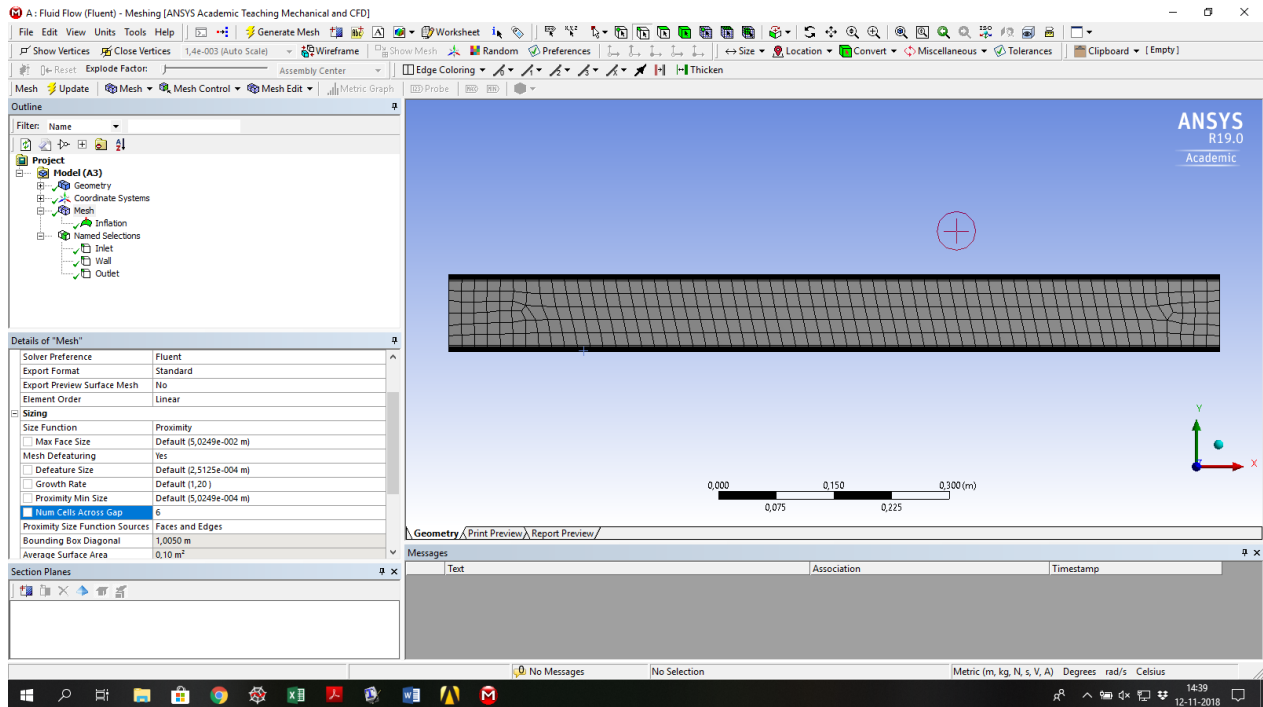
## Step 7:

- In the *Outline* click on *Mesh* to view the *Details of “Mesh”* appearing below. Normally here you specify your mesh. For the simple geometry I use, only an inflation is used, which basically specifies the mesh close to the wall.
- Right click on *Mesh* in the *Outline* and click on *Insert, Inflation*. For *Geometry* select the plane (first enable *Face* selection in the top bar) and press *Apply*. For *Boundary* select the two walls boundaries and press *Apply*.
- For the *Inflation Option* I used *First Layer Thickness*, with a *First Layer Height* of  $6.67e-6$  m, *Maximum Layers*: 30 and a *Growth Rate* of 1.2. The growth rate allows a cell to be 1.2 times higher than the previous cell, counting from the wall. If your inflation layer doesn't fit into the geometry, it might be that Fluent automatically decreases the *First Layer Height* (without telling you). So always zoom into the inflation layer to check if it's correct.
- Press on *Generate Mesh* at the top bar.



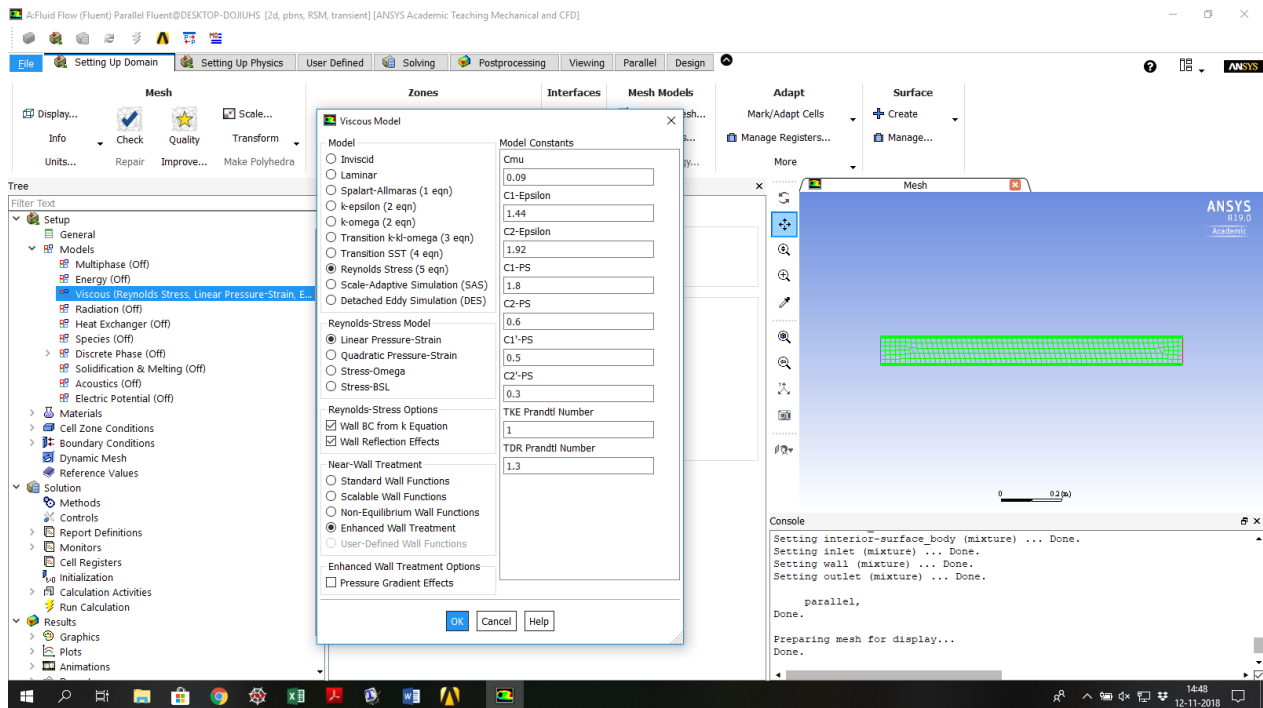
## Step 8:

- In the *Outline* select *Mesh* and your mesh becomes visible in your geometry. The inflation layers will be visible (but thin) and there are two rows of cells in the core region. I think this is too coarse so I will redefine this.
- In *Details of "Mesh"*, *Sizing* choose *Proximity* for *Size Function* and for *Num Cells Across Gap* choose the amount desired. I took 6. Click on *Generate Mesh* again.
- In *Details of "Mesh"*, *Quality* choose *Skewness* for *Mesh Metric*. The *Max* value should never be higher than 1 and preferably below 0.9. The lower the better. Close the meshing software.



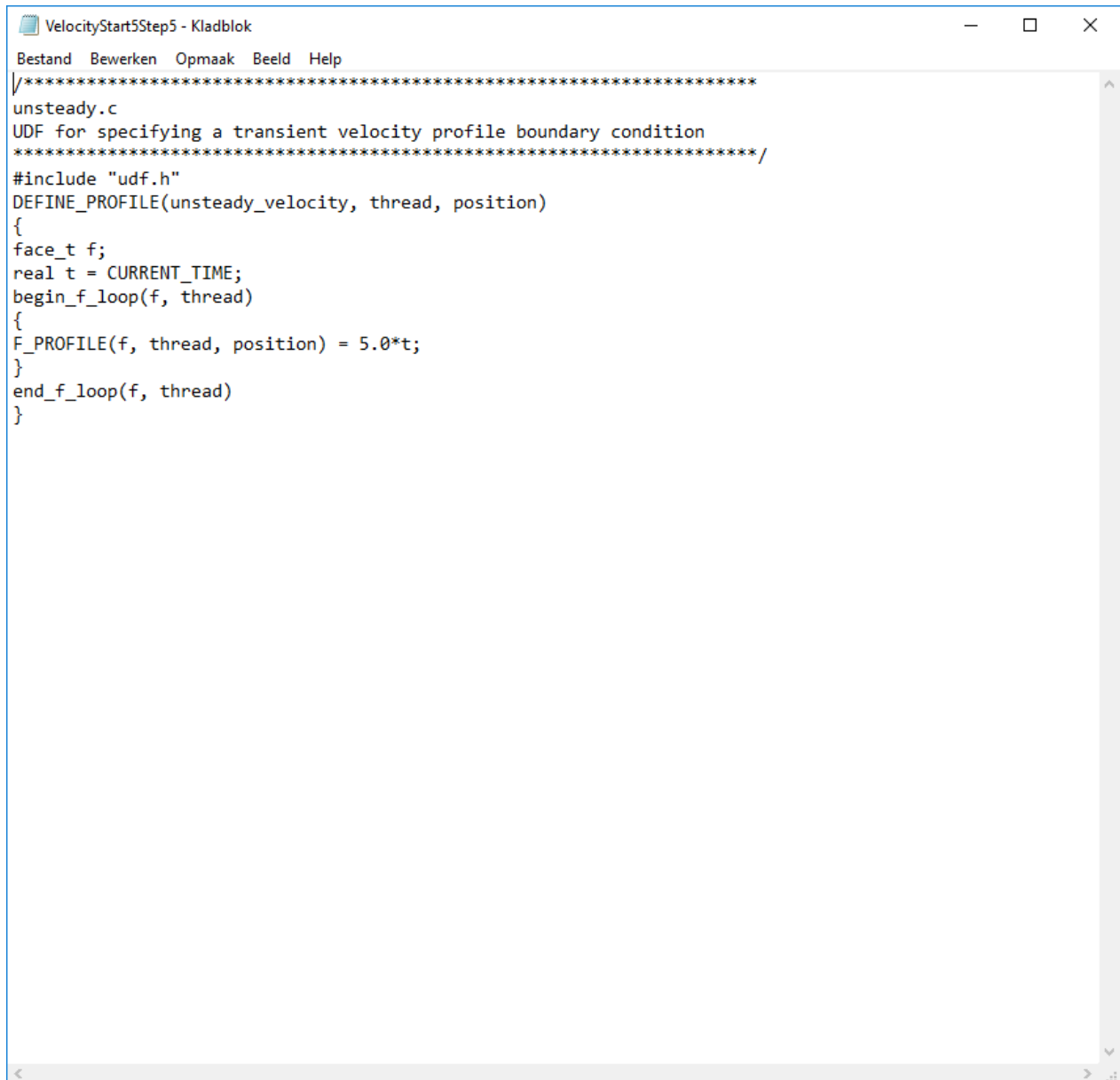
## Step 9:

- In *Workbench* now double-click on *Setup*. It is best to work top to bottom in the Tree, to not forget anything. In the Tree start by double-clicking on *Setup*, *General* and check the *Transient* box under *Time*.
- In the *Tree* now double-click on *Setup*, *Models*, *Viscous* and select *Reynolds Stress* and under *Near-Wall Treatment* select *Enhanced Wall Treatment*. This means that Fluent will solve the set of equations in the boundary layer as well, which will only work because we added a very thin inflation layer close the wall (such that the first cell is as thick as  $y^+ = 1$ ). Press ok and close the tab.
- In the *Tree* double-click on *Setup*, *Materials*, *Fluid*, *Air* and change the name, density and viscosity (to anything you prefer).



Step 10:

- Since the goal of my simulations is to get data for different inlet velocities, I use a transient analysis with a time dependent velocity inlet. This can be done by using a small C code (which I copied somewhere from the internet). The only modification I made was the function itself. If you don't use C, just write the file in notepad or any other simple text editor and save the file as *VelocityStrat5Step5.c* in a folder of preference. (Any name is good)

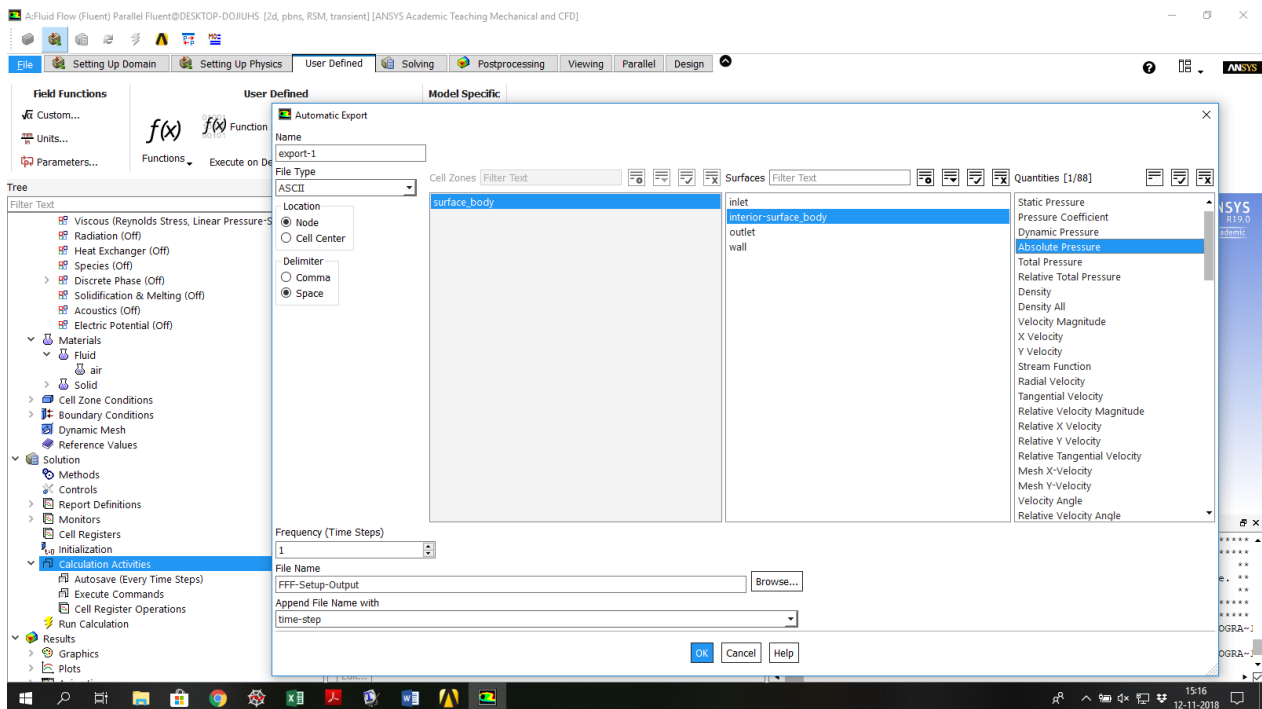


```
VelocityStart5Step5 - Kladblok
Bestand Bewerken Opmaak Beeld Help
/*****
unsteady.c
UDF for specifying a transient velocity profile boundary condition
*****/
#include "udf.h"
DEFINE_PROFILE(unsteady_velocity, thread, position)
{
    face_t f;
    real t = CURRENT_TIME;
    begin_f_loop(f, thread)
    {
        F_PROFILE(f, thread, position) = 5.0*t;
    }
    end_f_loop(f, thread)
}
```



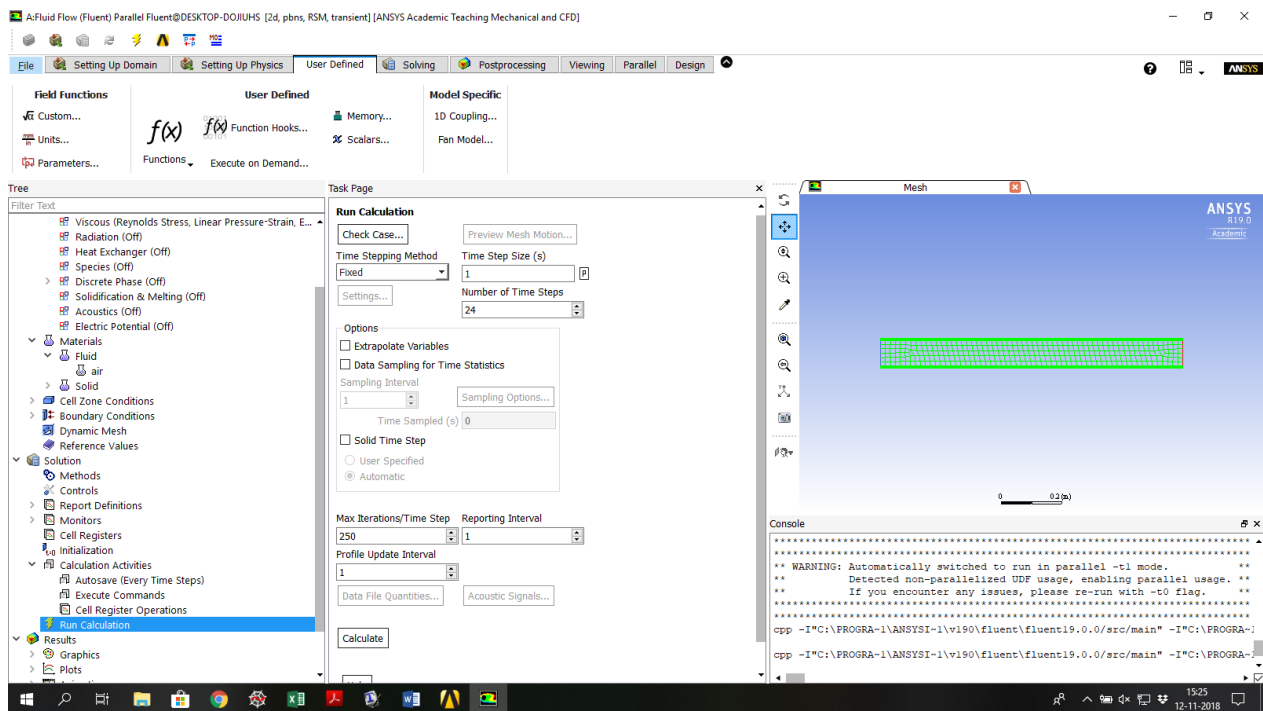
## Step 12:

- In the *Tree* double-click on *Solution, Calculation Activities* and set the *Autosave Every (Time Steps)* to 1, be able to analyse the transient results in CFD post (*Results in Workbench*).
- In the same tab, under *Automatic Export* click on *Create, Solution Data Export*. A new tab opens and for *File Type* choose *ASCII*. This is, I think, the simplest data structure possible and very easy to read with Python (or Matlab). Select *surface\_body* and from *Surfaces* select *interior-surface\_body*. Under *Quantities* select all the required parameters. If the viscous model is changed, these selections might change as well. For example, the k-epsilon model will never produce Reynolds' stress components *uu vv* and so on.
- Define a *File Name* and use browse to select the folder of preference. For 1 simulation with 24 time steps Fluent numbered automatically by ending the files with 0001 to 0024. But a new simulation overwrote these files. Therefore for every new simulation I changed the name of the output file. Also important: once the files are there, copy them into another folder. I had the idea that those files are temporary and I once lost them all, not knowing they are temporary.
- Press ok and close the tab.



### Step 13:

- In the *Tree* double-click on *Solution, Run Calculation*. Verify that the *Time Step Size* is 1 s (default). Set the *Number of Time Steps* to 24 and change the *Max Iterations/Time Step* from 20 to 250.
- Finally, on the top bar click on *Solving* and then click once on *t = 0 Initialize* and then press on *Calculate*. Fluent will now run the simulation and you will get noticed once it has completed.
- In *Workbench* double-click on *Results* to open CFD post. I did not find it easy to export data on custom specified locations (in a fast way) by using CFD post. Therefore I used the *Automatic Export*.



### 6.3 CFD Results

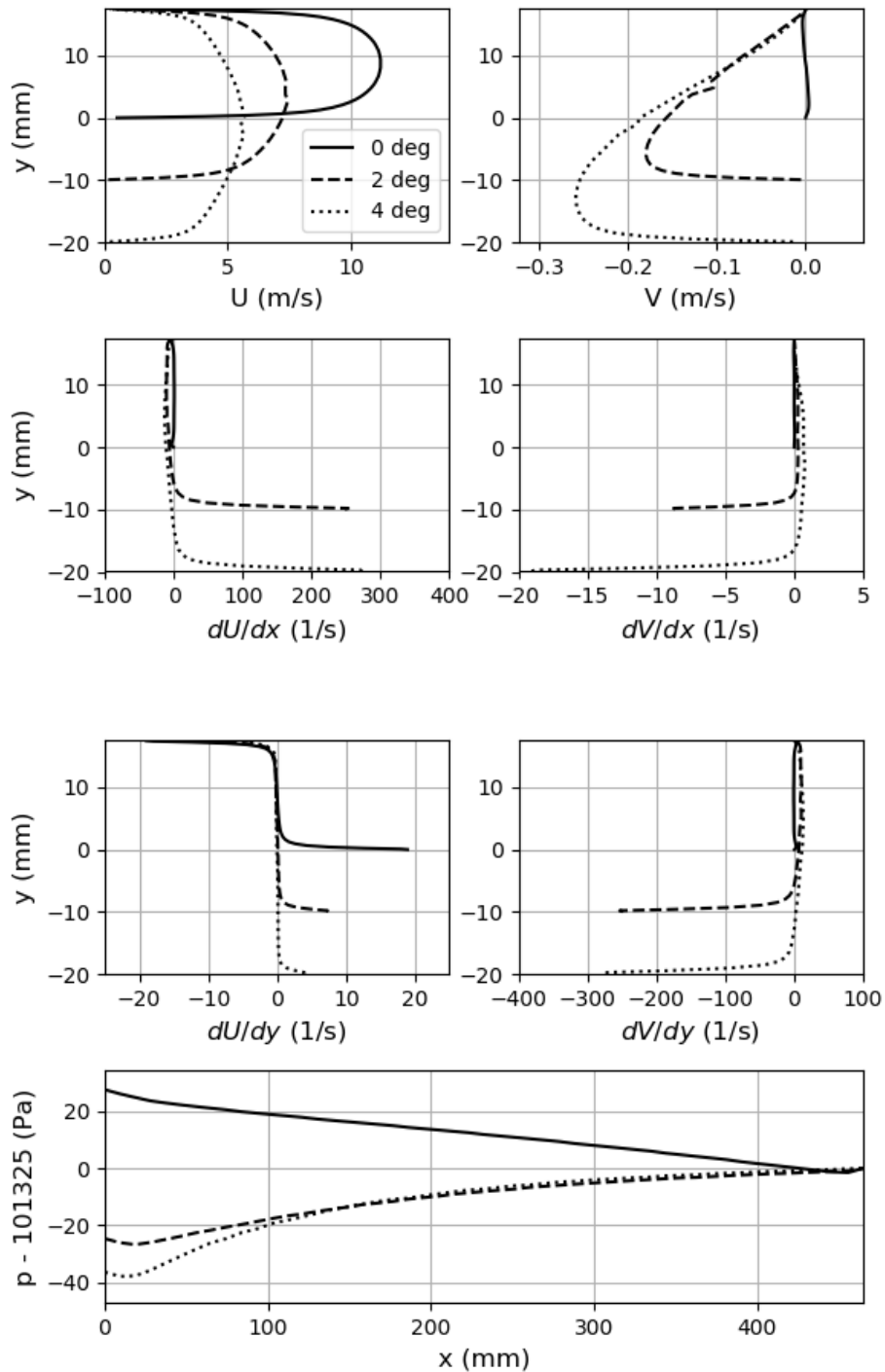


Figure 60: Non-scaled CFD results: velocity profiles over the full channel height at  $x = 300$  mm and the pressure over the full length at half the inlet height.

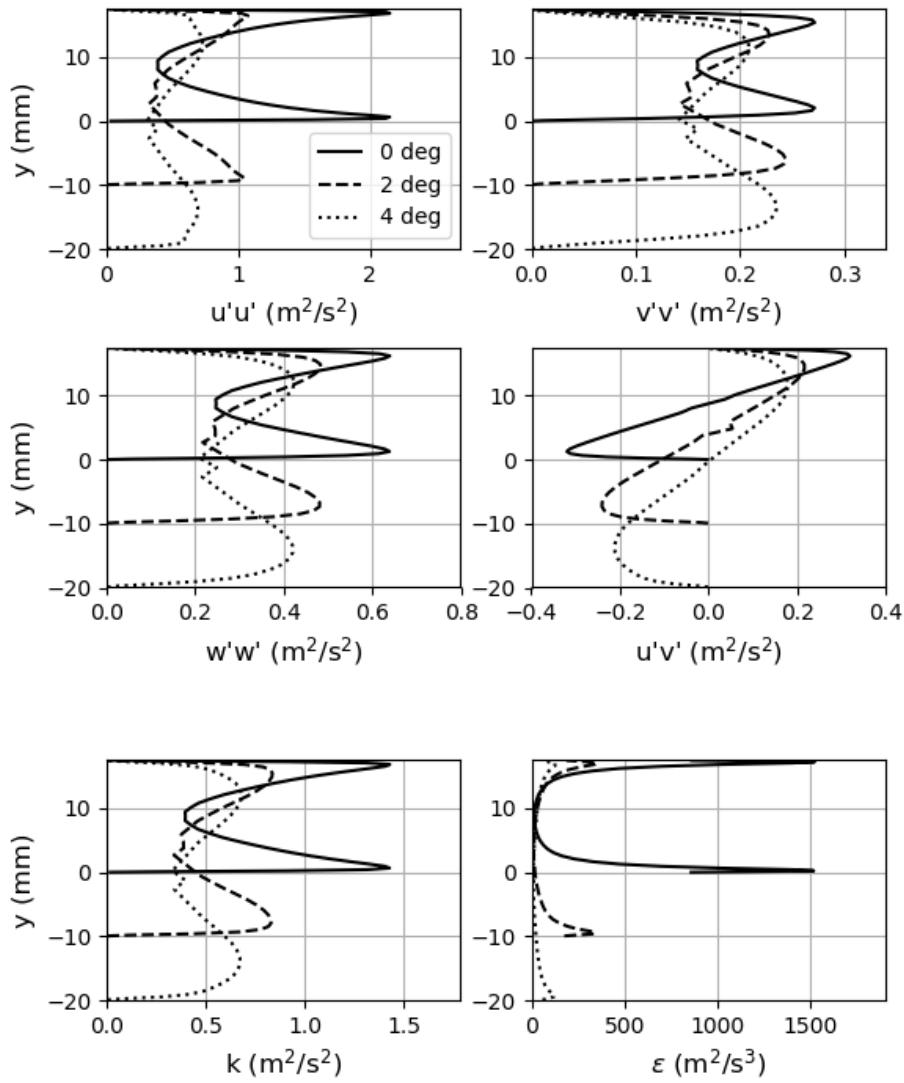


Figure 61: Non-scaled CFD results: turbulence profiles over the full channel height at  $x = 300$  mm.

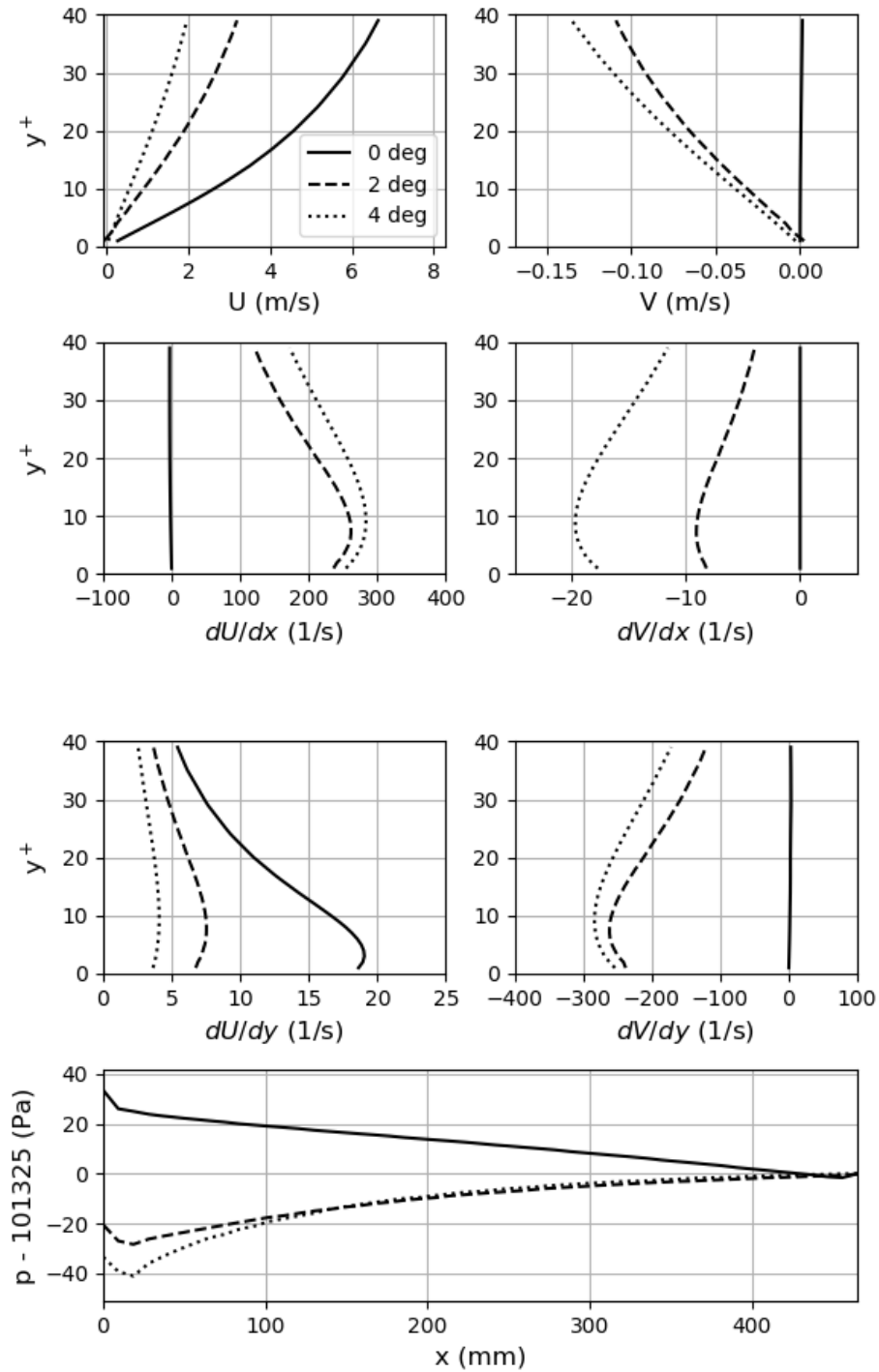


Figure 62: Non-scaled CFD results: velocity profiles in the lower wall region at  $x = 300$  mm and the pressure over the full length at  $y^+ = 15$ .

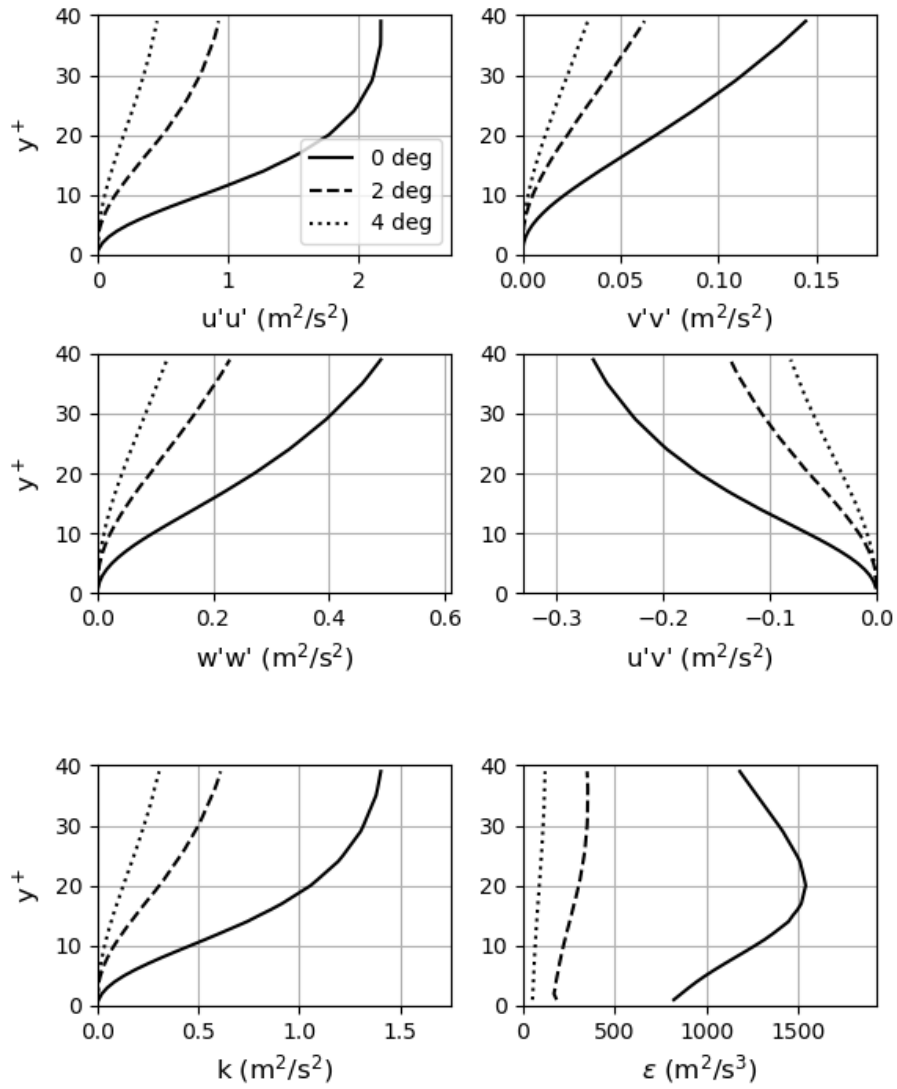


Figure 63: Non-scaled CFD results: turbulence profiles in the lower wall region at  $x = 300$ .